Characterization and Optimization of a Time-of-Flight Detector for Isochronous Mass Measurement at the ESR

Inauguraldissertation
zur
Erlangung des Doktorgrades
der Naturwissenschaftlichen Fakultät
der Justus-Liebig-Universität Gießen

vorgelegt von

Benjamin Fabian

aus Münzenberg/Hessen

Gießen 2008

Zusammenfassung

Die isochrone Massenmessung, die am Fragmentseparator (FRS) und Experiment-Speicherring (ESR) der GSI in Pionierexperimenten durchgeführt wird, erlaubt es Massen exotischer Kerne mit Lebensdauern von einigen 10 μs mit einer Genauigkeit von 10^{-6} zu messen. Die exotischen Kerne werden durch Projektilfragmentation und Uranspaltung am Eingang des FRS bei relativistischen Energien erzeugt, im Fluge räumlich getrennt und danach in den Speicherring eingeschossen. Die Impulsverteilung der erzeugten Fragmente ist bis zu einigen Prozenten breit, so dass die isochrone Einstellung des ESR für präzise Massenmessungen erforderlich ist. Dieser spezielle Modus des ESRs ermöglicht es, dass Ionen mit identischen Masse-zu-Ladungsverhältnisses aber verschiedenen Geschwindigkeiten mit derselben Umlauffrequenz im ESR zirkulieren.

Um nun die Masse der Kerne zu bestimmen, wird die Umlauffrequenz der gespeicherten Ionen gemessen, die ein direktes Maß für das Masse-zu-Ladungsverhältnis ist. Die Bestimmung der Umlauffrequenz erfolgt mit einem Flugzeitdetektor, der auf einer der langen geraden Strecken des ESRs eingebaut ist. Im Detektor durchqueren die zu messenden Teilchen eine dünne Folie und setzen dabei Sekundärelektronen durch atomare Wechselwirkungen frei. Bei jedem Durchgang der Ionen durch die Folie, werden Sekundärelektronen erzeugt, die über eine Kombination von elektrischen und magnetischen Feldern auf einen Mikrokanalplatten-Detektor (MCP-Detektor) isochron transportiert werden. Der Detektor erlaubt es unter anderem auch, dass die Elektronen auf der Eintritts- und Austrittsseite zur zusätzlichen Identifikation eines Ions genutzt werden können.

In dieser Arbeit wurde dieser Flugzeitdetektor mittels komplexen Simulationen, Offline-Messungen mit α-Teilchen und Elektronen und Online-Messungen mit einem stabilen $^{64}Ni^{28+}$-Strahl charakterisiert und optimiert. Alle Phasen von der Bewegung der Ionen im Ring, der Erzeugung von Sekundärelektronen, deren Transport zu dem MCP, sowie die Detektion werden untersucht und mit theoretischen Vorhersagen und Simulationen verglichen.

Die Simulation der Verlustraten der Ionen im Speicherring zeigt auf, dass die reinen ionenoptischen Verlustraten hauptsächlich durch den endlichen Radius der Detektorfolie, sowie den mittleren Energieverlust in der Folie bestimmt ist. Eine Reduzierung der Foliendicke führt, wie erwartet, zu einer Zunahme der mittleren Anzahl der möglichen Umläufe im Ring.

Die mittlere Anzahl von Sekundärelektronen, die pro einfallendes Ionen erzeugt werden, sind über ein einfaches Skalierungsgesetz abgeschätzt worden und sind in guter Übereinstimmung mit Offline- und Online-Messungen.

Simulationen des Transports der erzeugten Sekundärelektronen zum Mikrokanalplatten-Detektor haben gute Übereinstimmungen mit Offline-Messungen und zufriedenstellende Übereinstimmung mit Online-Messungen gezeigt. Mit den Resultaten der Simulation war es möglich, die Transmission der Elektronen von der Folie um einen Faktor 2 und damit die Nachweiswahrscheinlichkeit zu steigern. Der Detektor erlaubt in diesen neuen Feldeinstellungen, aus der Simulation, eine effizientere und gleichmäßigere Ausnutzung der Folie bei nur vernachlässigbarer Erhöhung der Flugzeitverschmierung (21 ps).

Die Anzahl der auf das MCP treffenden Sekundärelektronen ist ein direktes Maß für die Detektoreffizienz, was durch theoretische Betrachtungen und Messungen gezeigt werde konnte.

Es ist ebenso noch gezeigt worden, dass Aufladeeffekte des Mikrokanalplattendetektors für Messungen am Speicherring zu berücksichtigen sind, da dort die Umlauffrequenz von ca. 2 MHz relativ hoch ist. Diese Annahme ist durch systematische Untersuchungen des MCPs-Detektors, theoretische Betrachtungen, sowie Online-Messungen, verifiziert worden.

Eine Erhöhung der Umlaufdauer der Ionen im Ring kann durch Benutzung dünnerer Kohlenstofffolien erzielt werden. In Offline-Messungen ist die Detektionseffizienz verschieden dicker Kohlenstofffolien untersucht worden, sowie deren Vergleich zur derzeit benutzten CsI beschichteten Folie. Untersuchungen haben ergeben, dass die Detektionseffizienz der Kohlenstofffolien ab einer Dicke von 10 $\mu g/cm^2$ konstant bei etwa 80% für α-Teilchen liegt und nur für geringere Foliendicke abnimmt. Des Weiteren kann gezeigt werden, dass die Detektionseffizienz mit der CsI beschichteten Folie nur leicht erhöht ist, verglichen zu den reinen Kohlenstofffolien. Die Abnahme der Detektionseffizienz, sowie die nur leicht erhöhte Effizienz der CsI Bedampfung kann über theoretische Modelle der Sekundärelektronenerzeugung befriedigend erklärt werden.

Diese Arbeit dient dem Erlangen eines detaillierten Verständnisses aller physikalischen und technischen Prozesse, die für die Weiterentwicklung eines Flugzeit-Detektorsystems für die isochrone Massenmessung am Collector Ring, bei der neuen "Facility for Antiproton and Ion Reseach (FAIR), wichtig sind.

Contents

1 Summary

Isochronous Mass Spectrometry has been developed to measure masses of exotic nuclei with lifetimes as short as a few tens of microseconds at the FRS-ESR facility at GSI. For measurement of the ions revolution frequencies, a time-of-flight detector is used. Secondary electrons released from a thin carbon foil at each passage of the stored ion through the detector are transported to micro-channel-plates (MCP) by electric and magnetic fields.

This time-of-flight detector, currently installed in the ESR to measure the masses of ions in the isochronous mode, was investigated in this work by experiments and realistic simulations. The detector efficiency was optimized off line with α-particles and electrons and tested on line with a stable Nickel beam. All stages of the detector from the creation of secondary electrons to the final timing signals were examined. The typical number of secondary electrons released per ion can be estimated within a factor of two using an empirical formula. The formula incorporates the target properties and the electronic stopping power of the ion. Typical average electron numbers for mass measurements in the isochronous mode range from 1 to 10 electrons. The transport of the electrons from the foil to the MCP was calculated for the first time using the 3-dimensional geometry of the detector. The simulation helped to understand the transport of the electrons in the detector and thus optimize the detection efficiency while preserving the timing performance. With the calculate settings the detection efficiency and also the detection duration on one MCP detector side were significantly improved (factor of 2).

The detection efficiency of the MCP in dependence of the average number of secondary electrons was also examined in the experiment. The detection efficiency of the MCP detector for a Ni-projectile at 372 MeV/u was estimated to be about 88%. In addition saturation effects of the MCPs were examined . The saturation effect is a dead time effect, which happens because of the large recharge time of the micro channels (1-10 ms) compared to the measurement time (400 μs). This effects causes the decrease of the gain and so the amplitude of the signals. This also will have the effect of decrease of the detection efficiency. The dependence of the detection efficiency of the thickness of carbon foils was measured and yields an excellent detection efficiency for foil thickness down to 10 $\mu g/cm^2$. Using thinner foils will allow longer observation times in the ring due to less energy loss and straggling. By taking all these effect into account it is possible to describe the behaviour of the detection efficiency and the amplitude

in dependence of the turn number. This new knowledge makes it possible to further improve the detector in the ESR and within the ILIMA project to develop a new dual detector system for the CR at FAIR.

2 Motivation of Mass Measurement of Exotic Nuclides

The mass of a particle is one of the most fundamental properties that can be measured in physics. In nuclear and high energy physics the mass is a measurable parameter that yields a lot of information about the structure of a particle. This is caused by the fact that the mass of a particle is related to its binding energy. The structure is directly connected to the binding energy of the nucleus and by using sufficient nuclides models it is possible to calculate the local distribution of the neutrons and protons.

An important field in which the masses of exotic nuclides far from the stability need to be known precisely are nuclear reactions in astrophysics. The r-process, which is known to be the main process for the creation of heavy chemical elements proceeds in the unexplored region of neutron-rich nuclides [Bbfh-57]. To calculate the r-process, measuremenst of more precise mass values of exotic nuclides located in the very neutron-rich region are necessary.

A further important field is the nuclear structure research that is also based on the mass properties. Most of the theoretical models are only valid close to the stable region. The further away one goes from the region of stability the worse the accuracy of the models get (fig. [2.2]). So experimentally measured masses can be used to develop better theories of nuclear models that can describe a broader range of nuclides. Another interesting question that can be answered is the location of the proton and neutron drip lines (fig. [2.1]).

With increasing beam intensities at accelerator facilities it is possible to produce more exotic nuclides that are even further away from the region of stability than previously found nuclides. At the moment about 3100 different nuclides and 580 isomers are known [Chart-08] but not all of them have well defined or measured masses. Most of the exotic nuclides have relatively short lifetimes compared to the natural existing stable isotopes. So they have to be produced before they can be measured. The lifetimes vary from minutes to microseconds. Exotic nuclides can be produced by performing nuclear reactions using particle accelerators.

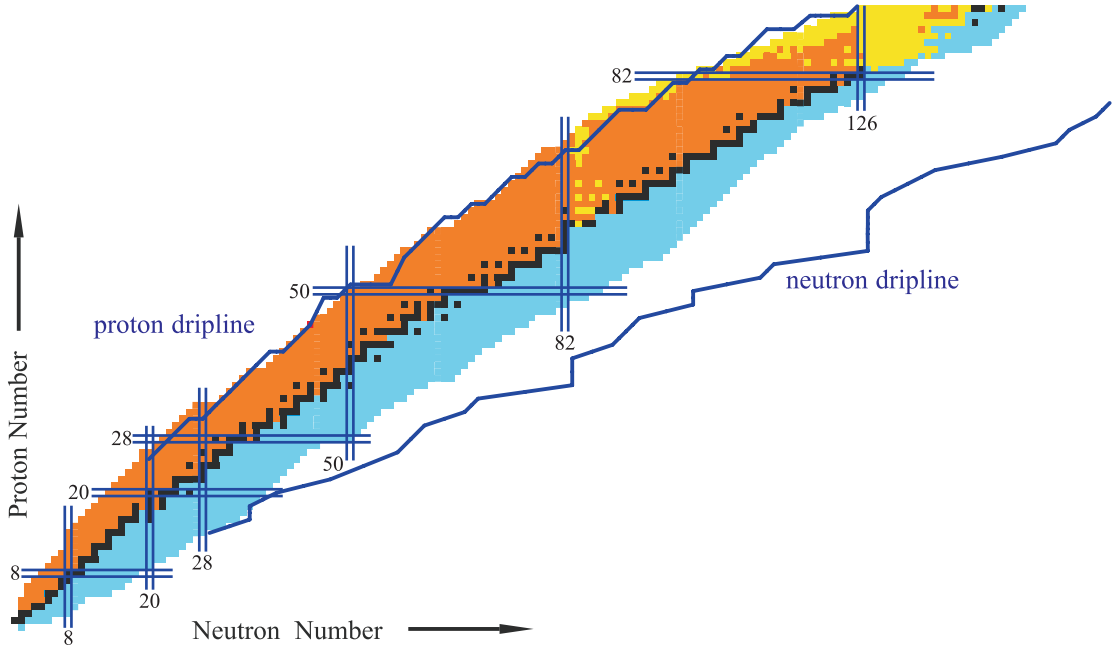

Figure 2.1: Chart of nuclide including the proton and neutron drip lines [LitS-08].

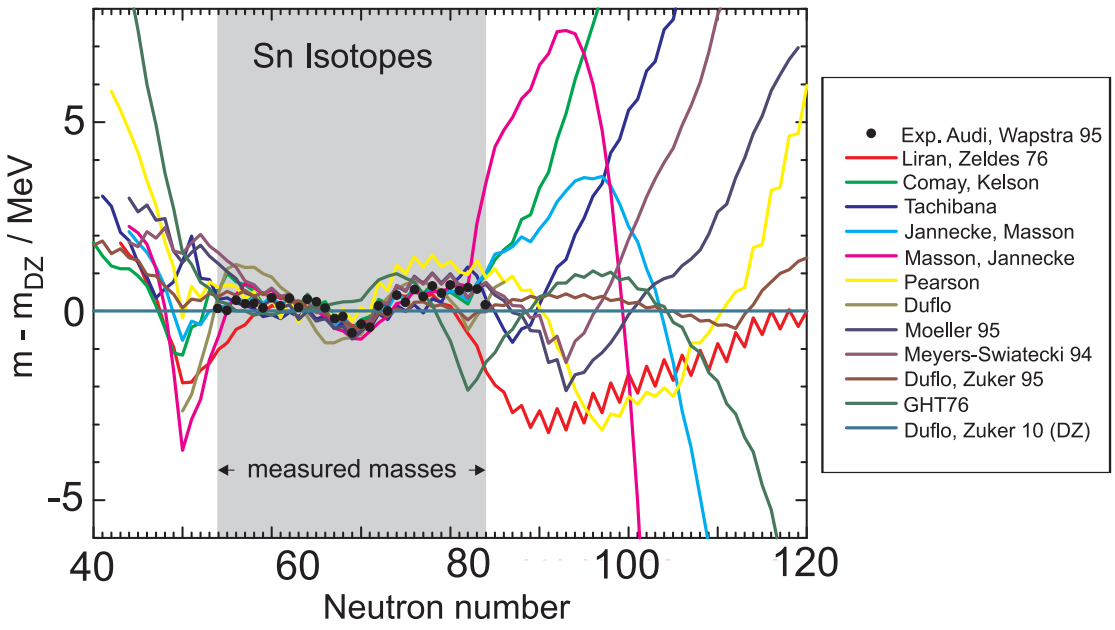

Figure 2.2: Comparison of measured Sn-isotopes with different mass models [Lun-98].

2.1 Creation and Separation of Exotic Nuclear Beams

Before the properties of an exotic nucleus can be measured it must be produced. A way to produce exotic nuclides is done by using a stable ion beam that is shot onto a target where different ion species are created by nuclear reactions. A “cocktail” of exotic particles is created and therefore the nuclides of interest must be seperated from the beam. Ions of stable isotopes are created in ion sources. The stable ions are then extracted into a linear accelerator where they are pre-accelerated. Then the beam is injected into a ring accelerator in which the ions are further accelerated over multiple turns. The ions are turnwise accelerated by HF-resonators. The increase of speed needs to be compensated by a higher magnetic field. At the GSI facility it is possible to accelerate U^{92+} up to a value of about 1 GeV/u [Bbfp-85]. This pre-processing of the stable beam is mostly the same for most of the experiments. To produce exotic beams the stable beam is shot onto a target where nuclear reactions take place and the exotic products are created and can be separated from the stable beam and further transfered to the experimental areas. The process of the creation of exotic nuclides in the target and the further separation can be mainly divided into two different approaches named the in-flight method and the isotope-separation-on-line (ISOL).

2.1.1 ISOL

The ISOl (Isotope-Separation On-Line) technique is a widely used technique to create and separate exotic nuclear beams. This method is successfully used at ISOLDE at CERN [Hhj-92]. Proton or other light ion beams are shot onto a thick target that includes heavy elements. The three main reaction channels in the target are the spallation, fragmentation and fission of the heavy target nuclei. The exotic nuclides created, diffuse through the target. During the diffusion process, the ions are thermalized before they leave the solid. After desorbing from the target’s surface they are ionized in an ion source. The ions are selected accoriding to their charge state and extracted using an electric field and furthermore accelerated by a typical voltage of 50 kV. This technique allows high production rates because of the thick target and the high primary ion beam current that can be achieved with light ions.

The disadvantage is that the efficiency of the production of the exotic nuclides depends strongly on the chemical and solid state properties of the target. For specific combinations of projectiles and targets a higher yield of products can be produced than in the in-flight method. Mostly it is not straight-forward to make predictions about the intensity of a secondary beam because of the complex properties of the target and projectile combination. An other disadvantage is that it is not possible to go to very exotic nuclides with short life times. This is caused by the total time it takes to prepare the

secondary beam for the experiment. Life times that can be still measured are in the range of 10 ms [Bdc-99].

2.1.2 In-Flight Method

In the In-Flight method a primary beam of heavy ions is shot onto a thin target. Typical processes that occur in the target are the fragmentation, electromagnetic dissociation, fusion and fission of the heavy projectiles (fig. [2.3]).

The projectile fragmentation uses a heavy projectile that is shot onto a target consisting of lighter elements like beryllium. This is a process in which a part of the projectile nucleons are sheered off (abrasion) while the rest of the nucleus is left in an excited state that deexcites and leads to a fragment (ablation). The kinetic energy of the fragments is very close to the kinetic energy of the projectiles. So the momentum distribution of the secondary particles is small and given by the Fermi-momentum of the nucleons and the momentum difference caused by the different masses of the projectile and fragment. The momentum distribution can be calculated using a description of Goldhaber [Gol-74]. A detailed description of the reaction kinematics can be found in [Gol-74], [Mor-89].

If the target consists of heavier elements there are two more important processes that can occur. The projectile can also get excited by the coulomb-interaction with the heavy target nuclides. Once excited, the nuclides can deexcite by losing nucleons or even fission. This process is called the electromagnetic dissociation.

The induced fission describes the excitation of the projectile and breaking apart of the projectile. Typically the fission products leave the target with kinetic energies higher than the projectiles energy. Therefore the products of the induced fission have a broader momentum distribution than nuclides created by the projectile fragmentation process.

For lower projectile energies close to the Coulomb barrier it is also possible to fusion nuclides. If the kinetic energy of the projectile is sufficient to overcome the Coulomb-barrier or to tunnel through the barrier of the target nuclides they become a compound-nucleus. Typically the newly formed nucleus is in an excited state. The newly formed nucleus starts to deexcite by γ-radiation and evaporation of nucleons until it gets into a non-excited state. If this process of deexcitation is faster than any breakup process the formed product survives and can be transfered to further experimental areas. Experiments concerning the fusion of elements in-flight are performed using the velocity filter SHIP [Muenz-79] at the GSI.

The advantage of the in-flight-method is that after the creation of the exotic nuclides no acceleration or ionization is necessary. This advantage gives access to exotic nuclear beams with life times in the order of μs down to hundreds of nanoseconds. Sometimes

a disadvantage of the in-flight and ISOL-method is that a broad spectrum of exotic nuclides is created which needs to be separated from the interesting ones.

2.1.3 Separation of Ions using the Fragment Separator at GSI

The separation of ions can be done by using electric and magnetic fields. An important feature to note is that electric fields separate according to kinetic energies of the particles while the magnetic fields separate according to the momentum of the charged particles.

The fragment separator (FRS) [Gab-92] at GSI is an instrument that is successfully used for the efficient separation of ions. The FRS (fig. [2.4]) consists of a three step system for the selection of a specific ion species. First the primary beam is shot onto a production target where exotic nuclides with almost the same velocity as the primary beam are produced. In the first stage the exotic ions are separated by their momentum. This is done by using a magnetic dipole system that also includes quadrupoles to focus the beam. So at the midplane of the seperator (F2) only ions with specific m/q are detectable. In the middle of the FRS a degrader is installed to separate the ions with same m/q now by their nuclear charge Z. The ions pass through the degrader and lose energy by atomic interactions depending on their atimic number. Therefore ions with different Z have different momenta after the passage trough the degrader. The next stage behind the degrader selects ions again according to their momentum while now only ions with a specific mass and charge can be effectively chosen. Using this so called $B\rho - \Delta E - B\rho$ method it is possible to select a specific element at the final focus of the seperator (F4).

The FRS can also be used as a secondary beam source for a broad spectrum of mass-to-charge ratios by not using the degrader. The FRS is typically used in this mode when mass measurements in the storage ring ESR are performed because of the broad range of ions with a specific mass to charge ratio that can be created using this mode of the FRS.

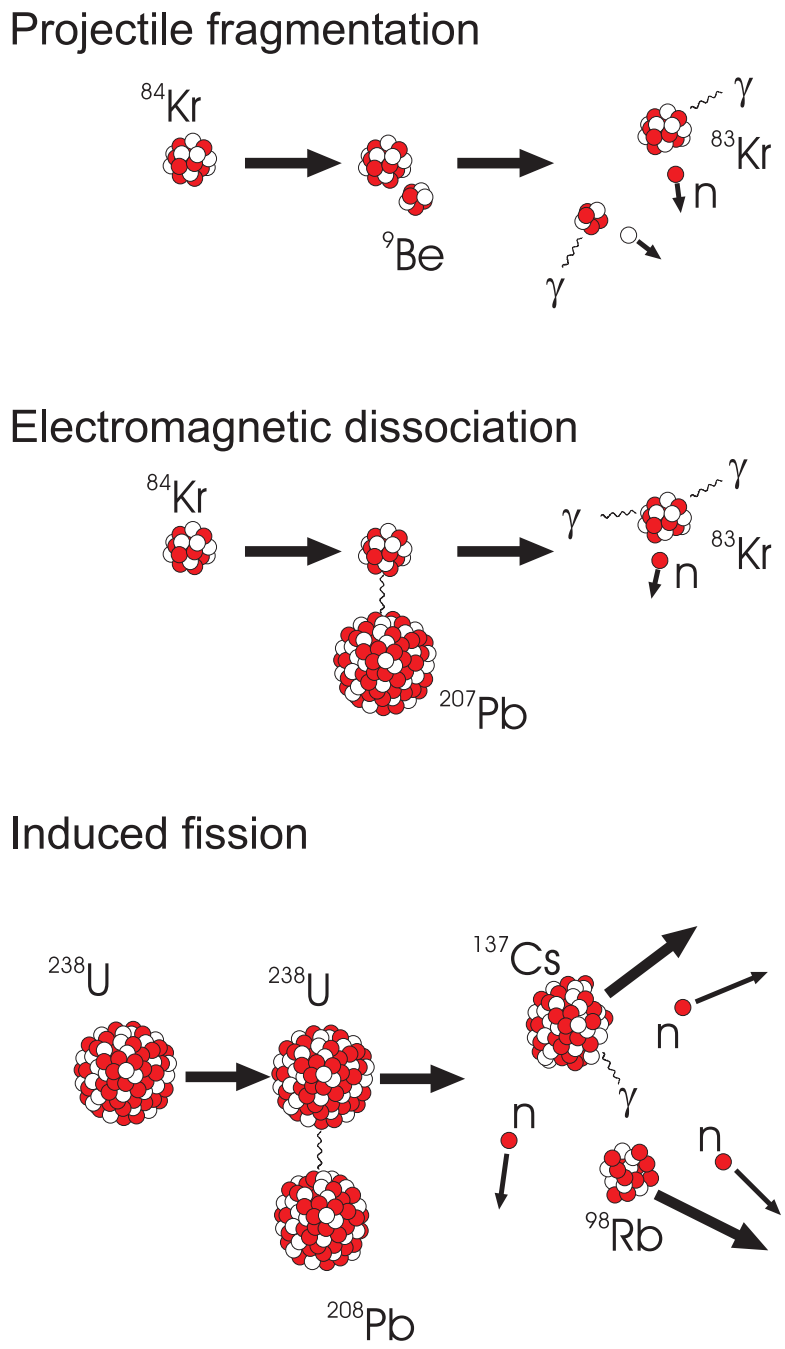

Figure 2.3: Important nuclear reactions using the in-flight method. In the projectile fragmentation process heavy ions colliding with lighter target ions lose nucleons by shearing them off. Projectiles interacting with another ion of the target by Coulomb interaction, the projectile gets excited and emits photons and nucleons in the dexcitation process. This process is called the electromagnetic dissociation. For heavy projectiles it is possible that the electromagnetic excitation energy or a close collision is high enough to induce a fission process. The projectile mainly breaks apart into two main fission products while the rest of the energy is carried away from single nucleons and photons.

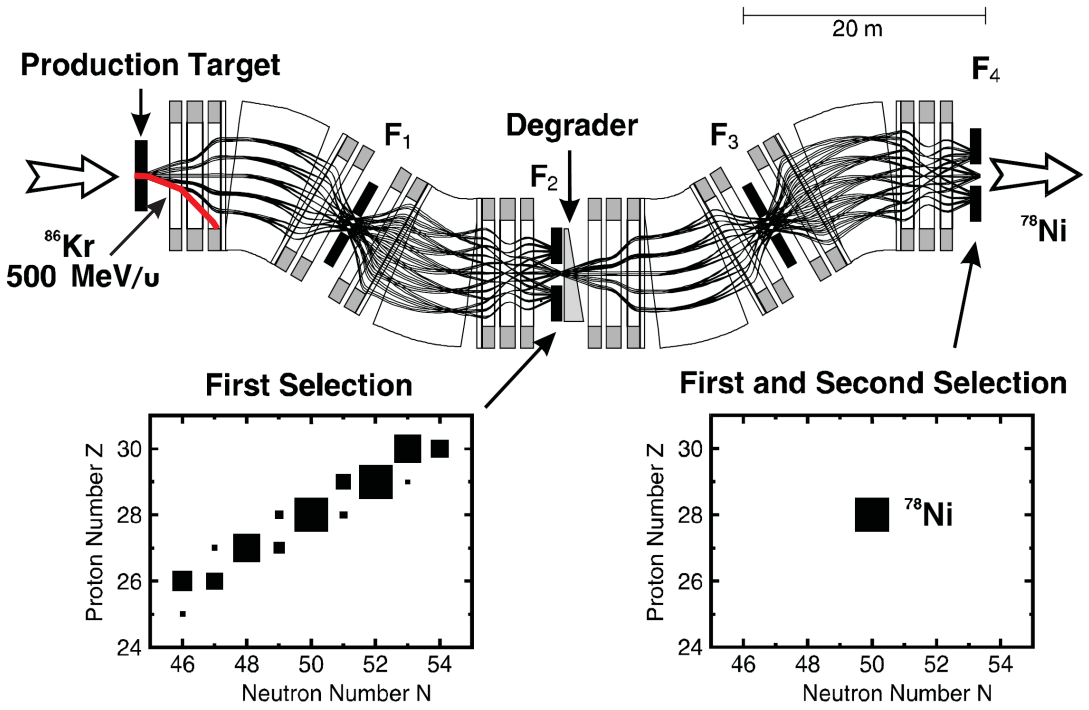

Figure 2.4: Principle of the ion separation process at the Fragment Separator (FRS). The first step is the selection of ions with same momentum at F2. In the focal plane a degrader is installed which will lead to an energy loss of the ions depending on their proton number. The change in energy makes it possible to select an monoisotopic ion beam at the second stage of the FRS (F4).

2.2 Methods for Mass Measurement

There exist two classes of methods to measure the masses of nuclides. One concept is the direct measurement of the masses, for example in ion traps by measuring the revolution frequencies in magnetic fields. The other concept is the indirect measurement of the masses by the reaction value (Q) measurement of a nuclear process.

2.2.1 Q-Value Measurements

The Q-value of a reaction is defined as the difference of the rest mass in the in- and out channel of the reaction. The reaction value Q is identical to the excess of kinetic energy.

$$Q = (m_{In} - m_{Out})c^2 \tag{2.1}$$

The *Q*-value can be determined by measuring the energy in the incoming and the outgoing channel. To determine the mass of a nucleus all other masses and energies must be known.

The disadvantage of this method is that for calculating the correct mass the decay scheme of the exotic nuclides needs to be known which is unknown. An other point is that it is necessary to detect all the energies in the outgoing channels, which includes the detection of all particles like γ-rays, α-particles and electrons.

The *Q*-values for α and proton decays are much easier to measure than for β-decay because of the much sharper energies compared to the β-decay. The *Q*-value for the β decay needs to be extracted from the endpoint of the β-spectrum which causes the largest uncertainties in the Q-value evaluation. The typical precision that is achievable with this method are 10 keV for α-decay dominated nuclides up to 1 MeV for nuclides decaying via β decay.

2.2.2 Ion Traps

Very precise mass measurements are possible with Penning traps. In Penning traps ions are confined by a magnetic field in the radial direction while a quadrupolar electric field stores them in axial direction (fig. [2.5]). The combination of the electromagnetic fields determines the ion trajectory in the trap. The motion of the ion can be divided into three main motions, the reduced cyclotron motion with frequency ω_+, the magnetron motion ω_- and the axial motion ω_z. The cyclotron frequency ω_c can be derived from the motion of a charged particle with charge q and mass m in a homogeneous magnetic field B.

$$\omega_c = \frac{q}{m} B \tag{2.2}$$

Therefore it can be seen that a determination of the cyclotron frequency yields the mass-to-charge ratio and therefore the mass of the ion species. It is important no note that the cyclotron frequency is related in the following way to the reduced cyclotron and magnetron frequency.

$$\omega_c = \omega_+ + \omega_- \tag{2.3}$$

Two different methods of measuring the cyclotron frequency are available at the moment, fourier transform ion cyclotron resonance (FT-ICR) and the time-of-flight ion cyclotron resonance (TOF-ICR) method. The FT-ICR method is based on the fourier transformation of the induced current on the electrode caused by the ions moving in the trap. This method is only applicable for many ions or high charge states in the trap. The TOF-ICR method is based on measuring a time-of-flight resonance curve from which the cyclotron frequency and therefore the mass can be determined. This method is also applicable for single ions and therefore it is the method for measuring exotic ions. The

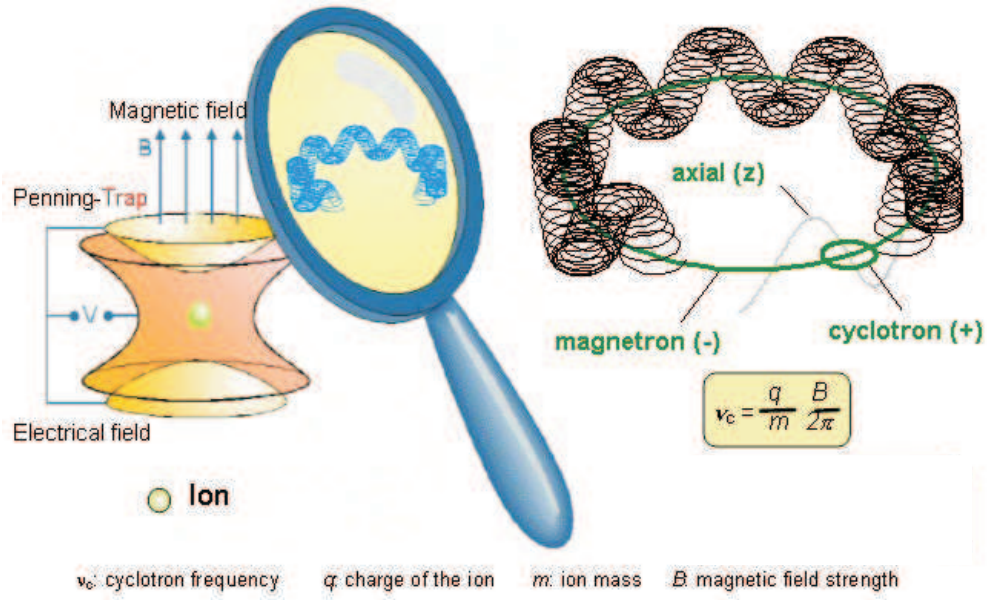

Figure 2.5: Overview of the basic ion motion and operation of a Penning trap. The ring electrode stores the ions in axial direction while an axial homogeneous magnetic field stores them in radial direction. (Figure from www.titan.triumpf.ca)

ion gets excited in the trap by an electric radio-frequency. If the excitation frequency is close to the cyclotron frequency the radial amplitude of the ions motion increases. Before describing the aspect of ejecting the ions a further important physical effect needs to be explained. A charged particle moving on a closed circle has a magnetic momentum $\vec{m}_m$ which is dependent on the mass-to-charge ratio, the gyromagnetic ratio and the angular momentum. So a particle in the trap has a higher magnetic momentum if it moves on an outer orbit. After exciting the ion and moving it on an outer orbit it can be ejected out of the trap. Directly after the ejection out of the hole the ion passes trough an inhomogeneous region of the magnetic field. The inhomogeneity of the magnetic field in combination with the magnetic momentum leads to a force that accelerates the ion after ejection.

$$\vec{F} = -\vec{m}_m \nabla \vec{B} \tag{2.4}$$

The time-of-flight of the ion is measured compared to the ejection time with a detector. Applying different resonance frequencies the ion has different orbits and therefore a different initial magnetic momentum and so different time-of-flight. If the correct cyclotron frequency is applied the maximum radial amplitude and so magnetic momentum is reached which leads to the smallest time-of-flight. Typical accuracies of this method are on the order of keV, allowing very precise measurements. The disadvantage of this method is that the measurement time is about one second to reach a high mass precision. This limits the lifetime measurement for very exotic ions with lifetimes

shorter than a second.

2.2.3 Schottky Mass Spectrometry

The Schottky mass measurement is one of the mostly applied methods for mass measurements of nuclides at the experimental storage Ring (ESR) [Fra-87], [Gei-92] at GSI. The method is based on the revolution frequency measurement of specific ions in the ring.

The ions in the ring are cooled using an electron cooler [Ste-96]. The electron cooler creates an electron beam that can be overlapped with the revolving ions in the ESR. The electron beam forces the ions to move within a specific velocity with a velocity spread as small as 10^{-6} [Ste-96] which is given by the average electron beam velocity. The cooling procedure normally takes about a second.

For Schottky mass spectrometry the ring is operated in the so called standard mode which means that ions with different mass-to-charge ratio move on different trajectories and so have different revolution frequencies (fig. [2.6]). The measurement of the revolution frequency is done without destroying the ions. For this detection so called Schotty electrodes have been developed [Bor-74]. These plates are arranged like an ideal capacitor. Every time an ion passes between the plates it influences charge on the plates [Bec-90]. This small signal can not be measured within one turn. But because the ions can be stored in the ring for multiple turns in the ESR one can divide the noise spectra into its frequenciy components (FFT) [Pres-92]. A high abundance at a specific frequency that corresponds to the mass-to-charge ratio of the ion is observed. Further peaks with smaller intensity can be seen at higher harmonics of the frequency.

The measurement is very effective because the injection and simultaneous mass measurement of more than hundreds of ions is possible (fig. [2.7]). So it is likely to inject known nuclides which can be used for a calibration of the frequency to the mass-to-charge ratio. The disadvantage of this method is that the cooling time is about some seconds. Therefore this method is only applicable for nuclides with life times longer than the cooling time. It is also important to take care that the mass difference of ions moving simultaneously in the ring is larger than 200 keV. Otherwise these close lying masses have a correlated motion in the ring which shifts the measured frequency and so the mass to a wrong value [LitY-03]. The mass measurement accuracy reachable at the moment is about $5 \cdot 10^{-7}$ [LitY-01] with a mass resolving power about $2 \cdot 10^{6}$.

2.2.4 Isochronous Mass Spectrometry

In order to measure smaller lifetimes of exotic nuclides down to 50 μs the experimental storage ring is operated in an other ion optical setting that differs significantly from the standard mode. The ring is operated in the isochronous mode. This means that the revolution time of the ions is independent from their initial kinetic energy. This offers

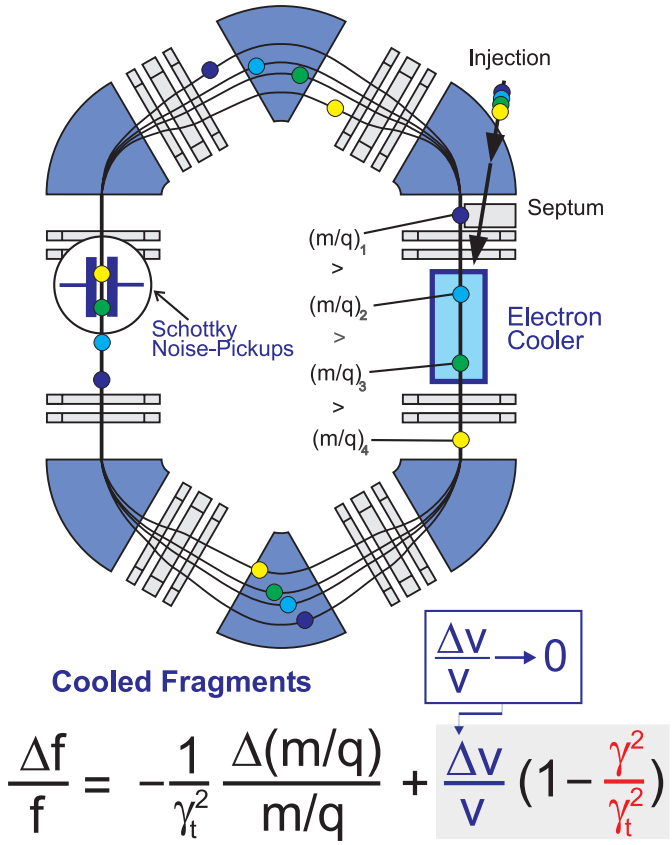

Figure 2.6: Principle of the Schottky mass measurement method of the ESR. The filled circles represent ions with different m/q while the lines show their trajectories. The ions velocity spread is decreased with the electron cooler. Ions with larger m/q have a larger pathlength in the ring therefore their revolution frequency is smaller than for ions with smaller m/q.

the advantage that the so called “hot fragments” can be injected into the ring and do not need to be cooled before the measurement.

The ion optical setting sends ions with same m/q but different energies onto different trajectories (fig. [2.8]). The faster ions have a longer path to travel than the slower ones so that the ions still have the same revolution frequency. The revolution frequency of each ion is measured by a time-of-flight detector in the ESR. At each turn the ions pass through a foil where secondary electrons are created. These electrons are bent onto a micro channel plate detector which produces a time signal.

This method has the big advantage that no cooling is necessary. So the life time measurement is limited by the transport time from the production target to the ESR and the necessary number of about 100 revolutions of the ion in the ring. With this method exotic nuclides with life times down to 50 μs are accessible. The accuracy of this method

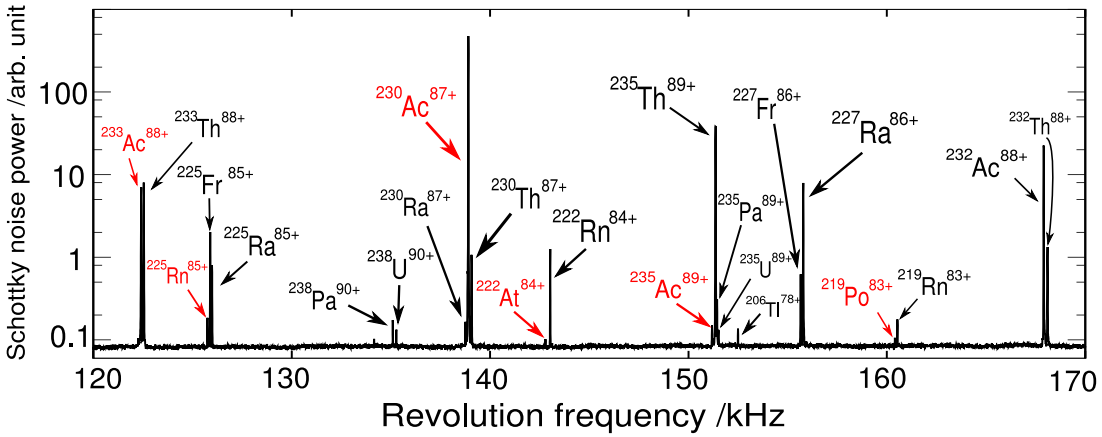

Figure 2.7: Part of a typical frequency spectra by using the Schottky mass measurement method. The spectra is created applying a Fourier transformation to the taken Schottky noise spectra. While the black peaks show known masses the red peaks show new measured masses. [Chen-08]

is about $1 \cdot 10^{-6}$.

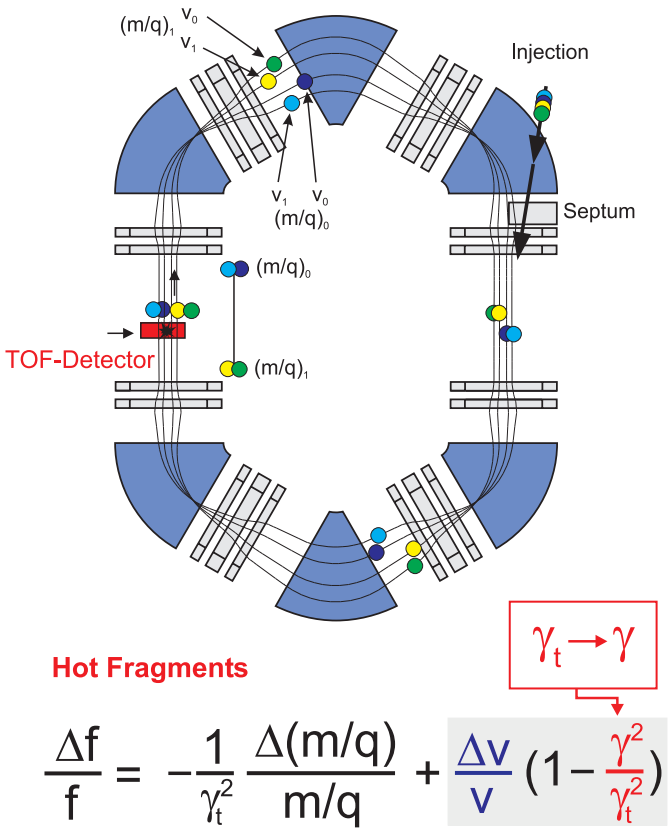

Figure 2.8: Principle of the isochronous mass measurement method. The different circles represent ions with different m/q and the lines their corresponding trajectories. Ions with different m/q and momentum are injected. The ion optics of the storage ring is set into the isochronous mode that makes it possible to measure the masses directly after the injection while having no further ion beam preparation. Ions with same m/q but different energy move on trajectories with different lengths so that the revolution time stays the same independent from the initial energy.

3 Basics of Isochronous Mass Spectrometry

The isochronous mass measurement method is capable of measuring nuclear masses with lifetimes down to 50 μs. No other method allows the measurement of short lifetimes with an accuracy of about 300 keV. The isochronous mass measurement method is a typical method used in storage ring experiments. The method is based on the fact that the revolution frequency of ions with the same mass-to-charge ratio is independent from their initial velocities. Therefore the storage ring needs to be set in this special ion optical mode. To measure the revolution frequencies a time-of-flight detector is used that is based on a conversion-foil detector principle. Ions pass the foil at each turn and create secondary-electrons in the foil. These electrons are bent onto a micro channel-plate detector by a combination of electric and magnetic fields. Each electron bunch imping on the MCP-detector creates a measurable signal that is used to determine the revolution frequency of the ion. To understand the overall process of the measurement method the process of ion motion in the storage ring, the creation, transport and detection must be examined. In the following sections all important physical basics of these processes are presented. The next section is focused on a general description of ions moving in a storage ring. Therefore a basic first order derivation of the mass-to-charge ratio dependence from the initial velocity spread ions of the ions, an ion optical factor and the revolution frequency spread in an ideal storage ring is given.

3.1 Principles of Isochronous Mass Measurement

The revolution time T of a stored particle with mass m and charge q depends on the velocity v and the path length L.

$$T = \frac{L}{v} \tag{3.1}$$

The total differential divided by T of this equation is given by

$$\frac{dT}{T} = \frac{\partial T}{\partial L}\frac{dL}{T} + \frac{\partial T}{\partial v}\frac{dv}{T} = \frac{dL}{vT} - \frac{dv}{Tv^2} = \frac{dL}{L} - \frac{dv}{v} \tag{3.2}$$

The dependence of the path length from the magnetic rigidity is given by [Bry-93]

$$\frac{dL}{L} = \alpha_p \frac{d(B\rho)}{B\rho} \tag{3.3}$$

while α_P is the momentum compaction factor which describes the path length change by changing the magnetic rigidity. The magnetic rigidity is given by

$$B\rho = \frac{m}{q}\beta\gamma c \tag{3.4}$$

while γ is the relativistic Lorentz factor and $\beta = v/c$. Substituting expression 3.2 in formula 3.3

$$\frac{dT}{T} = \alpha_P \frac{d(m/q)}{m/q} + (\alpha_P \gamma^2 - 1)\frac{dv}{v} \tag{3.5}$$

Using the following definition for the transition point of the ring

$$\gamma_T = \frac{1}{\sqrt{\alpha_P}} \tag{3.6}$$

so eq. 3.5 can be written as

$$\frac{dT}{T} = \alpha_P \frac{d(m/q)}{m/Q} + \left(\frac{\gamma^2}{\gamma_T^2} - 1\right)\frac{dv}{v} \tag{3.7}$$

Equation 3.7 shows the principle of this mass measurement technique. To get a relationship between the revolution time T and the mass-to-charge ratio the second term in eq. 3.7 needs to be canceled out. This can be done by decreasing the velocity spread $\Delta v/v$ as it is done by the Schottky method. The other option is to vary the transition point γ_T or the energy γ of the particles to cancel out the expression in the brackets ($\gamma = \gamma_T$ [Wol-87]).

The typical value for γ_T in the standard mode is $\gamma_T = 2.5$ for the ESR at GSI. This value of operation is not useable from the applied side because a lot of ions would be out of the adjustable magnetic rigidity of the ESR (fig. [3.1]). This means that only a small portion of different exotic ions could be stored. So the value of $\gamma_T = 1.4$ is used by adjusting the quadrupoles in the ring to make the storage of more exotic nuclides possible [Dol-96]. To test the isochronicity of the ring a primary beam in conjunction with the electron cooler can be used while the ions revolution frequency can be measured with the Schottky pickups. Changing the electron cooler voltage the velocity of the ions in the ring is varied. From this measurement the so called “isochronicity curve” can be calculated which shows if the revolution frequency is really independent from the initial velocity (fig. [3.2]). But nevertheless the revolution frequency changes a little bit with the initial velocity which is caused by higher order field corrections of the magnets and focussing elements (fig. [3.2]). Another important point is that the isochronicity is in principle only valid for a specific mass-to-charge ratio and the quality of the isochronicity changes for different mass to charge ratios and needs to be corrected in the analysis.

Because of the energy loss of a particle caused by travelling through the foil the momentum changes over each turn. So the particle’s trajectory moves in the average to the outside of the beam pipe until it hits onto the wall.

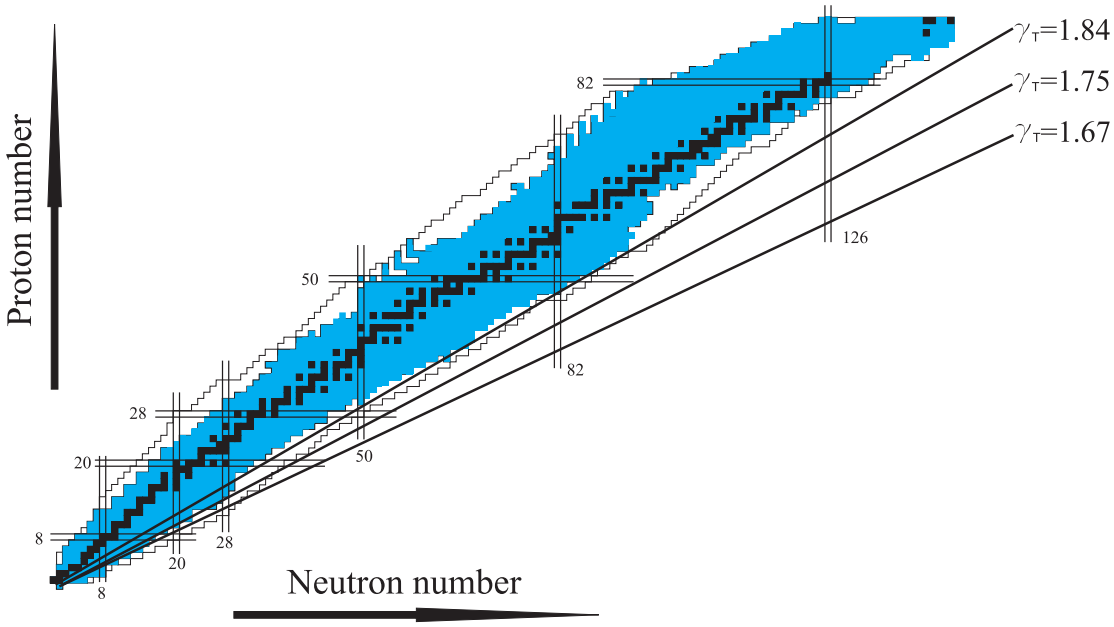

Figure 3.1: Chart of nuclide that shows the region of ions that can be stored by using different transition points γ_T for a magnetic rigidity of 10 Tm. Nuclide on the right side of the straight lines indicate the region that can not be stored. The picture shows clearly that only a small portion of neutron rich nuclide can be stored while keeping the transition point to the standard value $\gamma_T = 2.5$ [LitS-08].

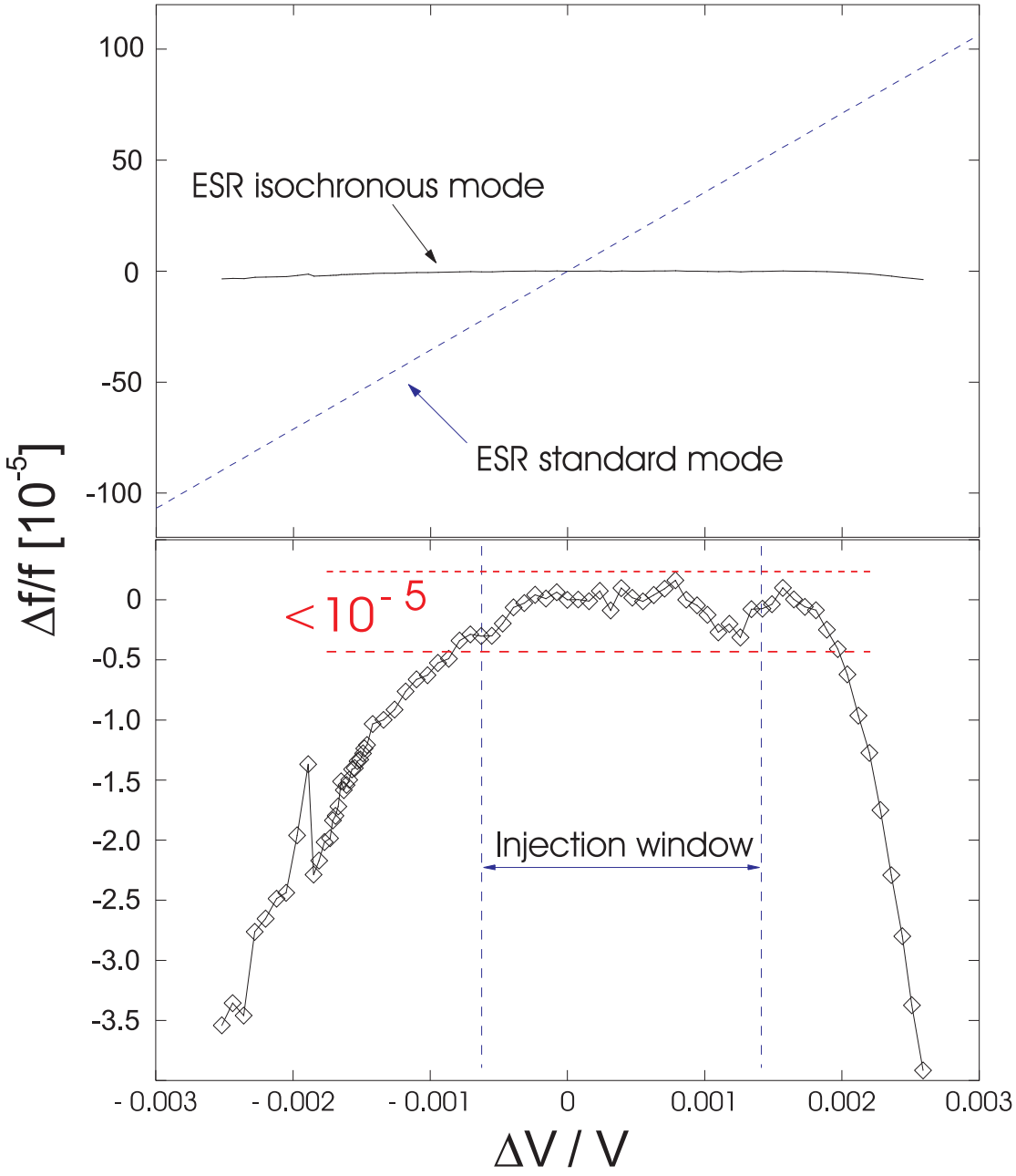

Figure 3.2: Isocronicity curve measured by using the Schottky plates and the electron cooler. The graph shows the change of the revolution frequency in dependence of the particle velocity. In the standard-mode the revolution time changes proportional to the velocity while for the isochronous mode the revolution time stays roughly constant over a broad range of velocities. [Sta-02]

3.2 Motion of Stored Ions in the ESR including Atomic Interaction

3.2.1 Motion of Charged Particles in Electromagnetic Fields

The behavior of charged particles in electric and or magnetic fields can be described by the electric and magnetic forces acting on them. The trajectory of the particles can be solved by using the Lorentz-force.

$$m\frac{d^2\vec{r}}{dt^2} = q\left(\vec{E} + \frac{d\vec{r}}{dt} \times \vec{B}\right) \tag{3.8}$$

So knowing the electromagnetic fields $\vec{E}$ and $\vec{B}$ and the initial conditions $\vec{r}(t_0)$ and $\vec{v}(t_0)$ of the particles the trajectory for any mass m and charge q can be calculated. This is a straight forward assumption to start with and is used in conjunction with a numerical solver for electromagnetic fields based on the Finite Element method (FEM).

The numerical method is used to calculate the electromagnetic fields for a given problem and to solve the equation of motion for the trajectories for multiple particles with different initial condition. But the disadvantage of using the real electromagnetic fields is that the calculation time for many particles or for a big volume to solve increases dramatically. So for larger systems like in ion optics another concept is used to describe the motion of charged particles as a beam in a less time consuming way. Therefore the concept of transfer matrices was developed to describe the development of average beam properties and their spread over time and space. To describe the behavior of ions in the storage ring the matrix description is used while for the smaller time-of-flight detector the numerical field solving method is used.

3.2.2 Fundamentals of Ion Optics

The motion of particles in an ion optical system is described by a reference trajectory and their standard deviations. But for the calculation another base of coordinates than the cartesian coordinates are used. Typically coordinates are relative to the reference particle trajectory. To describe the development the following coordinates are defined

$$X \tag{3.9}$$

$$\frac{p_x}{p_0} = a \tag{3.10}$$

$$Y \tag{3.11}$$

$$\frac{p_y}{p_0} = b \tag{3.12}$$

$$l = v_0(T - T_0) \tag{3.13}$$

$$\Delta = \frac{p/q - p_0/q_0}{p_0 q_0} \tag{3.14}$$

while all values with index 0 are the properties of the reference particle [Wol-87]. X and Y describe the transversal positions of the beam, a and b the corresponding angles, l the time-of-flight difference to the reference trajectory and Δ the relative deviation of the momentum.

If a particle beam moves into an ion optical system like a magnet it will change its trajectory caused by the magnetic force. The change of the initial coordinates compared to the coordinates after travelling through the system can be described by a transformation matrix. So the new final properties of the beam are simply calculated by a multiplication of the initial properties with a transformation matrix.

A system of different ion optical elements is given by the product of the transfer matrices. Each of the parameters in the matrix tells us specific properties of the transformation of the particle beam.

$$\begin{pmatrix} X \\ a \\ Y \\ b \\ l \\ \Delta \end{pmatrix}_{final} = \begin{pmatrix} (X,X) & (X,a) & (X,Y) & (X,b) & (X,l) & (X,\Delta) \\ (a,X) & (a,a) & (a,Y) & (a,b) & (a,l) & (a,\Delta) \\ (Y,X) & (Y,a) & (Y,Y) & (Y,b) & (Y,l) & (Y,\Delta) \\ (b,X) & (b,a) & (b,Y) & (b,b) & (b,l) & (b,\Delta) \\ (l,X) & (l,a) & (l,Y) & (l,b) & (l,l) & (l,\Delta) \\ (\Delta,X) & (\Delta,a) & (\Delta,Y) & (\Delta,b) & (\Delta,l) & (\Delta,\Delta) \end{pmatrix} \cdot \begin{pmatrix} X \\ a \\ Y \\ b \\ l \\ \Delta \end{pmatrix}_{initial} \tag{3.15}$$

The method is typically used for ion optical calculations of complex systems like beam lines, storage rings and synchrotron. The advantage of this description is that the calculation of the electromagnetic fields is less time consuming than in a numerical calculation. Furthermore special properties of the system can be directly seen in the matrix-values. Each of the matrix elements describe the operation of the system. The matrix elements describes for example the beam spot size, the time of flight, the energy, momentum or angle after the transformation. It is also straight forward to fix properties of an intended behavior of the system by fixing the specific matrix elements. Therefore these parameter stay constant while the other parameter are changed.

3.2.3 Energy Loss of Charged Particles in Matter

A charged particle that travels through matter interacts with the target's electrons and the nuclides by different processes. During these processes the projectile loses energy. Main processes occurring are elastic scattering processes, inelastic processes like ionization, excitation and charge exchange between the projectile and the target.

Typically the energy loss process can be roughly divided into different regimes where different processes dominante (fig. [3.3]). Up to 0.1 MeV/u the nuclear interaction can get dominant over the electronic interaction. This process describes the elastic collisions between the projectile and the targets nuclides. In this regime the stopping power is proportional to the projectiles velocity. A more detailed description can be found in [Lind-61]. With increasing kinetic energy the contribution of the electronic interaction increases and drops for further energies because of the decrease of the ionization and excitation cross-sections for higher energies. In the third region an increase of the energy loss can be seen again that is caused by deceleration radiation losses and relativistic effects. Typically the minimum of stopping power is reached at about $3M_{Projetcile}c^2$. The so called Bethe regime is mainly dominated by interactions of the ion with a quasi-free electron. The formula can be used to calculate the energy loss per pathlength dx of an ion with charge Z_P travelling through a solid target with charge density n_T. The Bethe formula [Bet-30] is based on the first order Born approximation of describing the scattering process. Including relativistic corrections [ScheiD-96], [Sg-98] the relativistic Bethe formula can be derived.

$$\left(\frac{dE}{dx}\right)_{Bethe,rel.} = \frac{4\pi Z_P^2 e^4 n_T}{m_e c^2 \beta^2}\left[L_{Bethe} - ln\left(1-\beta^2\right) - \beta^2\right] \tag{3.16}$$

with $L_{Bethe} = ln(\frac{2m_e c^2\beta^2}{I})$. The average ionization potential of the target is given by I, while β is the relative speed of light and γ the Lorentz factor. The energy loss caused by ionization and excitation is averaged. For further discussion the variable $C = \frac{4\pi Z_P^2 e^4 n_T}{m_e c^2 \beta^2}$. But it should be noted that the Born approximation is only applicable for small pertubations. Therefore the Bethe-formula needs to be corrected for heavy ions that cause larger pertubations. Therefore the Bethe formula is only valid for the condition [ScheiD-96]

$$\frac{\sqrt{Z_P}\alpha}{\beta} \ll 1 \tag{3.17}$$

with α being the fine structure constant. A higher accuracy of the description of the stopping power can be achieved [Schei-94], [Schei-96] by using a model developed by Linhard-Soerensen which yields deviation to experimental data that are smaller than 1%. Especially for heavy ions where the condition in equation 3.17 does not hold, the Linhard-Soerensen theory must be used if accurate stopping powers are necessary. This theory is based on solving the Dirac equation for the scattering processes and gives

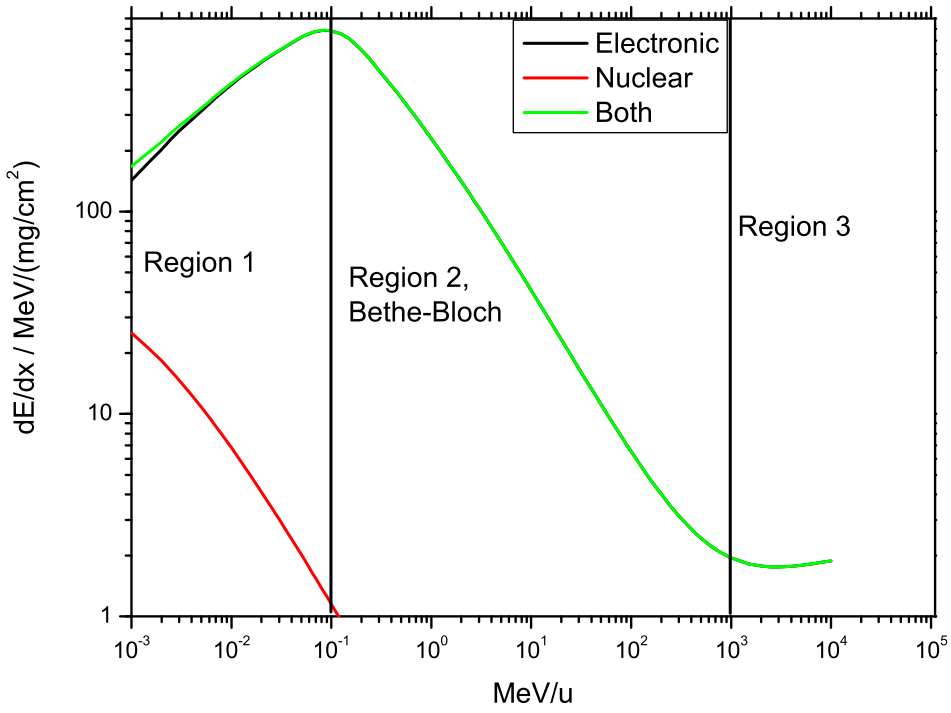

Figure 3.3: Calculated Stopping power of a proton in a carbon target in dependence of the projectiles specific energy. For low specific energies the stopping power has additional contributions by the elastic process with the targets nuclides while for higher energies the electronic process dominates. [Pstar]

corrections to the Bethe formula. The solution of the stopping power for the description within the Linhard-Soerensen theory can be written in the following way

$$\left(\frac{dE}{dx}\right)_{L,S} = C\left[L_{Bethe} + \Delta L_{L,S} - \frac{\delta}{2}\right] \tag{3.18}$$

while the third term in eq. 3.18 incorporates the fermi-density effect that accounts for the dielectric polarization of the stopping power at relativistic velocities. The Linhard-Soerensen term $\Delta L_{L,S}$ includes the effect of spin dependency of the cross-sections (Mott-cross-sections) and the relativistic effects and also the so called non-relativistic Bloch correction.

Another option to calculate the energy loss is by simulating the tracking of an ion and its collisional processes step by step. The calculation of the track of many ions the

average behavior of the variable interested in and its standard deviation can be derived. This method is known as a Monte Carlo calculation technique.

The given values of the stopping power mentioned in this work are calculated with the ATIMA code [At]. This code is based on the Linhard-Soerensen theory and yields accurate stopping powers for fast heavy ions.

3.2.4 Charge Exchange of Particles in Matter

Ions that pass through the foil are also able to interact with the target through charge exchange processes. Therefore the main charge exchange processes are shortly presented and discussed.

The charge exchange is described by two main processes the so called radiative electron capture (REC) [Eich-07]and the non-radiative electron capture (NRC) [Schei-98]. The radiative electron capture can be described by the time reverse process of the photoeffect. Therefore the electron is assumed to be in a quasi free state and gets caught into a bound state of the ion. While going from the quasi continuum state to the bound state a photon carrying away the energy difference is released. The cross section σ_{REC} of this charge exchange process is directly proportional to the charge state of the target ($\sigma_{REC} \sim Z_T$).

The NRC can be described by a three body interaction where the bound state electron interacts with other electron shells of the atom. The electron jumps from one bound state of one ion to another lower bound state of the other ion while the momentum difference is carried away by the target. This process is a non radiative process and its cross-section σ_{NRC} is proportional to Z_T^5 and Z_P^5 ($\sigma_{NRC} \sim Z_T^5 Z_P^5$).

Both processes are dominant in different projectile energy regions. While the NRC is dominant in the energy range up to 90 MeV/u the REC is dominant in the range of more than 100 MeV/u. So the main process that could lead to electron capture is the REC in the range of $300 - 400$ MeV/u.

Calculation with the program CHARGE [Schei-98] showed that the probability for a projectile electron capture from the target of carbon is about $1.692 * 10^{-6}$ for thickness of 10 $\mu g/cm^2$ or by the caesium iodide coated carbon foil $5.14 * 10^{-5}$ for one passage of the foil. Considering multiple passages of the ion through the foil it shows that the probabilities are so small that they start to contribute at turn numbers where the ion optical limitations are even more dominant ($n \approx 1000$). So in further discussion the charge exchange is excluded.

But the discussion of the charge exchange already shows that by going to a pure carbon target the charge exchange probability will be even further decreased by a factor 10.

3.2.5 Motion of Ions in the ESR

To understand and optimize the mass measurements of the ESR in the isochronous mode a detailed understanding of the ions motion in the ring is necessary. A very interesting parameter to know is the survival probability of ions moving in the ring and their development over time. To simulate the expected performance of all of the ongoing physical effects need to be taken into account. The effects can be mainly divided into ring loss effects and energy or charge changing effects. The charge changing effects will not be considered in the further discussion because of the charge exchange probability being to small as discussed in chapter 3.2.3.

3.2.5.1 Simulation

A Monte Carlo method is used to calculate the survival probability of the ions for different turn numbers. Therefore the ion optics needs to be considered. It is calculated using the GICOSI [Gic-87] program while the electromagnetic fields are imported into the programm MOCADI [Schw-88] that allows a Monte Carlo calculation. The fields calculated by GICOSI are based on the transfer matrix descriptions. All dipole magnets, quadrupols, vacuum and foil apertures of the ESR are implemented into the calculation. The aperture size at the position of the detector is limited by the foil dimension of a diameter of 4 cm. Sextupoles and other high order elements are not considered because of having minor effects on the survival probability and allowing an easier model. Higher orders only start to play a role for the timing properties. Analytical expressions that consider the fringing fields of the magnetic dipoles are used for the calculation. The effect of angular straggling of the ions in the foil is implemented by assuming a Gaußian-distribution. The most dominant effect is the change of the trajectory caused by the energy loss of the ion passing the foil. Therefore the energy loss at the foils position for $^{64}Ni^{28+}$ at 372 MeV/u is added by using a calculated value ΔE from the ATIMA code. To include the statistical fluctuation of the energy loss the energy straggling is also implemented ($dE/E = -3.16935 \cdot 10^{-6}$). The foil considered is a $20\mu g/cm^2$ carbon foil with $10\mu g/cm^2$ of CsI coated on each side of the carbon carrier. The ATMIA codes yields a value of $\Delta E = 75.5$ keV per passage of the foil.

The time development of an ion bunch of 10000 ions is investigated over the turn number by repeating the calculation for each turn with new updated ion properties after the foils position. To calculate the motion of bare Ni-ions it assumed that the initial energy spread is $\pm 0.2\%$ while the initial emmitance is estimated to be about 10 mmrad for a matched beam. The energy of the ions was set to be 372 MeV/u as in the experiment with the stable Ni-beam. An ion that is injected close to the momentum acceptance boarder or very far from the ideal trajectory can get lost by simply hitting the wall. These loss are expected to occur especially at the beginning when a bunch of ions with

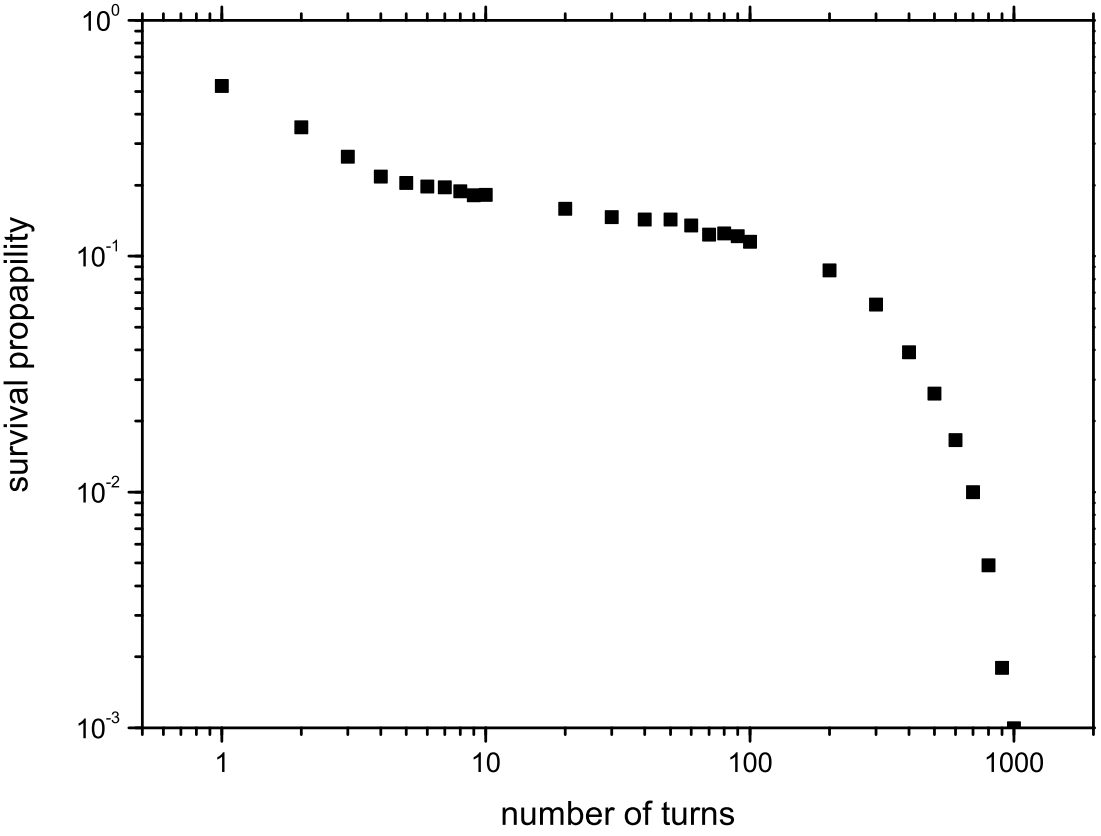

Figure 3.4: Result of the calculated ion survival probability for 372 MeV/u $^{64}Ni^{28+}$ ions in the ESR for a 20 $\mu g/cm^2$ carbon foil and CsI coating in dependence of the turn number. In the first few turns the effect of phase space cutting of ions in the ring is clearly seen. At about 5 to 10 turns the ion loss is dominated by the energy loss of the ions caused in the foil [Wei-07].

a big momentum spread is injected (fig. [3.4]). But never the less ions also get lost during further turn numbers. The energy an ion loses at every passage through the foil will shift the ions trajectory into the direction of the beam pipe. So at one point the ion optical setting is not be able to hold it on an stable trajectory anymore. During the process of the foil passage the ion will also get slightly scattered. Simulations also showed that the influence of ion scattering in the foil on to the ion survival probability is minor.

3.3 Electron Generation, Transport and Detection

In this section the time-of-flight detector used for the detection of the ions and the determination of the revolution-frequency is examined in detail. Ions that pass through

the foil release secondary electrons that are transpored by a combination of electric and magnetic fields onto micro channel plate detectors. To understand the detector in more detail and optimize the performance parameters like timing and electron transport efficiency all stages from the creation of electrons in the foil and the transport and detection need to be examined. The following sections give a detailed background on the analytical and numerical solved electron transport behavior of the electrons in the detector. The basic physics of secondary electron creation in foils by ions and the working principle of micro channel plates is explained.

3.3.1 Time-of-Flight Detector

To measure the revolution frequencies of the ions, a detector is necessary that detects single ions without destroying them. This is done by an isochronous foil detector (fig. [3.5]). This type of detector was conceptually developed by Bowman and Heffner [Bh-78]. A more detailed description of the mechanical properties of the currently installed detector can be found in [Rad-94] [Troe-93] [Troe-92].

The detector includes a CsI coated carbon foil where ions release secondary electron when they pass through the foil. The electrons are transported by a crossed electric and magnetic field onto a micro channel plate detector where the electrons are detected. The electric field is created by equidistantly spaced electrodes while the magnetic field is created by an external dipole magnet. The transport of the electrons is also isochronous which means that the time-of-flight from the foil to the micro channel plate detector is independent from the initial velocity of the electrons.

The detector is normally operated in a mode where the electrons created in the forward and backward direction are detected. Coincident signals of the forward and backward branch of the detector allow an easier identification of the passage of an ion through the foil. The ions passing through the foil experience an energy loss at every passage through the foil. Typical values of the energy loss are on the order of $50-100$ keV per turn which is very small compared to their total energy of some hundreds of MeV/u in online experiments.

3.3.1.1 Ideal Detector

The isochronous motion of the electrons from the foil to the micro channel plate detector is caused by a homogeneous electric field $\vec{E} = E\vec{e}_z$ crossed with a magnetic field $\vec{B} = -B\vec{e}_y$ [Troe-93]. The equation of force of a charged particle with charge q and mass m can be written as

$$m\frac{d^2\vec{r}}{dt^2} = q\left(\vec{E} + \frac{d\vec{r}}{dt} \times \vec{B}\right) \tag{3.19}$$

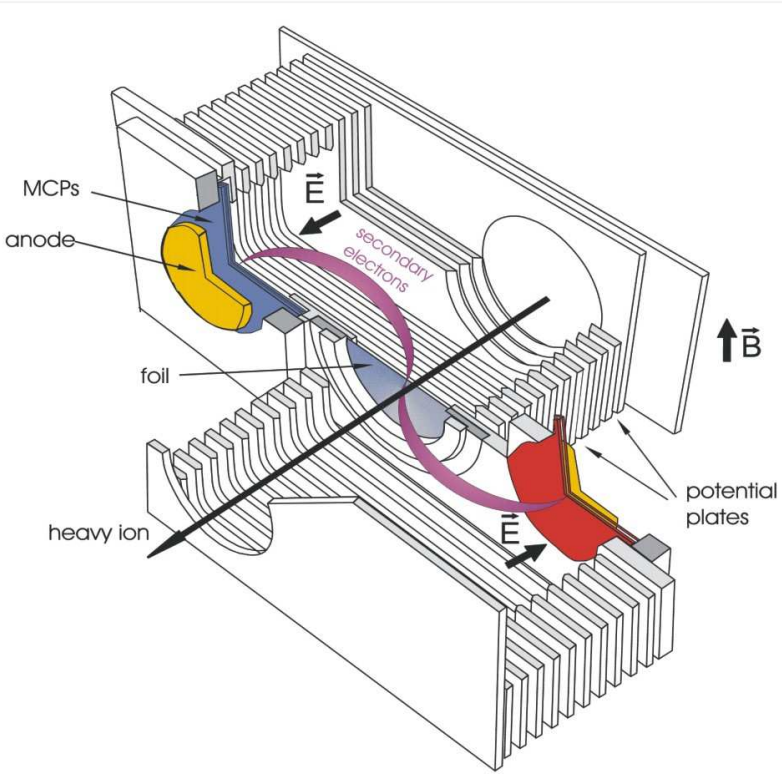

Figure 3.5: Scheme of the time-of-flight detector used for the isochronous mass measurement. Ions passing the foil release secondary electrons at the entrance and exit of the foil. These electrons are transported to a micro channel plate detector by a combination of electric and magnetic fields. The transport of the electrons in the detector is also isochronous. The secondary electrons imping on the MCP-detector is gained before they hit onto the anode which creates a measurable signal.

The direction of the homogeneous magnetic field is the negative y direction while the direction of the electric field is the x direction. So the vectorial equation (eq. 3.19) can be written in the cartesian component form as

$$m\frac{d^2x}{dt^2} = -q\frac{dz}{dt}B \tag{3.20}$$

$$m\frac{d^2y}{dt^2} = 0 \tag{3.21}$$

$$m\frac{d^2z}{dt^2} = q\left(\frac{dy}{dt}B - E\right) \tag{3.22}$$

Solving this coupled equations system (eq. 3.20, 3.21, 3.22) yields the solutions as

$$x(t) = x(0) - \frac{y_z(0)}{\omega}\left(1 - cos\left(\omega t\right)\right) + \frac{v_y(0) + E/B}{\omega} sin\left(\omega t\right) - \frac{E}{B}t \tag{3.23}$$

$$y(t) = y(0) + y_x(0)t \tag{3.24}$$

$$z(t) = z(0) + \frac{v_y(0) + E/B}{\omega} \cdot (1 - cos(\omega t)) + \frac{v_z(0)}{\omega} \cdot sin(\omega t) \tag{3.25}$$

with $\omega = eB/m_e$ being the cyclotron frequency. The trajectory is a so called Cycloid trajectory. From this knowledge the lateral distance can be calculated by neglecting the initial velocity into the z-direction.

$$D = x(T) - x(0) = \frac{2\pi m_e}{e} \frac{E}{B^2} \tag{3.26}$$

The maximum distance an electron travels into the z-direction is given by

$$z_{max} = \frac{D}{\pi} \tag{3.27}$$

The transport to the MCP is isochronous, which means that the time-of-flight is independent on the initial kinetic energy of the electrons. Faster electrons fly on a longer trajectory to compensate the velocity by distance to reach the detector at the same time of flight.

Micro channel plates are known to reach a plateau in detection efficiency at initial kinetic energies of 300 eV for electrons [Wiz-79]. But the derivatives of eq. 3.23, 3.24 and eq. 3.25 with respect to the time show that the initial starting velocity is the same as the imping velocity. So, to reach a higher velocity at the position of the MCP-detector a shift of the detector into the direction of the incoming electrons could help. The electrons hit with more energy but do not hit perfectly isochronously. Another method that can be used is to give them a higher initial velocity. This can be easily done by applying a more negative voltage onto the foil. The potential difference between the foil and the MCP defines the average kinetic energy the electrons hit the micro channel plate. Superimposed there is also the initial velocity distribution caused by the secondary electron creation process.

3.3.2 Finite Element Method

This is a method that is used to solve differential equations on arbitrary geometries even with time dependence. This method can be applied to almost all physical problems that can be described by a field theory like electromagnetic, mechanical, thermodynamical, fluid dynamical,... problems. Originally it was developed for calculations of stress of materials and structures. A broad application can still be found in this field today like in automobile and aerospace industry for the calculation of stress and fatigue of special parts and materials.

The finite element method is based on the earlier developed finite difference method. Using this method the volume is divided into equidistant points. Initial conditions of

some points are fixed and the values at the neighboring point can be calculated. This can be done by substituting $\frac{\partial f(x)}{\partial x}$ the differential expression in the physical equations with finite differences that makes it possible to calculate the values (see eq. 3.28).

$$\frac{\partial f(x)}{\partial x} \approx \frac{f(x_2) - f(x_1)}{x_2 - x_1} \tag{3.28}$$

All of these methods are based on the same first step. The geometry with which the physical equations shall be solved is divided into nodes (fig. [3.6]). Using the finite element method the nodes are grouped into elements like lines, triangles or tetrahedra. The problem that needs to be solved is defined accurately if the overall physical equation that describes the calculation method, concerning the neighboring points, and the boundary conditions are given. For example an electrostatic problem where the boundary condition is given by a Dirichlet condition. The potential is given on a special volume that creates an electric field distribution that can be calculated just by knowing the boundary condition and the responsible geometry.

So to solve an arbitrary differential equation of the form

$$\hat{L}u(x) = f(x) \tag{3.29}$$

defined on an interval $a \leq x \leq b$ with $\hat{L}$ being the differential operator the following approximation can be made [All-05].

$$u(x) \approx u_N(x) := \sum c_j \Phi_j(x) \tag{3.30}$$

while $\Phi_j(x)$ are the so called assumption functions that are linear independent and solve the boundary conditions, c_j are coefficients and $u_N(x)$ is the approximated function of the real solution $u(x)$. Approximations of the functions deviations to the exact solutions $u(x)$ are made. The deviation is simply the difference of both sides of the equations 3.29 and 3.30 is called the residuum R.

$$R := \hat{L}u_N(x) - f(x) = \sum_{j=1}^{N} \hat{L}c_j\Phi_j(x) - f(x) \tag{3.31}$$

The coefficients are calculated from the N equations with the weighting function $w_k(x)$.

$$\int_a^b w_k(x) R dx = 0 \tag{3.32}$$

Substituting the expression for R with equation 3.31 in eq. 3.32 yields

$$\int_a^b w_k(x) \left(\sum_{j=1}^{N} \hat{L}c_j\Phi_j(x) - f(x) \right) dx = \sum_{j=1}^{N} \int_a^b w_k(x)\hat{L}\Phi_j(x)dx c_j - \int w_k(x) f(x)\, dx = 0 \tag{3.33}$$

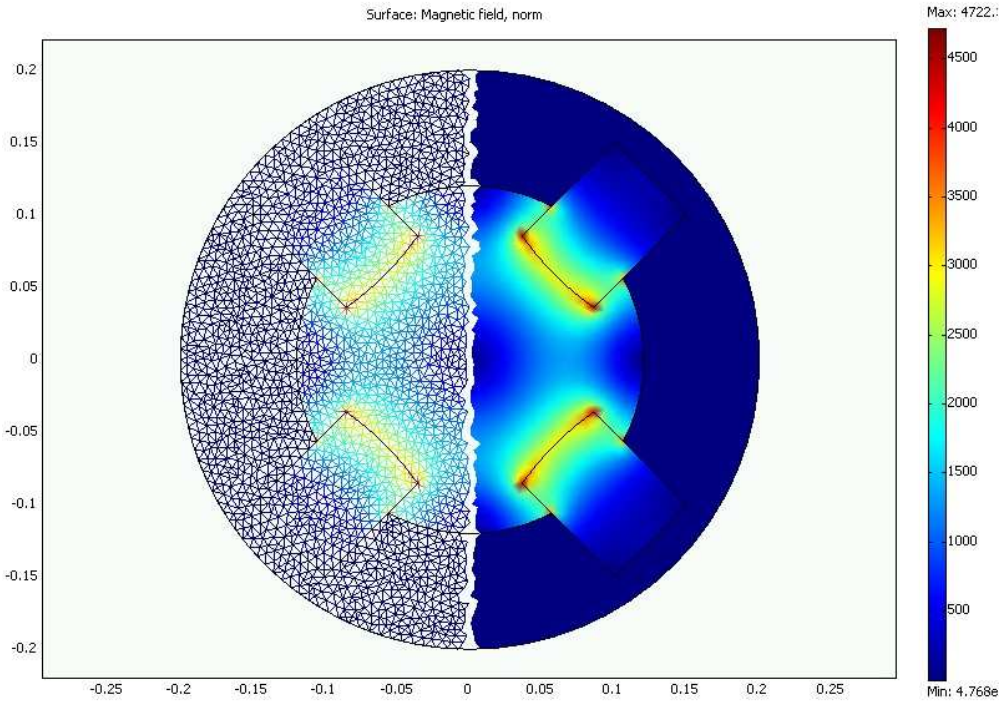

Figure 3.6: Color plot of a magnetic field solution (right) of a magnetic 2d quadropole calculated with the finite element software COMSOL and the corresponding mesh (left). The main boundary conditions that are set are the permanent magnetization of the electrodes.

and using the following definition:

$$(g,h) := \int_a^b g(x)h(x)dx \tag{3.34}$$

equation 3.33 can be written in the following way

$$\sum_{j=1}^{N} \left(w_k, \hat{L}\Phi_j\right) c_j = (w_k, f) \tag{3.35}$$

$$A \cdot \vec{c} = \vec{B} \tag{3.36}$$

This equations (eq. 3.36) symbolizes a linear equation system with unknown coefficients c_j. Reasonable weightening functions w_k can be calculated by minimizing the residuum. Another option that is widely used is the so called Galerkin method that assumes that the weighting function are equal to the assumption functions Φ_j [Bin-92]. This method showed improved convergence and better numerical precisions. Therefore

equation 3.35 can be written as

$$\sum_{j=1}^{N} \left(\Phi_k, \hat{L}\Phi_j\right) c_j = (w_k, f) \tag{3.37}$$

The next step is to choose the assumption functions Φ_j that connect each points. Typically the nodes are connected by polynomial functions that are just defined on a specific interval (so called finite elements). The coefficients are solved by a Gauss method [Gaus]. The advantage of the Finite element method is that it does not need structured or equidistant nodes. This makes the method more feasible to arbitrary geometrical structures with different length scales of interesting features.

3.3.3 Simulation of the Secondary Electron Transport

The transport of the electrons is simulated by using a Monte Carlo capable program so called Ion Trajectory Simulation Program ITSIM [Pla-01], [Wu-06]. This program is able to calculate particle trajectories for any analytical or numerical given electric-, magnetic field and gas flow field. The geometry of the detector is drawn in the COMSOL programm´[Com] by an implemented CAD-Program. Then the electric potential Φ for every electrode of the 3D geometry is calculated using the commercial finite element programm COMSOL by solving the Laplace equation.

$$\nabla\Phi = 0 \tag{3.38}$$

Afterwards the electric field is imported into the programm ITSIM (fig. [3.7]). The program COMSOL was tested before on analytical problems of electrostatic and magnetostatic problems and has given reasonable results down to an average relative error of 10^{-4} compared to the analytical solutions for 3D problems.

The 12 electrodes that produce the main electric field have relatively defined voltages because they are supplied by a voltage divider which is supported by two main voltages U^{++} and $U-$. The voltage drop caused by the voltage divider is already implemented into the field calculation (fig. [7.1]) before importing it into ITSIM. So it is possible to reduce this 12 electrodes to the main experimentally voltage sources U^{++} and U^{-} that support the voltage divider. The voltage divider is built in a way that it creates a linear dropping potential to get a constant electric field in the region where the electrons fly. Two more important potentials implemented are the voltage on the foil U_{Foil} and the voltage onto the micro channel detectors first plate U_{MCP}.

To check the need of the comprehension of the real magnetic field distribution of the dipole magnet the inhomogeneity and the absolute values of the magnetic induction B are checked by measurements with a Hall probe and a finite element calculation with the program COMSOL (fig. [3.9, 7.3, 3.8]). To solve the magnetostatic problem with given external current density $\vec{J}$ on the coils and a magnetic permeability μ_r of the surrounding iron, Amperes law

$$\nabla \times \vec{H} = \vec{J}_{Eff} \tag{3.39}$$

needs to be solved (fig. [3.8]). The number of windings N=140 are incorporated into the effective external current as $\vec{J}_{Eff} = JN$ while $\mu_r(Steel) = 2000$. The relative field deviations further away from the middle of the dipole compared to the value in the middle are less than 10^{-4} (fig. [7.3]). This deviation is so small that it does not influence the transport significantly. Knowing this fact we decided to use a constant ideal magnetic field to simulate the transport of the electrons which decreases the calculation time.

The initial kinetic energy distribution (fig. [7.2]) is chosen as a Maxwellian distribution [Troe-93] with a maximum at 1.8 eV [Agr-70]. The creation of secondary electrons into other directions than normal to the surface of the foils is assumed to drop with

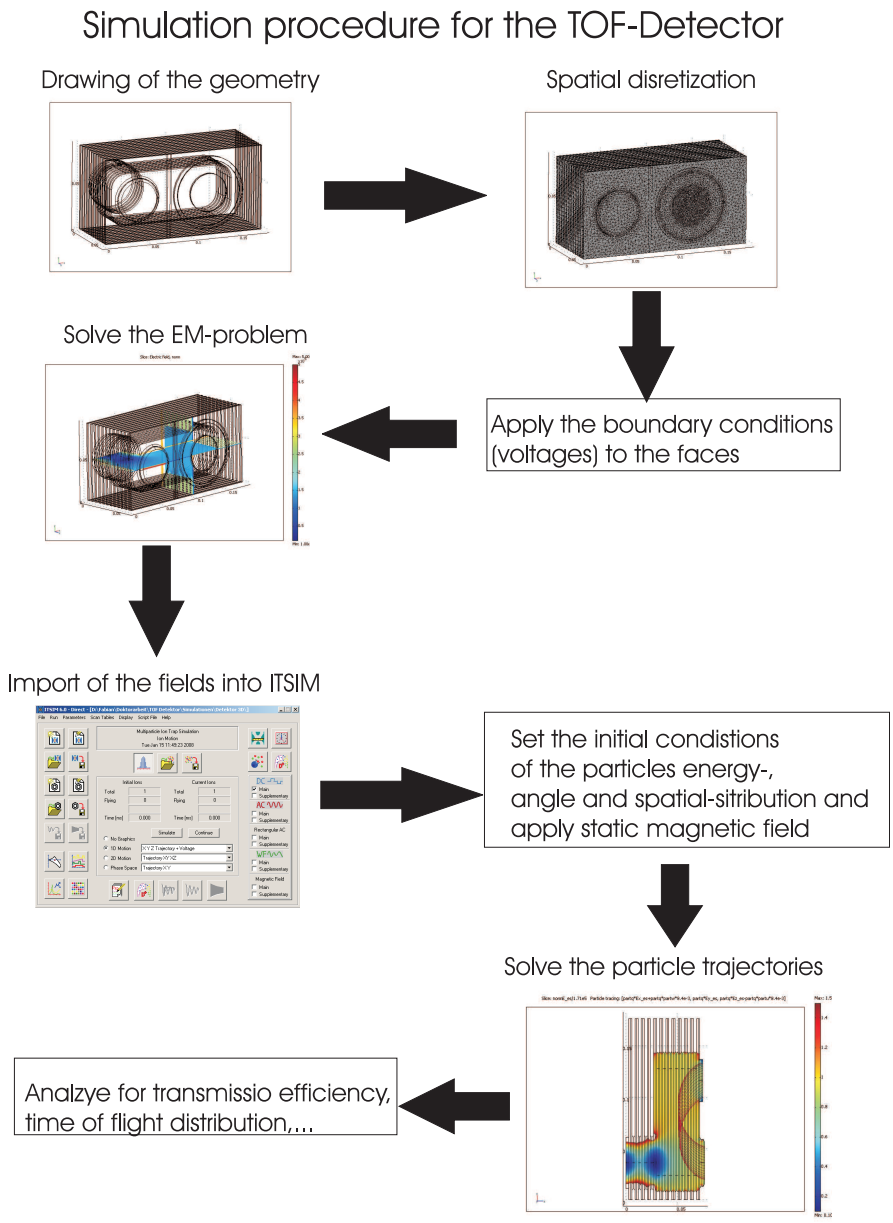

Figure 3.7: Procedure of the electron transport simulation in the detector by using different software. The program Comsol offers the capability of drawing the real 3D structure of the electrodes. The geometry is discretized by using an arbitrary grid. Potential can be applied to lines faces and volumes of the geometry. The next step is the calculation of the electrical potential on the nodes using a finite element method. The electrical field can be imported into the Ion trajectory simulation programm ITSIM. The initial conditions like spatial and energy distributions of the electrons can be chosen. Each electron trajectory is calculated by using a Runga-Kutta algorithm[But-87].

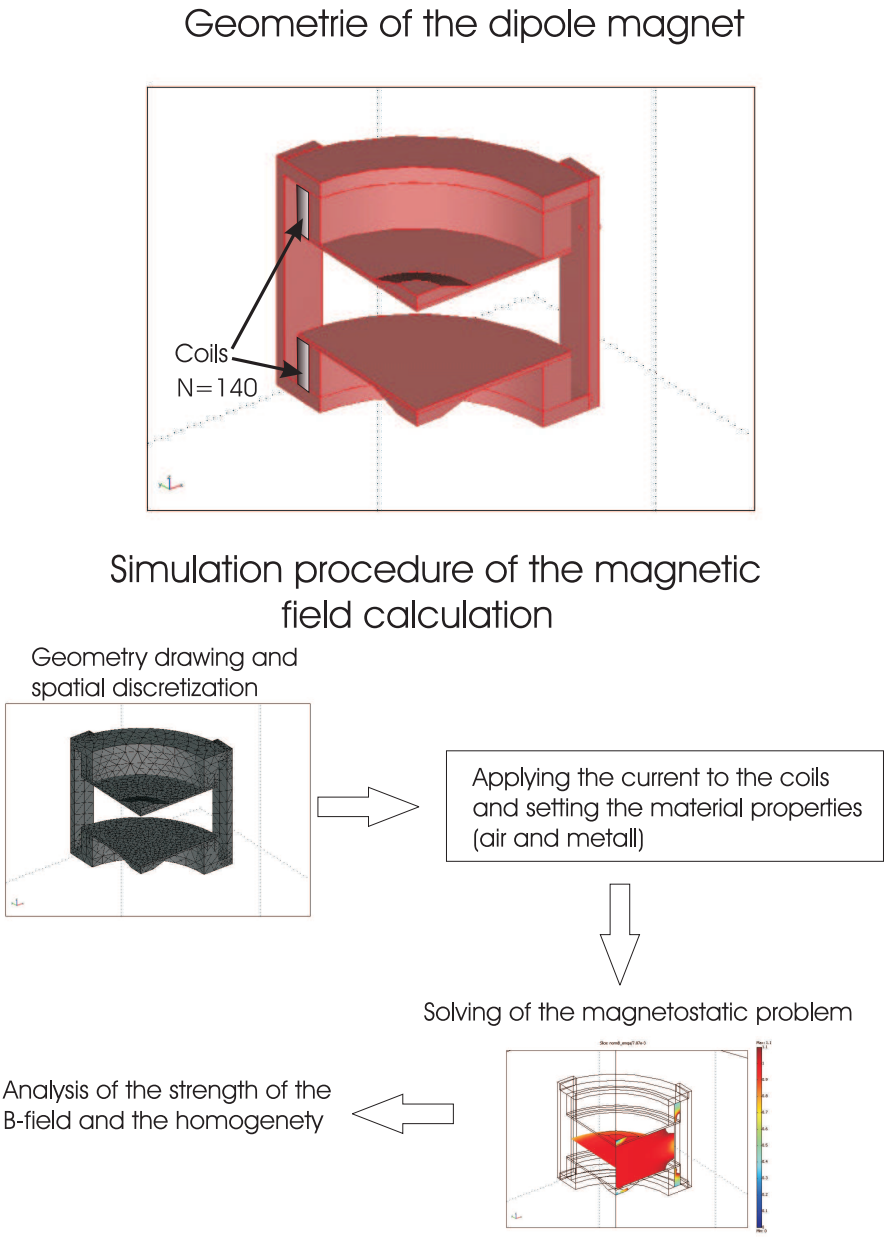

Figure 3.8: Process of magnetic field calculation using COMSOL. The geometry is drawn into the program COMSOL. Because of the symmetry of the geometric problem only one fourth of the geometry is solved. This yields a less time consuming calculation. The geometry is spatially discretized by a grid. The external current density is applied to the coils and the different volumes of air and steel are specified by setting the magnetic permeability μ_r. The problem is then solved by a finite element method [Com] and can be analyzed for interesting values using the implemented post processor.

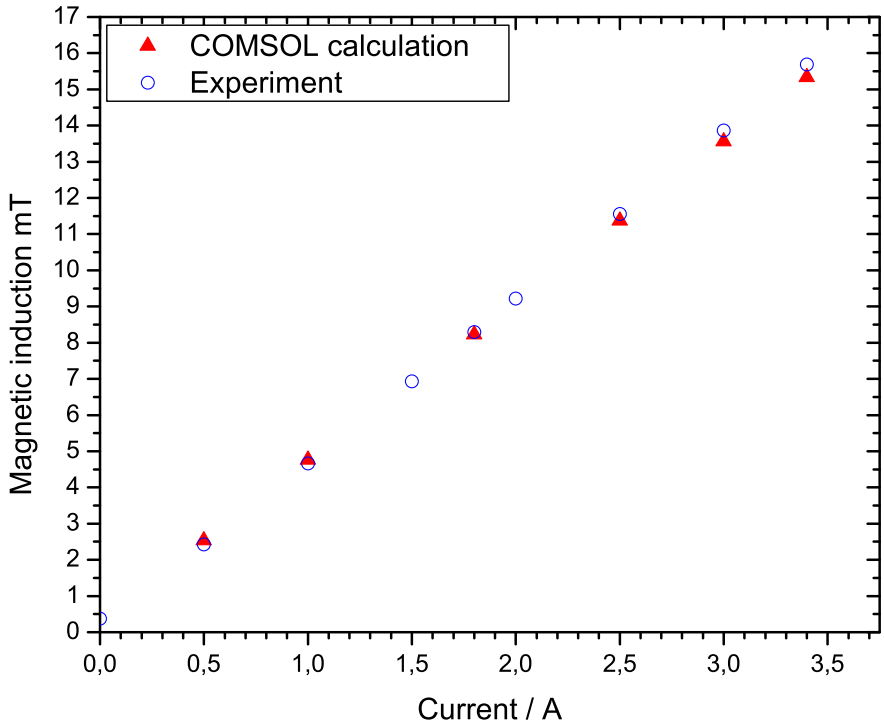

Figure 3.9: Comparison of the simulated magnetic induction using COMSOL in dependence of the applied current with the measured magnetic induction. Estimated experimental errors of the magnetic induction are about $\pm 1\%$

a cosine law [Troe-93] [Kos-74] [Dre-96]. This assumption includes that most of the particles pass through the foil orthogonally. A simulation with an isotropic emission angle distribution shows no significant influence on the transmission or timing results. So the detector itself is not sensitive to the variation of emission angles of the electrons. Different initial spatial distributions of the electrons are chosen. The distribution that describes the shape of the transmission curve the best is a Gaußian distribution with a sigma of 10 mm. The initial spatial distribution is therefore chosen to be a Gaußian-distribution in x and y-direction over the whole foil area with a $\sigma = 10$ mm. If not explicitly mentioned in the further studies this initial spatial distribution is used. It should also be mentioned that the magnetic field at which maximum transmission is reached does not shift by varying the initial spatial distribution.

Typical number of calculated trajectories are 10000 up to 100000. Typical calculation times ranged from 1 to 30 minutes. The calculation can be used to optimize the electron transport transmission from the foil to the detector while keeping the time-of-flight difference as small as possible.

3.3.4 Theory of Ion Induced Secondary Electrons

Ions passing through matter create electrons by inelastic collisions with the electrons of the solid. Electrons are created all along the passage of the ion through the solid. Some of them have energies high enough to overcome the potential barrier to the continuum and can be emitted by the solid. The so called "real secondary electrons" are electrons within an energy of $0 - 50$ eV [Dre-96]. A typical spectra includes also electrons with higher energies but the contribution of the real secondary electrons to the overall spectra is about 85% [Has-98]

3.3.4.1 Creation of Secondary Electrons

The secondary emission can be divided into two emission types. The potential electron emission [Has-98] which plays a role for slow imping ions and the kinetic electron emission [Has-98] that is dominant for higher impact energies. The potential electron emission starts if the potential energy of the projectile exceeds twice the workfunction ϕ of the target. The secondary electrons are created by resonance neutralization followed by auger deexcitation or by auger neutralization [Hag-54], [Hag-78].

The mechanism of the kinetic electron emission is considered as a three step model [Ster-57] and is applicable for higher impact velocities.

- Generation of excited electrons in the solid
- Diffusion of the electrons towards the surface
- Penetration of the electrons through the surface barrier.

The generation of secondary electrons by the kinetic emission type can be divided into the following processes:

- direct processes between projectile and target
  - by excitation of conduction or valence electrons into free states above the fermi level
  - by ionization of inner shells of the target atoms
  - by ionization in outer and inner shells of the projectile
  - electron loss of electrons from the projectile
- by secondary processes:
  - cascade multiplication of diffusing secondary electrons

- excitation of target electrons by energetic recoil atoms and by backscattered projectiles
- one-electron-decay of volume and the surface plasmon generated either by energetic primary ions or by secondary electrons
- by photons produced in projectile target collisions.

The main processes that contribute to the creation of secondary electrons are the excitation of electrons from the valence band into the continuum and shell ionization processes [Has-98]. An empirical way to describe the transport and the multiplication of the electrons is by describing it within a diffusion model [Ster-57], [Sch-80]. Electrons are created all along the path of the ion. The created electrons migrate through the solid and interact with other electrons untill they get lost by an inelastic process. Within the diffusion model it is assumed that the electrons have a diffusion length that is roughly given by the inelastic mean free path [Kos-89], [Jab-88]. Typical inelastic mean free paths of low energy electrons in metallic solids are in the order of $5-20$ [Sea-79] while for insulating materials the inelastic mean free path can be significantly higher [Has-98], [Ver-73], [Ohy-04], [Sei-67]. This is a fact caused by less free collisonal electrons inside the conduction band. The freed electrons have less collisional partners to interact in the conduction band that leads to significantly larger mean free paths. Caused by this effect more electrons are able to survive during their migration to and out of the solids surface. This effect causes an increase of the secondary electron yield.

After travelling to the surface the electrons still need to overcome the surface barrier of the solid. For metals the surface barrier is given by the sum of the Fermi-Energy E_F and the work function ϕ. The work function is a result of a non compensated potential energy because of the finite volume of the solid. Typical values for the work function of carbon are $\phi = 5$ eV [Dre-96] For insulators the barrier height is given by the electron affinity of the material [ICRU-99] [Has-98], [Sch-80]. The value of the electron affinity for CsI is given as 0.2 eV [She-02]. This difference in barriers already shows that by using an insulating target a higher secondary electron yield is expected.

3.3.4.2 Secondary Electron Yield per Ion

The total secondary electron yield per ion is given by the sum of the forward and the backward yield per ion. It has been shown by a wide test of experiments that the total secondary electron yield scales with the electronic energy loss of an ion imping on a target [Clou-89], [Roth-90], [Roth-92]. The constant Λ in equation 3.40 only depends on the target material and not on the projectile target combination or the velocity [Has-98]

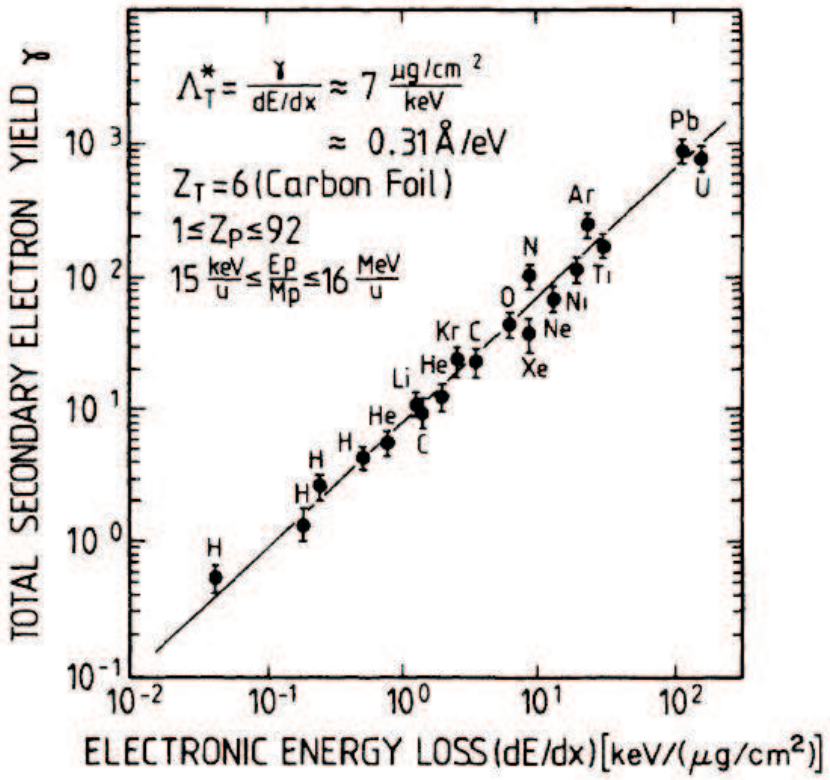

Figure 3.10: Total secondary electron yield of a carbon target in dependence of the stopping power. The secondary electron yield shows a quite good linearity with the electronic stopping power over a broad range of the stopping power and projectiles [Has-98].

and can be measured experimentally easily for each target.

$$n_{SE}^{T} = \Lambda \frac{dE}{dx} \tag{3.40}$$

The electronic energy loss is a good approximation for the sum of the main effects that contributes to the creation of electrons in the solid like excitation and ionization. To understand the target thickness dependence of the forward and backward electron yield Sternglass developed a model that is based on the three step model of the electron creation [Ster-57], [Kos-89]. The steps are the creation of electrons, the transport through the solid and the migration through the surface barrier. It assumes that the energy loss of the projectile is converted into the creation of two categories of electrons; slow and fast electrons.

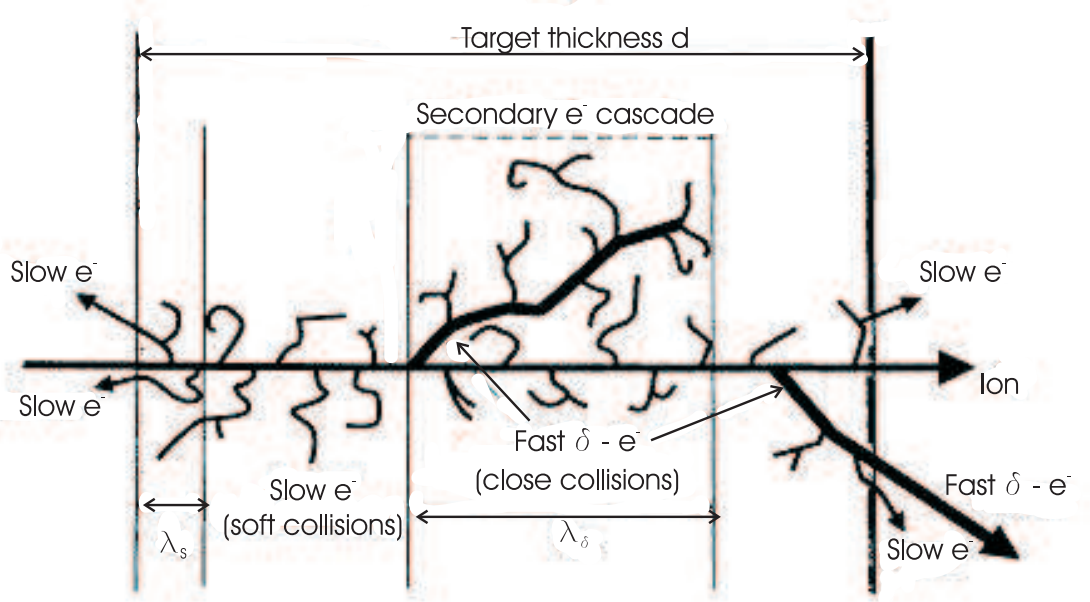

Figure 3.11: Creation of secondary electrons in a target. The main secondary electron cascade is induced by soft collisions of the projectile with the targets electrons. The so created slow electrons collide with other electrons in the target and so further develop a cascade that spatially develops up to target dependent thickness which is given by the inelastic mean free path of the slow electrons λ_S. Additional to this contributions secondary electrons can be created into the forward direction by a hard collisions process of the projectile with the target electrons. Therefore fast electrons (δ-electrons) are created that can also initiate an electron cascade further away from the point of creation. So the fast electrons are also able to develop an additional contribution of slow secondary electrons in the forward direction. Because of the higher electron energy the δ-electrons have a higher mean free path λ_δ and so the slow electron cascade develops further away of the point of creation and so a larger pathlength is necessary to let the cascade completely develop [Ster-57].

The slow electrons are produced in soft collisions with big impact parameter and the fast electrons, so called δ electrons, are created in collisions with small impact parameters (hard collisions). Only a fraction β_δ of the energy loss is converted into the creation of δ electrons. The total number of δ electrons generated in an unit layer dx with an average energy amount E_{SE} necessary to create them is given by

$$n_\delta = \frac{1}{E_{SE}} \frac{dE}{dx} \beta_\delta dx \tag{3.41}$$

While the soft collisions n_{Di} occur in forward and backward direction the hard collisions are assumed to contribute only to the forward direction.

$$n_{Di} = \frac{1}{E_{SE}} \frac{dE}{dx} (1 - \beta_\delta) dx \tag{3.42}$$

The electrons that are created by the soft collision at each position of the ions path travel through the solid with an inelastic mean free path of the slow electrons λ_{SE}. Because of the higher kinetic energy of the δ electrons they have a higher inelastic mean free path λ_δ as the slow electrons and so travel further away from their origin of creation compared to the slower ones. Because of increasing projectiles velocities the velocities of the δ-electrons also increases so the incorporation of the energy dependence of the diffusion length needs to be respected. This effect can be described by an empirically found formula [Jung-96]

$$\lambda_\delta = 390 (E_{Projectile}/M_{Projectile})^{1.22} \tag{3.43}$$

The energy transport of the δ electrons can be described by the diffusion function [Ster-57]

$$f(x, \lambda_\delta) = 1 - e^{-\frac{x}{\lambda_\delta}} \tag{3.44}$$

Sternglass assumes that during their migration the δ electrons are able to initiate an own additional cascade of slow electrons. So the creation of secondary electrons by δ electrons can be written in the form:

$$n_\delta = \frac{dE}{dx} \frac{\beta_\delta}{E_{SE}} (1 - e^{-\frac{x}{\lambda_\delta}}) \tag{3.45}$$

The diffusion of the created electrons and the surface transmission can be included in the probability function $D(x)$

$$D_B(x) = \tau e^{-\frac{x}{\lambda_S}} \tag{3.46}$$

$$D_F(x) = \tau e^{-\frac{(x-d)}{\lambda_S}} \tag{3.47}$$

while τ mainly includes the initial secondary electron angular distribution and the surface transmission probability. Assuming that these processes are independent from each

other [Ster-57], [Kos-89] the electron yield in forward and backward direction can be calculated

$$n_{SE}^{F,B} = \int (n_{Di} + n_{\delta}) D_{B,F}\, dx \tag{3.48}$$

Further assuming that the inelastic mean free path of the δ-electrons is much higher than for the slow electrons the expressions for the backward and forward yield are given by

$$n_{SE}^{B} = \Lambda^{*} \frac{dE}{dx} (1 - \beta_{\delta})(1 - e^{-x/\lambda_S}) \tag{3.49}$$

with

$$\Lambda^{*} = \frac{\tau \lambda_{SE}}{E_{SE}} \tag{3.50}$$

$$n_{SE}^{F} = \Lambda^{*} \frac{dE}{dx} \left(1 - \beta_{\delta} e^{-x/\lambda_{\delta}} - (1 - \beta_{\delta}) e^{-x/\lambda_S}\right) \tag{3.51}$$

Both yields saturate at a special distance from the foils entrance and exit. The position of saturation mainly depends on the secondary electron diffusion length λ_S. This effect can be understood easily in the way that electrons that are created too far away from any surface of the solid and not being able to migrate through the surface. They are simply absorbed by a collisional process and recaptured into a bound state. The total yield of backward and forward is given by the sum of the saturation values.

$$n_{SE}^{T} = \frac{dE}{dx} \Lambda^{*} (2 - \beta_{\delta}) = \frac{dE}{dx} \Lambda \tag{3.52}$$

It is also important to note that β_{δ} is about 0.2 for protons and Helium [Has-98] while for heavier ions β_{δ} increases up to an average value of 0.7 [Jung-96]. This difference is up to now only experimentally observed and can not be identified clearly. For high velocities of the projectile the inelastic mean-free-path of the fast δ-electrons gets so large that they are not able to initiate an own slow-electron cascade. Therefore the secondary electron cascade induced by fast electrons in the forward direction cascade can be simply neglected for energies of about 400 MeV/u and foil thickness thinner than hundreds of $\mu g/cm^2$. Therefore the equation 3.49 for the description of the backward yield is also valid for the description of the forward yield.

3.3.4.3 Secondary Electron Spectra

The spectra of the secondary electrons includes different interesting features (fig. [3.12])

- True secondary electrons
- Plasmon excitation
- Auger electrons

- Convoy electrons
- Binary encounter electrons

The true secondary electron peak is created by the already explained cascade process.

The plasmon excitation followed by a release of an electron is a process in which a volume or surface plasmon is excited within the solid and by deexciting the energy is transferred to an electron that is emitted by the solid [Has-98]. This feature is superimposed the true secondary spectra and mostly seen as a shoulder.

If the ion creates a hole in a deep lying shell of the target atom the target can deexcite by transferring its energy to an outer electron that is emitted. This process has a very specific energy and is named Auger-process [Luc-72] [Schnei-75]. The energy of the Auger-electrons is very specific and a fingerprint of the atom that ejects it.

The so called convoy electrons are electrons that have the same velocity like the projectile [Det-74]. The main process of creation is the electron capture to continuum (ECC) and the electron loss to low-lying continuum states (ELC) [Has-98].

An electron that has a violent collision with the projectile and all the momentum from the projectile gets transferred to the electron is called a binary encounter collision. This is the maximum of momentum the target electron can gather from the collision and is so somehow a cutoff of the spectra. The speed an electron can gather from this binary encounter collision is twice the speed of the ion.

It is also important to note that the true secondary electron spectra shape does not depend on the projectile energy, mass or charge. But for different targets the shape can differ [Has-98], [Joy-04].

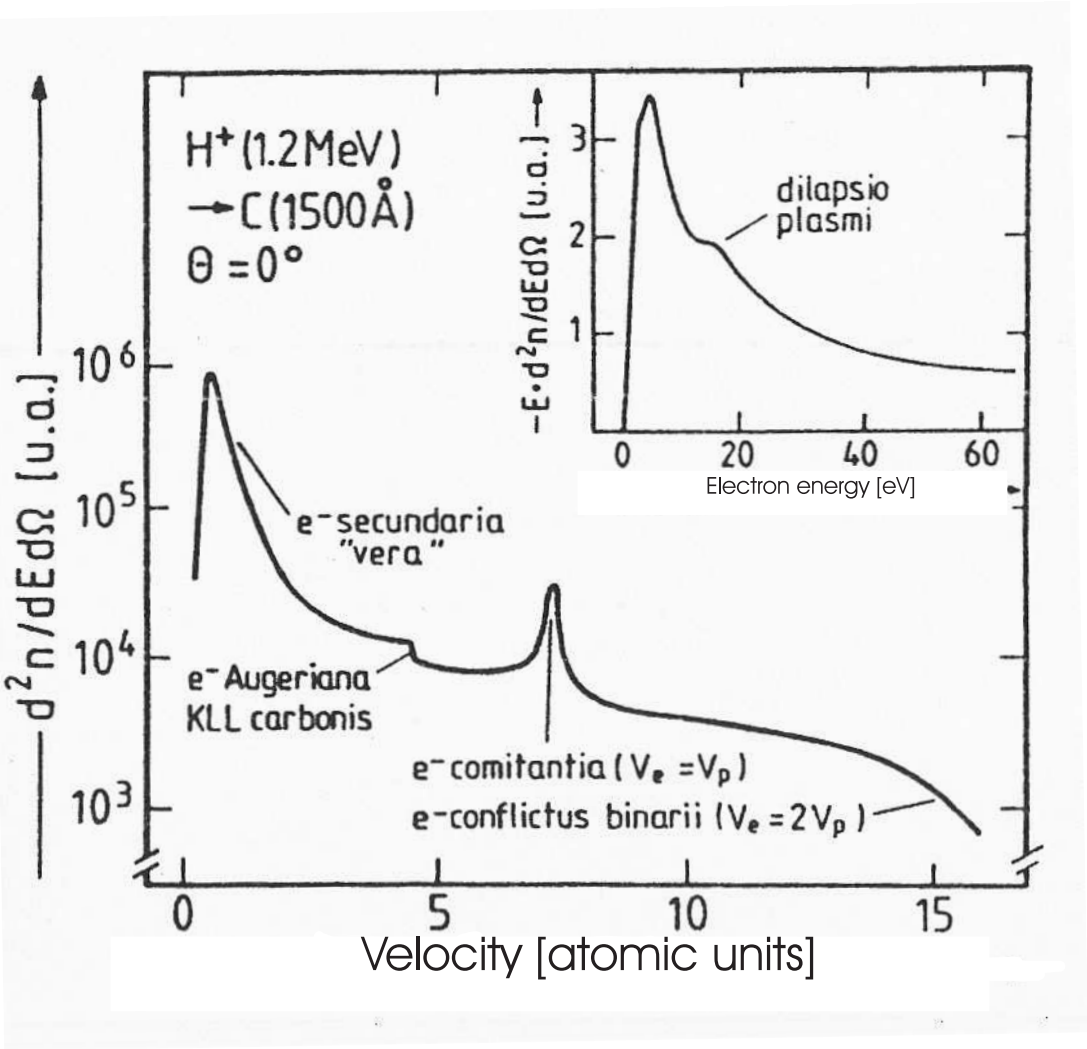

Figure 3.12: Typical secondary electron spectra of a carbon target of thickness 1500 an under an emission angle of 0° compared to the penetrating protons with an energy of 1.2 MeV/u. Different features can be observed in the spectra. The real secondary electron peak (e^- secundaria vera) caused by the cascade effect. The plasmon shoulder (dilapsio plasmi) that raises because of solid state effects in this energy region and causes electron ejection from the target. Further smaller features are Auger-electrons (e^- Augeriana KLL carbonis) from the ionization of inner shell electrons of the target and the convoy electrons (e^- comitantia) that are electrons which move with the same speed of the projectile. The spectra typically shows a bump at energies of about twice the velocity of the projectile which is caused by the so called binary encounter process (e^- conflictus binarii) that describes the total momentum transfer of the projectile to the target electron [Has-98].

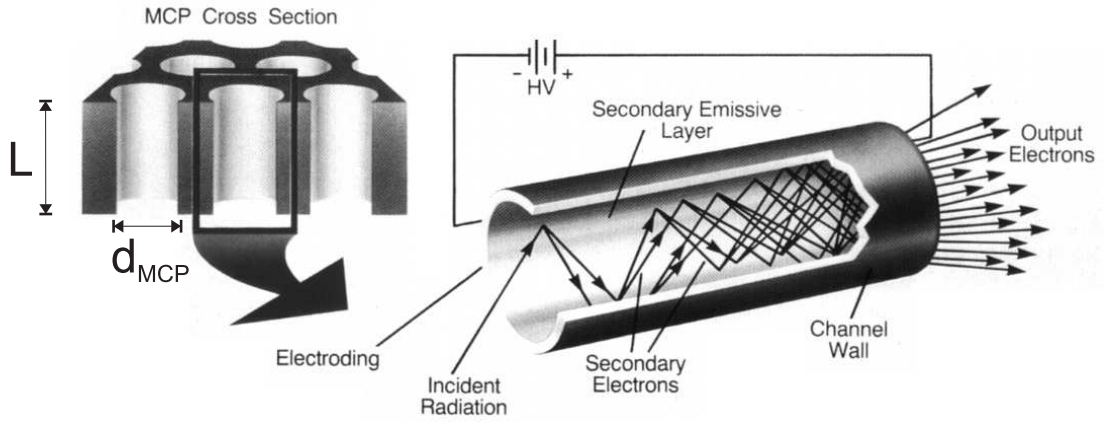

Figure 3.13: Sketch of a micro channel plate and gain operation mode of one micro channel. The MCP consists of about 10^6 - 10^8 micro channel. A micro channel is typically characterized by the length L of the channel and the diameter d_{MCP} of one channel. The ratio of these parameters is specific for the gain of the channel [Wiz-79]. A voltage of about 1000V is applied across the entrance and exit of the channel. Ionizing particles release secondary electrons while hitting onto the channels wall. The electrons are reflected by the walls and further gained untill they leave the channel. The outgoing current can be detected with a metal anode.

3.3.5 Micro channel Plate

A micro channel plate consists of about $10^6 - 10^8$ mostly independent parallel micro channels (fig. [3.13]). Each micro channel works like a electron multiplier with a typical gain of about 10^4. A typical voltage of $1000V$ is applied over the length of a channel. The multiplication cascade inside the channel is induced by the imping particles. The projectile releases secondary electrons at the channels wall which are further accelerated by the bias voltage. These created electrons hit onto the channel wall and further create electrons. The gain is dependent on the coating material of the channels that determines the secondary electron yield α and the length to diameter ratio L/d_{MCP}.

$$g \sim e^{\alpha L/d_{MCP}} \tag{3.53}$$

Typical full-widths at half-maximum of the MCP signals are about 1 to 3 ns and electron transit times in the channel are in the order of hundreds of pico seconds. A common approach to increase the gain and having less dark counts the usage of two micro channel plates in a so called chevron setup is proposed. Typically the angels of the channels are inclined against the normal of the channel plates surface. The reasons therefore are that the detection efficiency of ion depends on the imping angle of a particle and to suppress ion feedback [Wiz-79].

The MCPs are typically installed consecutively with a distance of about some μm up to

mm. The advantage of using two MCPs is a gain of 10^7 to 10^8 that can be reached. Another advantage is that because of charge saturation effects in the second micro channel plate the so called pulse height distribution gets peaked. The pulse height distribution is an abundance histogram of the signal amplitudes. This histogram makes it possible to define a useable threshold for further analysis of the signals. Using just one micro channel plate the gain is too small to produce measurable amplitudes and the pulse height distribution is exponentially. So the highest abundance of amplitudes is at small values that makes it hard to adjust a reasonable trigger for defining noise and signal.

The detection efficiency of channel plates is quite different for different energies and particles. For electrons in the range of 300 V to 1000V the detection efficiency saturates [Bou-79] around a value that is equal to the open area ratio (OAR) of the micro channel plate and is in the order of 60%. Using a grid in front of the detector the incoming particles that are reflected by the channel plate because of not hitting a channel can be driven back onto the detector. This feature allows to increase the detection efficiency up to a value of about 80% for electrons [Wiz-79], [Torn-90].

A disadvantage of these micro channel plates is the finite recharge time of the individual channels which is in the order of 20 ms for standard MCPs. The charge that is extracted from the channel needs to be refilled by the power supply but this time is simply limited by the micro channel itself. A single micro channel channelcan be described as a capacitor with a resistance of 10^{14} Ω and a typical capacity of 10^{-16} F [Wiz-79]. So the recharge time for one channel can be estimated by $\tau = RC$ an is in the order of 1 to 10 ms. There also exists so called Extended Dynamic Range (EDR) micro channel plates which are MCPs with a resistance of 10 MΩ instead of 100 MΩ. This decreases the recharge time by a factor of ten and so their rate resistance is better within a factor of 10.

3.3.5.1 Spatial Spread of the Electron Cloud

To estimate the number of excited channels in the second MCP by one channel in the first MCP in dependence of the gap voltage and the gap distance the following model can be used [Rog-82] (fig. [3.14]). The model is based on a classical acceleration description of the electrons in a constant electric field. Because of the small number of about 10^4 electrons after the first MCP no space charge effects are expected to contribute at this stage of the MCP-detector and will be therefore not considered [Rog-82].

The electrons that are released by a single channel in the first MCP have a tangential E_T and normal energy E_N component of about $E_N = 50$ eV and $E_T = 0.2$ eV [Mar-80] compared to the MCPs surface. The voltage U_G across the gap with size d_G accelerates the electrons and also focus or defocus the electrons onto the second channel plate. The transit time t of the electron can be calculated by

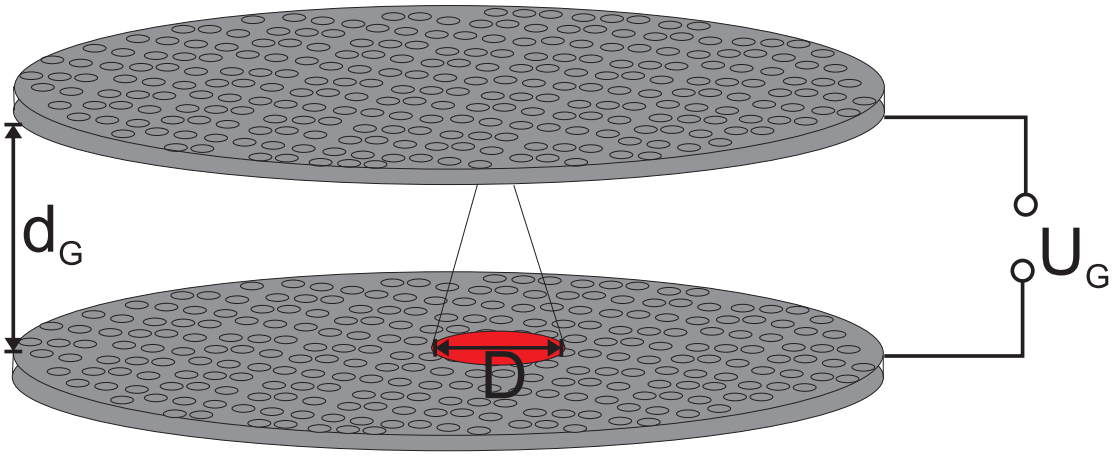

Figure 3.14: Spatial spread of the electron cloud between two MCPs. Electrons are released by a channel and spread into the transversal direction because of a transversal component of their exit velocity at the exit. Assuming that the electric field between both MCP surfaces is homogenous an analytical description for the influence of the spacing and the applied electric field between the MCPs onto the spatial spread of the electron cloud can be derived [Rog-82].

$$t = \frac{v}{a} \tag{3.54}$$

with v the velocity and a the acceleration. In a good approximation the electrical field E can be assumed to be homogenous. So the acceleration a of the electron can be written as

$$a = \frac{qE}{m_e} = \frac{eU_G}{m_e d_G} \tag{3.55}$$

while the initial velocity v_N of the electrons normal to the surface can be written as

$$v_N = \sqrt{\frac{2e}{m_e} E_N} \tag{3.56}$$

So the transit time is given by

$$t = \sqrt{\frac{2m_e}{e}} \left[\sqrt{E_N + U_G} - \sqrt{U_N} \right] \frac{L}{U_G} \tag{3.57}$$

In this time the cloud spreads into the radial direction and reach the radius

$$r = \sqrt{\frac{2eE_T}{m_e}} t \tag{3.58}$$

So the total width of the cloud is assumed to be the sum of twice the radial spread and the initial width that roughly corresponds to the channel diameter. The electron cloud

width D is therefore given by

$$D = d_C + 4\left[\sqrt{E_N + U_G} - \sqrt{U_N}\right]\frac{L}{U_G}\sqrt{E_T} \tag{3.59}$$

So the number of exited channels in the second MCP per channel in the first MCP is given by

$$N_{Exc} = \frac{\left(d_C + 4[\sqrt{E_N + U_G} - \sqrt{U_N}]\frac{L}{U_G}\sqrt{E_T}\right)^2}{d_{MCP}^2} \tag{3.60}$$

with d_{MCP} being the channel diameter of the MCP.

3.3.5.2 Detection Efficiency for Secondary Electrons

To get a relation between the average number of created secondary electrons and the detection efficiency of a micro channel plate a model described in [Brun-97] can be used. A good approximation of the number distribution of secondary electrons created in a collisional process with an average secondary electron number $\overline{n}_{SE}$ is the Poisson distribution [Has-98]. The probability distribution is given by

$$\rho = \frac{\overline{n}_{SE}^n}{n!}e^{-\overline{n}_{SE}} \tag{3.61}$$

while n is the number of electrons emitted. Assuming that only a detection is possible if at least one electron is created the following probability is given

$$\rho = 1 - e^{-\overline{n}_{SE}} \tag{3.62}$$

The finite detection efficiency ε_{MCP} caused by the finite channel area (OAR) of the MCP still needs to be considered in eq. 3.62 The electrons are only detected if at least one electron is created and hits into an active area of the MCP. So the detection efficiency can be written as.

$$\varepsilon_{MCP}(\overline{n}_{SE}) = 1 - e^{-\overline{n}_{SE}\varepsilon_{MCP}} = 1 - e^{-\overline{n}_{SE}OAR} \tag{3.63}$$

The detection efficiency starts to reach 100% at an average number of six electrons (fig. [3.15]).

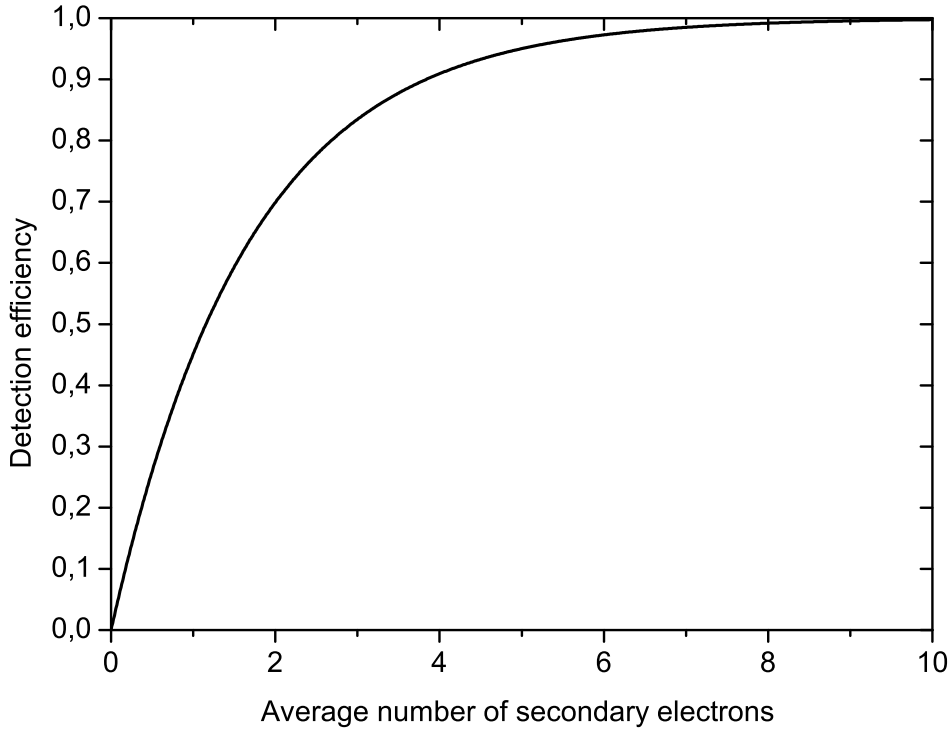

Figure 3.15: Detection efficiency in dependence of the average secondary electron number. Up to value of about 6 electrons the detection efficiency increases to 100%. Further increase in the secondary electron number does not yield a higher detection efficiency.

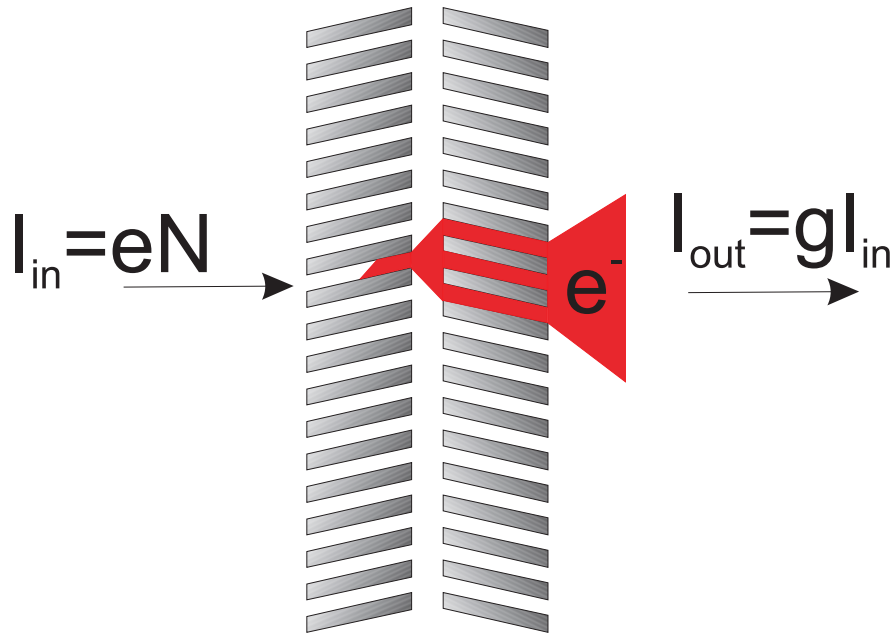

Figure 3.16: Explanation of the gain procedure of a MCP. An incoming particle current is amplified by the first MCP and then further by the second MCP. The gain als depends on the number of exited channels because more channels yield a higher gain. A second fact is that the voltage between the MCPs also defines the average kinetic energy an electron hits the second MCP. The total yield of secondary electrons also depends on the energy of the imping particle and so the gain is tuned by this value, too.

3.3.5.3 Saturation Effects in Micro Channel Plates

There are two points to consider in the dead time effect of micro channel plates. The first parameter that limits the detection of particles at higher rates is the strip current I_S of the MCP and the second the finite number of channels. The strip current of the MCP is the current flowing through the MCP supplied by the power supply. This current supplies the excited channels with the charge necessary to recharge. So, if the output current of the MCP reaches the order of the strip current not all channels can be recharged effectively. This effect results in a decrease of gain because of having less channels completely recharged [Shi-99]. So, the amplitudes of the signal drop and eventually so that that the voltage signal vanishes in the noise. The geometrical effect caused by the finite number of channels is mostly important if the measurement time is significantly shorter than the recharge time. Channels that are excited are not able to recharge sufficiently in the time the next projectile will hit. So the channels get somehow paralyzed and cumulatevly not respond anymore to incoming particles. It is important to consider that one channel in the first MCP excites $10-100$ channels in the

second MCP so that the effective rate the MCP could take is less than the number of channels in the first MCP. Therefore an effective channel number N_{Eff} which depends on the gap size d_G and the voltage across U_G the gap needs to be taken into account. Therefore eq. 3.60 can be used.

To describe the gain and amplitude of a micro channel plate detector in dependence of a constant incident particle rate the incoming current is given by

$$I_{in} = qf \tag{3.64}$$

with q being the charge and f the rate of the incoming particles. The micro channel plate multiplies the incoming current with the gain g (fig. [3.16]) which can be calculated by

$$g = \frac{I_{out}}{I_{in}} \tag{3.65}$$

Assuming that the time intervals between successive events are poisson distributed and taking into account that each channel recharges like an ideal capacitor with a typical recharge time τ dependent just on the resistance and capacitance of the MCP [Sha-89], the gain is given by

$$g = \frac{g_0}{1+f\tau} \tag{3.66}$$

Equation 3.66 shows that the gain decreases at a specific rate because the channels can not be recharged in time anymore. The dependence of the output current I_{out} is then given by

$$I_{Out} = gI_{in} = \frac{g_0 qf}{1+f\tau} \tag{3.67}$$

The measured rate f_{exp} in dependence of the real incident rate f has the same behavior like the output current and can be written as

$$f_{exp} = \frac{f}{1+f\tau} \tag{3.68}$$

To describe the behavior of a micro channel plate detector over a period of time a more detailed description is necessary. A very detailed description of the derivation of the equations can be found in [Giu-93]. In the further discussion only the basic assumptions and the key features are presented.

The time dependence of the gain of a MCP can be described by model [Giu-93] that is based on a dynode model of Eberhardt [Eb-79] [Eb-81]. This model is a more conceptional model that describes the MCP like a discrete dynode multiplier (fig. [3.17]). The voltage between two dynodes is given by $V_D = V_{MCP}/N$ where N is the dynode number. After amplifying the signal at a dynode the voltage drops at the dynode about the value V. So charge is extracted from the dynode but will be restored by the power supply.

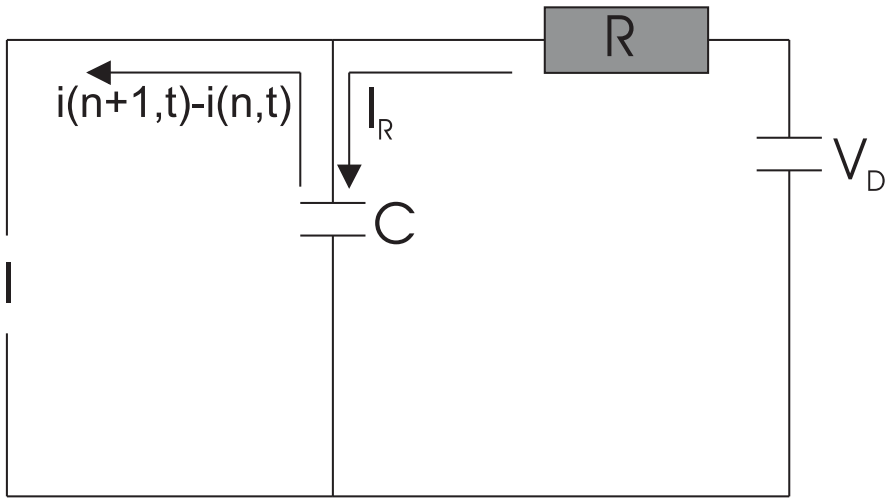

Figure 3.17: The circuit diagram of the recharge process of micro channel. An incoming current causes a voltage drop V_D over the capacity C which causes an outgoing current $i(n+1,t)$ that be transferred to the next dynode. The power supply recharges the lost charge over the resistance R with the current i_R. The incoming current also partially recharges the system with the current i(n,t).

The relative change of the current at the $(n+1)^{th}$ dynode compared to the n^{th} can be written as

$$\frac{i(n+1,t)}{i(n,t)} = \left(\frac{V_D - V}{V_C}\right)^k \tag{3.69}$$

in which V_C and k are constants that describe the secondary emission.

The voltage drop on a dynode can be described by a simple model that is based on the idea of recharging current processes. The voltage on a dynode with capacity C drops about a value V_D that causes an outgoing current. The missing charge is then recharged by the power supply over the resistance R with the current i_R. The incoming current on the n^{th} dynode also recharges the dynode with the incoming current $i(n,t)$ while the charge that is removed from the dynode carries away the current $i(n+1,t)$. This effects nett leads to a voltage drop about the value V_D on the dynode capacity C.

$$C\frac{\partial}{\partial t}\left[V_D - V(n,t)\right] = i_R(n,t) - i(n+1,t) + i(n,t) \tag{3.70}$$

Combining both equations 3.69 and 3.70 and solving it for the gain, an approximation to the differential equation can be made and a quantitative relation of the gain in dependence of an incoming pulse of intensity I_0 with length can be derived analytically.

$$g(t) = g_0 \frac{\left(1 + se^{-t(1+s)/RC}\right)}{1+s} \tag{3.71}$$

s is the so called saturation parameter that includes secondary emission constants, the recharge time and more important the Intensity I_0. So s is directly proportional to the incident rate. Equation 3.71 already shows important features of the MCP at different rates. The gain decays in first order exponentially with the time and gets into a quasi static equilibrium after a specific time. At this time the recharging and excitation process is in equilibrium. The higher the incoming rate the smaller the quasi static gain gets. So the amplitudes decrease to smaller values for higher rates.

An also quite known feature of MCPs at high rates is the disturbance of the pulse height distribution. The pulse height distribution is an abundance histogram of the measured pulse amplitudes. In a typical used mode the pulse height distribution has a peaked structure at a specific amplitude. This makes it easy to set a threshold that is used to decide between real signals and artificial signals like noise. Typically the area under the pulse height distribution is a measure of the detection efficiency. A known feature at higher rates is that with decreasing the gain the pulse height distribution shifts to smaller amplitudes and changes their shape [Giu-93], [Fras-92], [Fras-91]. This causes more and more amplitudes to drop under the threshold and so the area under the pulse height distribution drops which yields a drop of the detection efficiency.

4 Offline Experiments

To verify simulation and optimize the time-of-flight detector and the micro channel plate detector offline experiments were performed.

A time-of-flight detector identical to the one operating at the ESR was built in Gießen to make it possible to test the detector and make modification to it without applying for an expensive beam time. The projectiles used to penetrate the detector foil in the experimental setup are α-particles with an emission energy of 5.48 MeV/u. Offline tests concerning the optimization of the electron transport from the foil to the MCP are performed. Therefore the electric and magnetic field is varied. The influence of the foil thickness and coating on the ion detection efficiency is determined experimentally and compared combining predictions for the secondary electron yield and the detection efficiency of the MCP.

A special setup is built for testing the rate capability of the micro channel plate detector. Therefore an electron beam with specific electron current is shot onto the detector. The source is used in a DC-mode and a pulsed mode that allows to shoot short bunches of electrons onto the MCP for some hundreds of microseconds. In both modes the electron current is further increased until a break of the count rate is observed. For every electron current different parameters like gain, outgoing current at the anode, pulse-height distribution and count rate are registered. Different measurements are performed while varying the distance and voltage between the MCPs.

4.1 Transmission Efficiency

Simulations of the electron transport from the foil to the MCP show that the transport used previously is not ideal and a significant increase of the transmission efficiency could be achieved easily. Therefore it is necessary to compare the behavior of simulated transmission in dependence of the electrode potentials and the magnetic field with experimental data.

The total detection efficiency ε_{Tot} of the detector is given as the product of the transmission probability ε_{Tr} and the detection efficiency ε_D

$$\varepsilon_{Tot} = \varepsilon_{Tr}\varepsilon_D \tag{4.1}$$

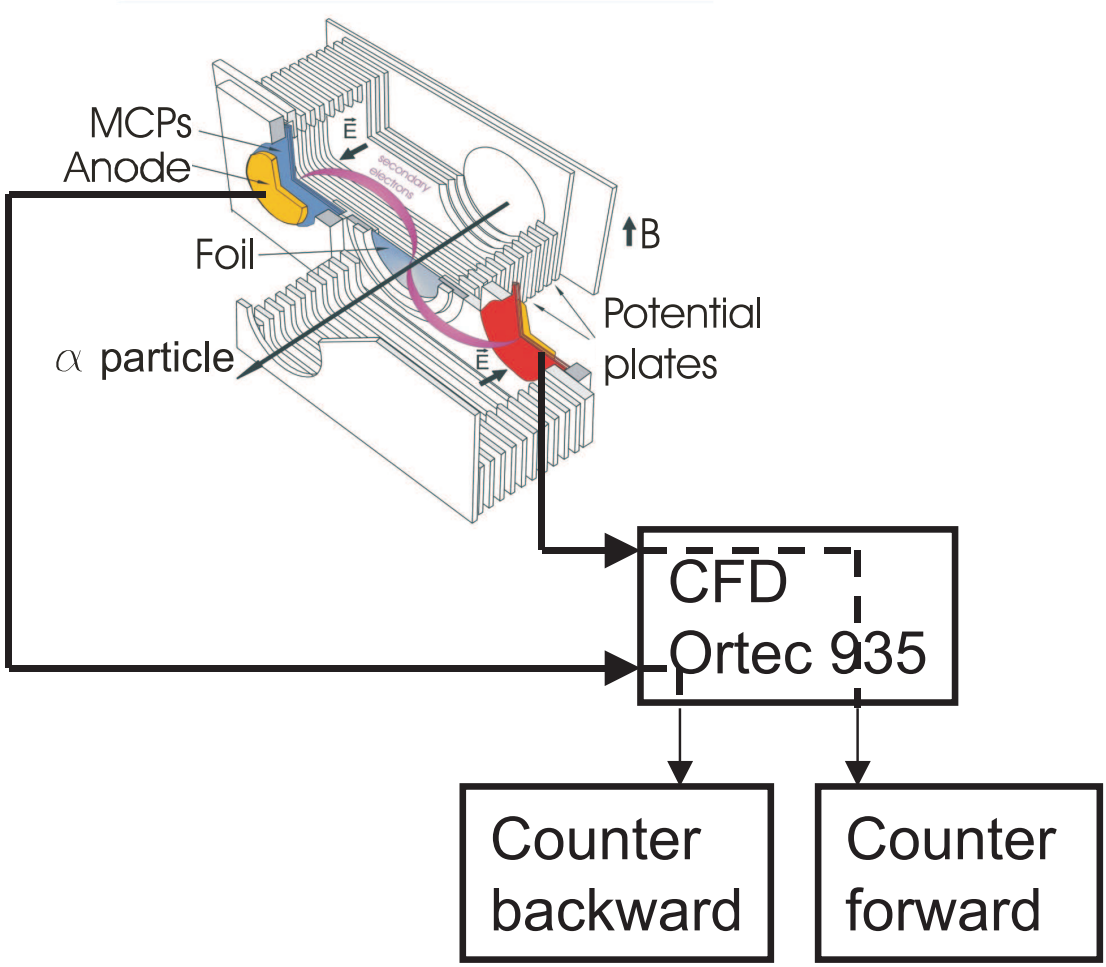

Figure 4.1: Setup used for measuring the transmission probability of the secondary electrons from the foil to the MCP. The foil is fully illuminated by the α-particles. So the flux of the projectiles stays constant while variation of the electrode potentials and the magnetic field yield a change in flux of electrons onto the MCP. The count rate is measured by converting the MCP signal into a standard NIM signal using the CFD that can be used by a NIM counter. For every different detector setting the number of signals per time are counted.

Detector setting	U^{++}	U^{-}	U_{MCP}	U_{Foil}	I_{Magnet}
Previous	$5200V$	$-2000V$	$-2700V$	$-3400V$	$1.7A = 7.9mT$
New	$5000V$	$-2700V$	$-2700V$	$-3400V$	$1.8A = 8.4mT$

Table 4.1: Overview of electrode potentials and the magnetic flux of the old and optimized new detector setting.

An ion hitting the foil produces the secondary electrons locally very focused around the passage of the ions path. So the origin of multiple electrons is in first order the same for a specific ion. Monte Carlo simulations show that electrons with different initial kinetic energies but the same starting position finally have a spatial spread smaller than 1mm on the MCP.

The used α emitter is a ^{241}Am source. The kinetic energy of the alpha particles is 5.486 MeV. The effective energy of the projectiles are slightly decreased by a 2 μm thick steady steel foil that is wrapped around the source that causes the kinetic energy to drop to 4.58 MeV.

The ion detection efficiency of the MCP detector is constant over the total area (fig. [4.7]) because it just depends on the open area ratio (OAR) and the average number of secondary electrons $\bar{n}_{SE}$ imping on the micro channel plate detector. This shows that the total detection efficiency is simply proportional to the transmission probability. To measure the relative change of the transmission probability the count rate on the MCP detectors are used. The relative change is measured by using counters that count the incoming electron bunches on the MCP that correspond to an ion. The MCP signals are prepared by a constant fraction discriminator (CFD) before leading them to counters to make sure that the dynamic range of the voltage is decreased. Typical signal heights of the MCP are in the range of 200 mV for an applied operation voltage of 1000 V per MCP. The lowest adjustable CFD threshold of the used ORTEC 945 is about 40 mV. No amplifiers are used because they significantly broadened the signal and produced strong noise effects.

To make a comparison between simulation and experiment the MCP count rate for the previous setting is normalized to the calculated transmission probability. For all other settings the count rates simply scale. Experimental data is taken for two different electrode voltages while varying the magnetic field. The error of the count rate measurement is estimated by the maximum error of single measurements compared to an average value and yields about 2%. The first electrode setting is a setting that was used for many years because it has experimentally shown best timing properties [Rad-94]. The second setting is found by an optimization of the transmission probability while keeping the time-of-flight width as small as possible using the simulations. The comparison shows that the improved transmission probability expected from the calculation can also be observed experimentally (fig. [4.3]). With the simulations is is

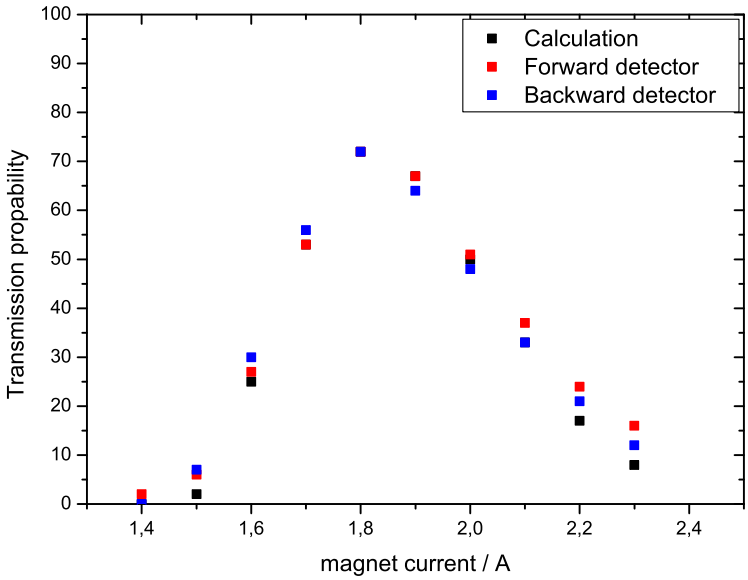

Figure 4.2: Comparison of the experimentally measured electron transmission probability with simulated values for the old timing optimized electrode potentials. Typical estimated experimental uncertainties are ± 2 %.

possible to make useable predictions of the transmission probability for future developments. Therefore the transmission efficiency can be increased by almost a factor 2 in simulation and experiment (fig. [4.3]).

Simulations also show that the influence of varying the initial kinetic energies of the secondary electrons have no significant influence on the transmission probability. The biggest uncertainty in this calculation seems to be the unknown initial spatial beam distribution of the α particles. But the knowledge of the exact initial distribution is not very critical because the optimum point of transmission and timing only change their absolute values while the relative optimum always stays the same. Only moving the centroid of the initial spatial distribution significantly changes the transmission characteristic. So, if the detector is optimized for a reasonable initial spatial distribution the relative optimum is found. The optimum of transmission calculated is also tested for the case of homogeneous illumination of the foils area. Therefore the found magnetic field and voltages also yield the highest transmission efficiency.

The absolute increase of the transmission efficiency can be explained by considering two main effects. The increase in magnetic field results in an increase of electrons imping on the MCP-detector. The higher magnetic field allows electrons that have a smaller

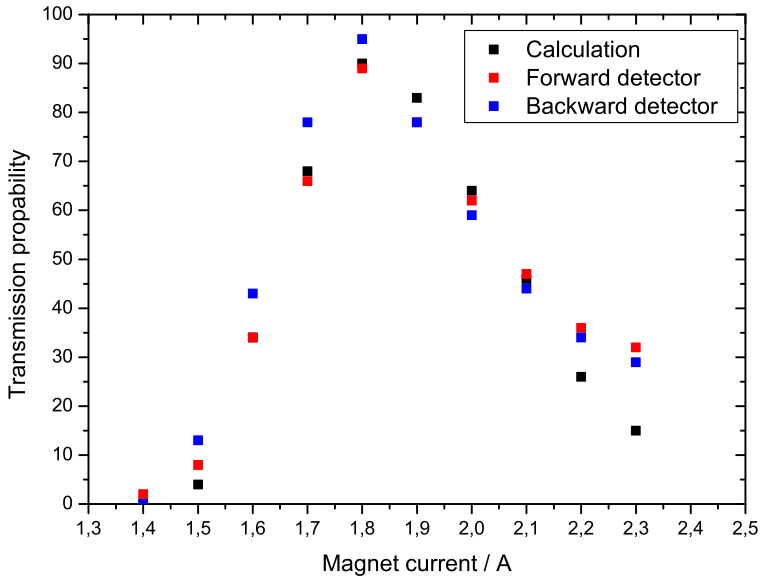

Figure 4.3: Comparison of the experimentally measured electron transmission probability with simulated values for the new timing optimized electrode potentials. Typical estimated experimental uncertainties are ± 2 %.

distance to the MCP-detector still to be bent onto the active detection area of the MCP. Furthermore the centroid of the final position distribution of the electrons match with the position of the middle of the MCP-detector. The second important parameter is the influence of the voltage U^-. This is the voltage that is applied to the voltage divider and also to the middle plain of the detector system. Changing this value to a more negative value the electron beam can be focused onto the channel plate detector. The comparison of the figures [4.3, 4.2] shows clearly the difference of the old and optimized setting. So, using the new optimized setting not only the transmission efficiency is increased but also the usage of the foils area. Calculations using a homogeneous spatial distribution of starting electrons yield a useable foil area of 38% (fig. [4.4]) for the previous setting and 83% for the new setting (fig. [4.5]). Therefore a much higher coincidence rate can be reached which could help in the detection of ion created signals in online experiments.

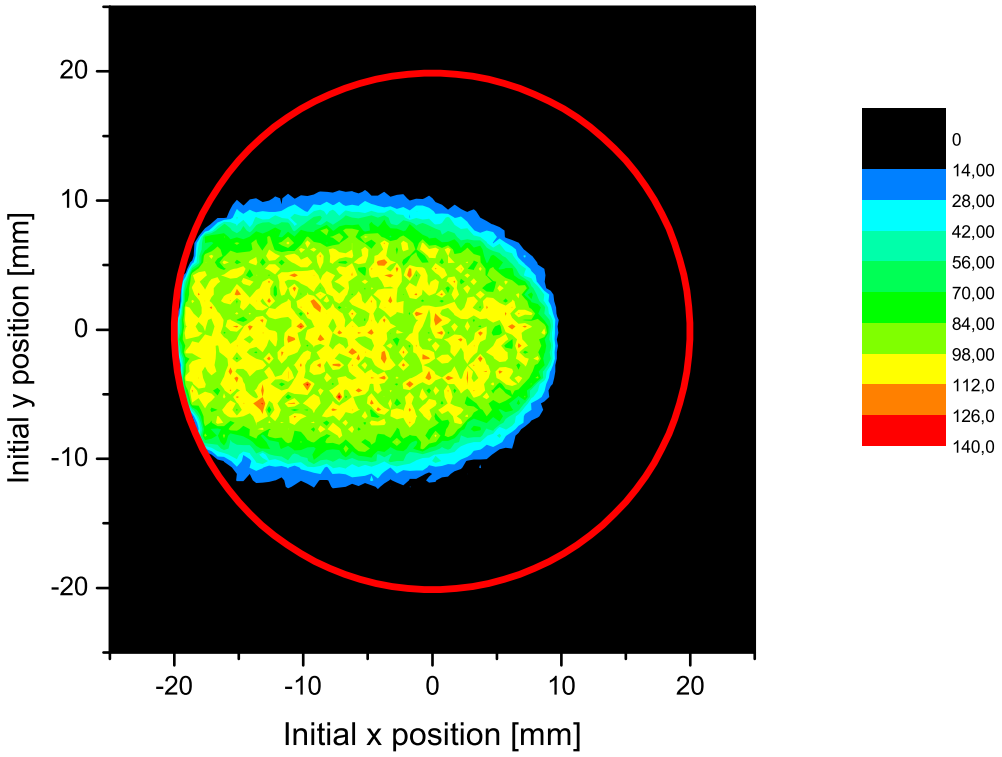

Figure 4.4: Visualization of the useable active foil area calculated with a Monte Carlo simulation for the previous detector setting and an initial homogeneous spatial distribution of the electrons on the foil. The red circle indicates the foil while the black area shows inactive positions on the foil. If an electron is created in the black area it will not be able to be transported to the MCP.

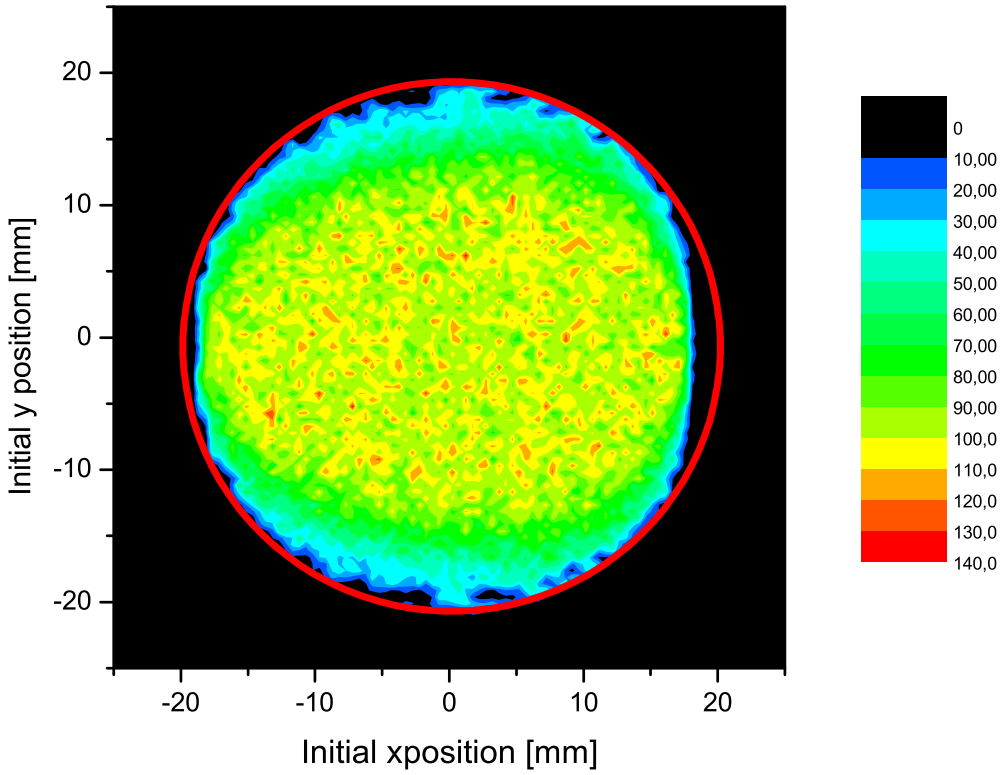

Figure 4.5: Visualization of the useable active foil area calculated with a Monte Carlo simulation for the new detector setting and an initial homogeneous spatial distribution of the electrons on the foil. The red circle indicates the foil while the black area shows inactive initial positions on the foil. If an electron is created in the black area it will not be able to be transported to the MCP.

4.2 Detection Efficiency

Another important process directly after the transport of the electrons to the MCP is the detection of them. Therefore it is important which fraction of the incoming particles is detected and therefore the detection efficiency. The conversion process from the passage of the ion through the foil, the release of an average number of electrons and the detection of them on the micro channel can be summarized by measuring the ion detection efficiency. In chapter 3.3.4.2 it is explained that the average number of emitted electrons depends on the stopping power of the ions while the detection efficiency of secondary electrons just depends on the open area ratio and the average number of secondary electrons. Measurement of the ion detection efficiency can be used to validate the combined model of number of secondary electron theory and detection efficiency of a MCP for application with the TOF-detector. To measure the detection efficiency a Si-surface-barrier-detector is installed behind the foil to detect the α particles that passed through the foil (fig. [4.6]). The estimated experimental error is estimated by the maximum deviation of single measurements to an average detection efficiency and is about 1 %. The Si-surface-barrier-detector is much smaller than the foil radius, just about 5 mm in diameter. So, only α particles passing through a small area in the middle of the foil are detected by the Si-Detector. By just using a very small inner part of the foil the transmission probability is 100% because for a somehow reasonable adjustment of the TOF-detector the transmission is only limited by effects concerning the outer part of the foil. This is experimentally verified by variations of the electrode potentials and the magnetic field (fig. [4.7]). Measuring the amount of signals $N(\alpha)$ on the Si-detector compared to coincident signals $N(\alpha) \wedge N(MCP)$ of the Si-detector and each MCP-detector $N(MCP)$ for a fixed time one can get the detection efficiency easily. The detection efficiency for α particles with a kinetic energy of about 4.8 MeV/u is assumed to be 100% for the Si-detector. The detection efficiency can be calculated by

$$\varepsilon_{Tot} = \varepsilon_D = \frac{\frac{dN(\alpha)}{dt} \wedge \frac{dN(MCP)}{dt}}{\frac{dN(\alpha)}{dt}} \tag{4.2}$$

The ion detection efficiency is measured for different foils and by changing electrode voltages and the magnetic field. The measurement by varying the magnetic field also shows the independence of the detection efficiency on the position of the electrons hitting the MCP (fig. [4.7]). The kinetic energy of the electrons imping on the MCP-detector is sufficient to be used in the saturation region of the detection efficiency (fig. [4.8]).

Typical measured ion detection efficiencies for carbon foils are in the range of 80% for foils down to 8 $\mu g/cm^2$. For smaller thickness the ion detection efficiency drops because less electrons are created in the foil because the secondary electron cascade can not develop completely. Creation of less electrons also implies the decrease of the

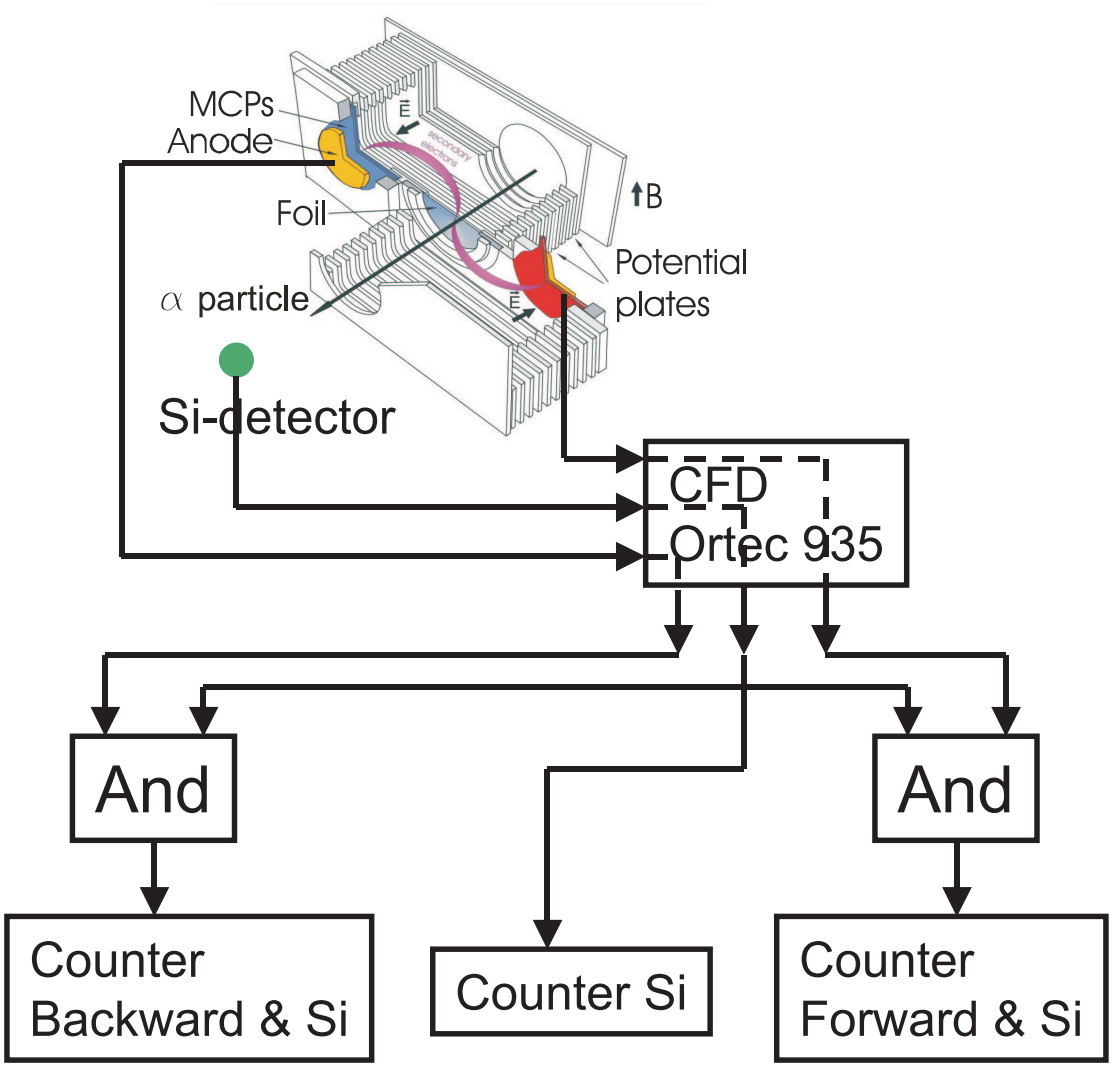

Figure 4.6: Setup used for measuring the ion detection efficiency. Therefore the α particles are detected by an Si-surface-barrier detector installed behind the detector foil. Using a coincidence technique it is possible to measure the ion detection efficiency. It should also be noted that the transmission probability is excluded in this measurement. This is caused by the small active area of the Si-detector. Only projectiles passing a small spot at the middle of the foil are contributing to signals on the Si-detector. Therefore the signal created by the α particle and each of the MCP-detector branches that detect the electrons are set into coincidence using a logical AND-module of the company CAEN. By comparing the count rate of the detected α particles and the coincident signals of the α particles and the MCP-detector the total detection efficiency is determined.

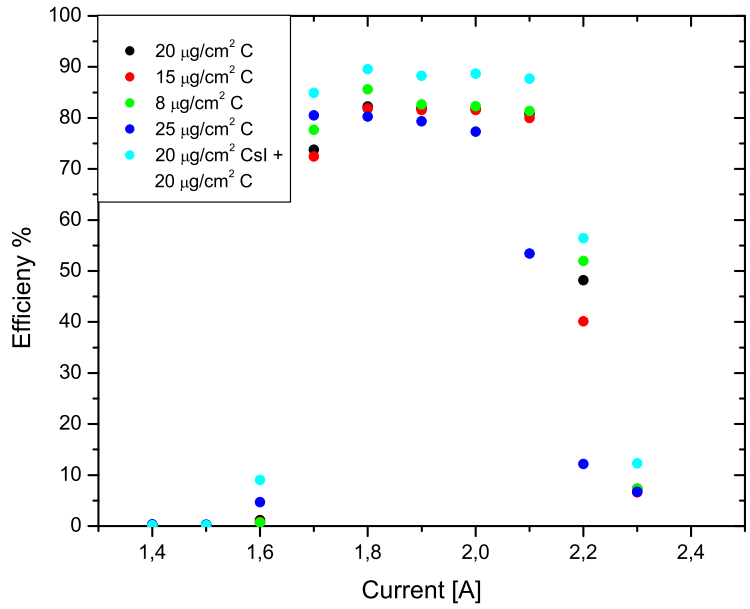

Figure 4.7: Ion detection efficiency measured in dependence of the magnets current. The graph shows that the ion detection efficiency stays constant over a broad range of the MCP surface. Changing the magnetic field yields a variation of the final position of the electrons on the MCP in horizontal direction. Estimated experimental error is given by ± 1 %.

ion detection efficiency (eq. 4.3). In this work the ion detection efficiency of the CsI coated foil with thickness of about 10 $\mu g/cm^2$ of CsI is measured. All other values for the detection efficiency of the CsI coated foils are converted from absolute secondary electron yield data taken from D. Rosenauer [Ros-92] by converting the yield into efficiency using equation 3.63. All other measurements on the carbon targets are done within this work.

The measurement of the CsI coated foil of thickness of 10 $\mu g/cm^2$ shows that the detection efficiency is just slightly increased compared to the pure carbon foils (fig. [4.9]). But the coating was originally chosen to give a higher secondary electron yield and therefore a higher detection efficiency because of CsI being an insulator.

It is important to know that in first order the inelastic mean free path of an electron in a solid just depends on the band structure. Therefore the inelastic mean free path is roughly divided into insulators, semi-conductors and metals. It is also known that for different metals the inelastic mean free path is roughly the same [Vos-88]. That

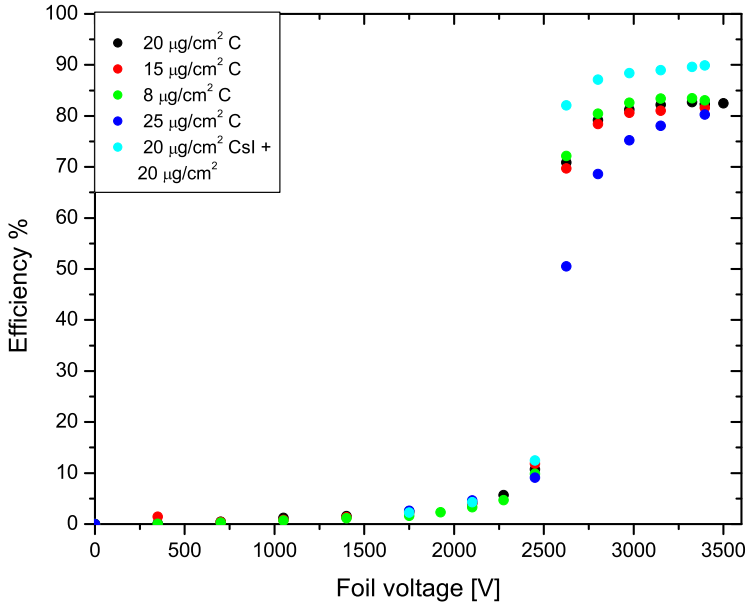

Figure 4.8: Ion detection efficiency measured in dependence of the foils voltage. The decrease of the voltage changes the ion optics of the detector and so less ions are able to hit on the MCP-detector. Changing the voltage on the foil the kinetic energy of the electrons is changed and so the detection efficiency starts to drop for kinetic energies less than 300 eV. It can be recognized that the foil voltage applied supports sufficient kinetic energy to the electrons to run the MCP detector in a stable and highest detection regime. Estimated experimental error is given by ± 1 %.

means that the electrons travel the same distance in materials with different densities. Because of using the mass density as thickness description of the foils, the density of the material needs to be included.

Therefore metalic solids with different densities have the same length the electrons have to travel [Pen-76]. But in the description of mass densities their length of migration is different. Because of the higher density of the CsI compared to carbon the layer thickness is much smaller which means that a thicker coating is needed to let the electron cascade develop completely.

The second fact is that the inelastic mean free path is much bigger in insulators [Has-98], [Low-04], [Ohy-04], [ICRU-99], [Shih-97]. If an electron is excited up to the conduction band or in a quasi continuum state the probability of collisions with other electrons is much smaller than in a metalic solid. The inelastic mean free path of the electrons is bigger and so the cascade also needs an additional length to develop. So, the satura-

	$\rho[g/cm^2]$	β_δ	λ_S [Å]	λ_δ [Å]	$\Delta[\frac{\mu g/cm2}{keV}]$
CsI	4.51	0.2	50± 32(fitted)	1210± 775 (fitted)	85± 24(fitted)
C	1.65	0.2	19	460	7

Table 4.2: Overview of the used and fitted parameters for describing the change of detection efficiency with the target thickness. The fitted diffusion length and the density of the CsI coating is larger which yield a thicker material thickness for being in a saturation region for the creation of secondary electrons.

tion thickness of the secondary electron yield for insulators an increased thickness than for metals. The secondary electron yield for CsI at the saturation thickness is higher because of the smaller barrier the electrons need to overcome and their larger inelastic mean free path (chapter 3.3.4.1).

To describe the detection efficiency two equations are necessary. Combining equation (3.51) and (3.63) the detection efficiency of a MCP is coupled to the thickness dependence of the secondary electrons. So the detection efficiency is given by

$$\varepsilon_D = 1 - exp\left(-\varepsilon_{MCP}\left[\frac{\Lambda}{2-\beta_\delta}\frac{dE}{dx}\left(1-\beta_\delta e^{-x/(\lambda_\delta\rho)} - (1-\beta_\delta)\,e^{-x/(\lambda_S\rho)}\right)\right]\right) \quad (4.3)$$

The values which are necessary for carbon and the already fitted values for CsI are given in table [4.2]. For the CsI target the same $\beta_\delta = 0.2$ is used while the diffusion length and the proportional constant are expected to be different. The ratio of the diffusion length for the fast and slow electrons for CsI are also taken the same like for carbon. Therefore the free parameters are the proportional constant Λ and the slow electron diffusion length λ_S that are determined by fitting equation 4.3 to the experimental values of the thickness dependent detection efficiency for CsI using a least mean square routine. The fitted diffusion length of electrons in CsI λ_S is about a factor 2.6 higher than for carbon. Qualitatively this increase is in agreement with the empirical transport theory. But for a pure CsI target experimental data from other authors yield a value of about 215Å [Low-04], [Hen-81]. So the fitted diffusion length seems to be underestimated. Reasons could be that the combination of CsI-C layers with the ratio of $10-20$ for each detector branch could yield an effective diffusion length. So the diffusion length needs to be weigthened with this thickness and their different diffusion length of carbon and CsI. Using the thickness layer ratio and the diffusion length for carbon of 19Å and the expected value of CsI of 215Å an effective diffusion length of about 89Å can be achieved. This value is already closer to our fitted value but still a little bit off. This difference could have several reasons like solid state effects at the coupling surfaces of the material or inhomogeneous thickness coverage of the foil with CsI. This last effect would yield that the cascade develops even more in the carbon layer which even more decrease the diffusion length. Another uncertainty is the assumed density of the

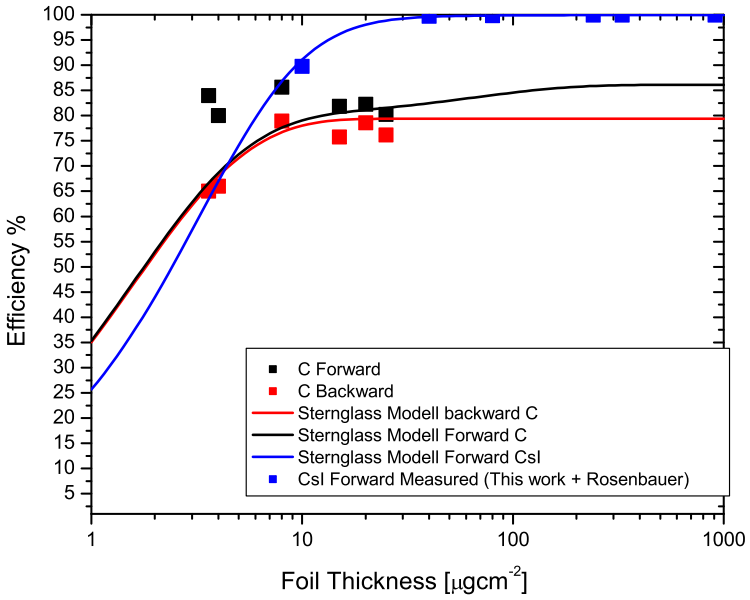

Figure 4.9: Measured detection efficiencies of different carbon foils and CsI coated carbon foils with respect to their thickness. The blue line represents the expected thickness behavior of a CsI foil using equation 4.3 and the corresponding values. The black line represents the expected thickness behavior of a carbon target using equation 4.3 and the corresponding values. It can be noticed that a thicker coating of CsI is necessary to reach an ion detection efficiency of about 100%. Estimated experimental error is given by ± 1 %.

evaporated CsI which is taken from solid crystalline structure. For evaporated CsI one could guess that the density is also slightly decreased which causes the diffusion length to be increased. The detailed description of this phenomena is out of the scope of this work. Therefore the conclusion is that the effect of increased secondary electron yield and diffusion length for the CsI covered foil can be qualitatively understood even the absolute diffusion length is underestimated compared to other authors. A thicker layer of CsI is needed to let the electron cascade develop fully which is in agreement with the expectations of increased electron diffusion length in insulating solids. The ion detection efficiency for a coating of 10 $\mu g/cm^2$ CsI is almost the same like for carbon. An coating thickness of about 25 $\mu g/cm^2$ of CsI is expected to give a detection efficiency close to 100%. But the usage of this coating is not very straight forward because CsI is very sensitive to heat and water [Schu-00]. The coating changes its local thickness distribution because of these effects and could cause different local secondary electron yields and so different detections efficiencies.

Detector setting	FWHM true SE
Previous	64ps
New	85ps

Table 4.3: Simulated standard deviation of the time-of-flight distribution for the previous and the electron transport optimized setting.

4.3 Timing Estimations Using Simulations

An important parameter of the time-of-flight detector is the full- width-at-half-maximum (FWHM) of the time-of-flight. It fundamentally limits the precision of the mass-measurements. Because of technical issues it was up to now not possible to measure the time-of-flight for each forward and backward branch with high precision. Therefore the timing is discussed on the basics of the simulation and comparison to experimental data based on the FWHM of the time-of-flight difference of coincident signals of the forward and backward detector.

The time-of-flight is simulated using about 10^5 electrons within the program ITSIM (fig. [4.10]). The initial spatial distribution is chosen to be homogeneous all over the foil. Therefore the so calculated time-of-flight distributions can be understood as a worst case timing calculations. It can be shown that the time-of-flight width at position smaller than 15 mm radius of the foil is about 45ps that is in principle given by the initial kinetic energy distribution. Only for outer radial position the time-of-flight starts to deviate. In the outer region with radius larger than 15 mm the time-of-flight deviation can additionally increase up to 20 ps FWHM.

The impact of incorporating more details out of the secondary electron spectra, the Auger-electrons of about 250 eV of the KLL transition in carbon are additionally considered. Therefore a discrete electron energy abundance at 250 eV is created while taking care that the abundance ratio of true secondary electrons to Auger electrons is about 100:1 (fig. [3.12]). Considering the convoy electrons for the offline setup which uses 4.8 MeV α-particles no significant increase of the time-of-flight width is observed within the main peak in the time-of-flight spectra. Concerning the energy of the α-particles the convoy electron energy is 625 eV. The calculated full-width at half-maximum of the time-of-flight for the previous and new setting are given by figure [4.3]. Increasing the maximum energy of the energy distribution of about 1 eV broadens the time-of-flight FWHM about 12 ps. To compare the timing to the experimentally measured values a more realistic initial kinetic energy distribution of the secondary electrons needs to be known.

It should also be noted that the expected energy of the convoy electrons using ions with 300-400 MeV/u exceeds the energy acceptance of the TOF-detector. Therefore

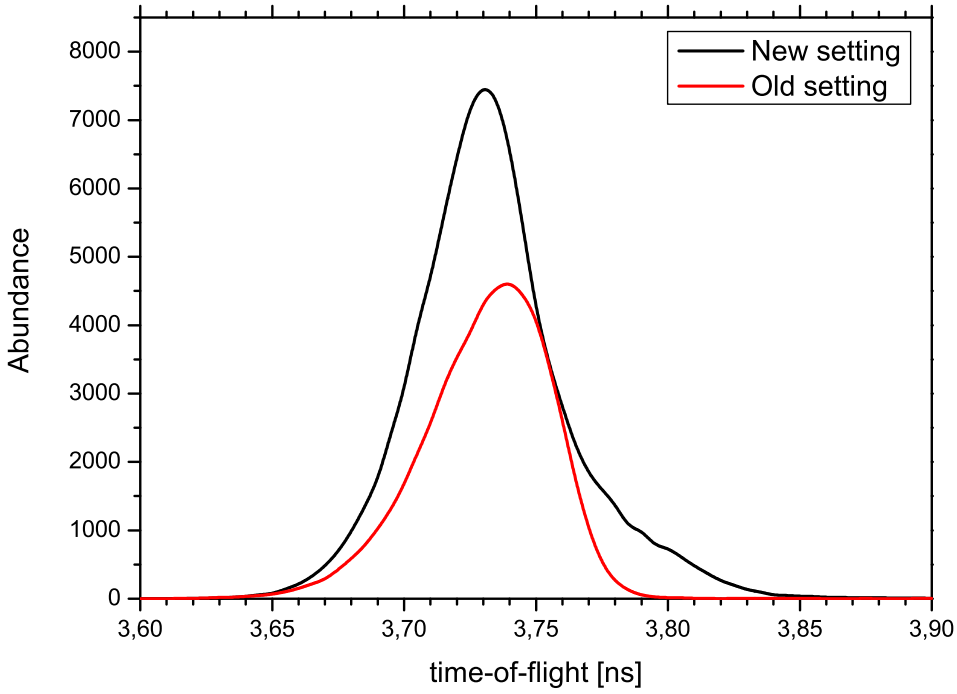

Figure 4.10: Calculation of the ejection time using a Maxwell Boltzmann distribution with $E_{Max} = 1.8$ eV and the previous and new transport efficiency optimized setting. The comparison of the calculation shows a slightly higher standard deviation of the efficiency optimized setting of about 12ps.

the convoy electrons are so fast that they can not be bent onto the micro channel plate detector.

The influence of the initial starting position on the time-of-flight for a foil that is not totally flat and yields a change of 3 ps in the FWHM by a change of the position in z-direction by 1 mm. Therefore the effect can be neglected. Offline measurements for the previous detector setting show that the FWHM of coincident signals created by the forward and backward detector are 134 ps by using an aperture that illuminates the foil area completely [Rad-94]. For the measurements two constant fraction discriminators are used to process the timing measurement. Tests show that each channel of the Constant fraction discriminator have a standard deviation of about $\Delta t_{CFD} = 28$ ps that is mainly caused by the amplitude-walk effect. From the calculation and by assuming that both time-of-flight processes of each branches are independent a standard deviation of $\sigma_{Coin} = \sqrt{2(\Delta t_{TOF})^2 + 2(\Delta t_{CFD})^2} = 48$ ps is expected with the standard deviation for

the time-of-flight for the previous setting given by $\Delta t_{CFD} = 28$ ps. So, the calculated FWHM is about $FWHM_{Coin} = 112$ ps. Therefore it seams that there could be more effects that increase the experimentally measured width which are still not considered. An online-analysis based on a software CFD reduces the timing jitter caused by electronic problems. With this method it was possible to measure a coincident FWHM of about 139 ps [Knoe-08] to 155 ps [Mat-04]. This values are in very good agreement with the offline measured coincident times (FWHM) and in reasonable agreement with the calculation. To improve the timing calculation an experimentally measured secondary electron spectra could be used.

4.4 Rate Capability of the MCP Detector

To test the rate capability of the MCP detector two different experimental concepts are used. The first measurement concept involves using a constant DC current of electrons hitting on the micro channel plate. For the second test the electron current of the source is pulsed so that only a electron bunch hits in a specific time interval of 500 μ s. This measurement method is similar to the process in the ESR where the ions just revolve for some hundreds of micro seconds. Similar experiments on standard MCPs were already done by other groups [Coe-06].

Using both methods it is possible to see how the MCP-detector behaves in a quasi static case and how the parameters of the MCP-detector develop over time for a short intensive bunch. To see the influence of varying different properties on the MCP detector the distance between the MCPs and the voltage over the gap is changed. The model description in chapter 3.8.1 implies that the gap distance and gap voltage could be responsible for variation of the rate capability of the MCP-detector. So, to measure and optimize the rate capability the parameters are varied.

For this experiment an own setup was built. The setup includes an electron impact source that is used to create and direct the electrons onto the MCP detector. After the electron impact source a drift tube is installed to prevent the electrons to be driven to the grounded wall. On the end of the tube the MCP detector is installed that detects the electrons. The creation of the electrons is done by heating up a tantalum wire by applying a current in the order of 1.8 to 3 A. The number of electrons created by the heating process is assumed to be exponentially proportional to the applied heating current. The creation of the electrons by heating the tantalum wire is statistically distributed. So it is a good assumption that the electrons that are directed from the wire onto the MCP are not hitting simultaneously. So its assumed that the setup works with single electrons that hit onto the micro channel plate detector.

Typical average kinetic energies of electrons in the TOF-detector are 700 eV therefore the same kinetic energy is used in the MCP-test setup. The average kinetic energy with which the electrons hit the MCP-detector is fixed by the voltage difference between the source and the MCP. An overview of the typically applied voltages is given in table 7.2.

4.4.1 MCP with Source in DC Mode

For the measurement a blind with a diameter of 15 mm is used to get a more homogeneously local distribution on the MCP-detector. So to determine the dead time values for the total useable detection area of the MCP the rate at which dead time effects occur needs to be extrapolated to 40 mm. Measurements with the full foil diameter of 40 mm show agreement with the extrapolation of the critical electron rate.

In the DC mode the electron current is changed while for every settings the parameters of counts per time, current on the MCP anode and the pulse height distribution are taken (fig. [4.11]). The electron current is simply changed by increasing the heating current on the tantalum wire. The counts per time are measured by using a CFD of the company Canberra and a counter that counts the pulses for about 1 minute. The output current can be measured with an electrometer while the pulse height distribution can be measured by using a 1 GHz oscilloscope of the company LeCroy. The scope triggers on the MCP signal and measures the amplitude of the maximum of the signal and creates a histogram of it that can be saved on the hard disc of the scope for every setting. The error of the count rate and the MCPs output current are estimated by the deviation of single to the average value of multiple measurements. The error of the gain is calculated by the error-propagation using the errors of the count rate and the output current.

For low count rates the electron current shows exactly an exponential behavior in dependence of the heating current while for higher currents the behavior broke down. It is simply caused by dead time effects of the MCP-detector. So to extrapolate the electron current for higher rates a least mean square fit to the lower count rates is used. The heating current behavior is fitted with an exponential curve. After the determination of the fit parameters it is possible to extrapolate the real incident electron current for higher heating currents. The maximum detection efficiency for this setup is limited by the open-area-ratio of the MCP which yields 60% and needs to be considered for the determination of the real electron rate. The limitation of 60% in this setup is caused by the fact that only uncorrelated single electrons hit onto the MCP.

The experiments show that the effect of decreasing gain starts at a value of about 10^5 Hz to 10^6 Hz dependent on the distance of the MCPs d_G and the gap voltage U_G (fig. [4.12]). The first effect that can be seen is a deviation of the output current linearity from the input current that already shows the decrease of the gain (fig. [4.13]). So the pulse height distribution shifts to smaller amplitudes and changes the shape to a none peaked histogram (fig. [4.14]). As long as the threshold of the CFD is small enough, no decrease in the count rate linearity is observed. But as soon as the distribution drops to amplitude values similar to the noise level the detection efficiency decreases significantly. A limiting factor is the total output current of the MCP. If the output current reaches roughly 10% of the strip current dead time effect start because the power supply is not able to recharge all channels. The other effect is a more geometrical effect that should be dominant for operation of the MCP with times shorter than the recharge time. If a channel is excited more than two times without being able to recharge completely, the gain also drops [Fras-91]. Fixing the voltage and varying the gap size the geometrical spread of the electron cloud hitting on the second channel is changed mainly. Increasing the distance more channels are excited what results in a higher gain and so in higher amplitudes. Fixing the distance and changing the voltage the spread of the electron cloud is changed and also the kinetic energy of the electrons that hit on the channel

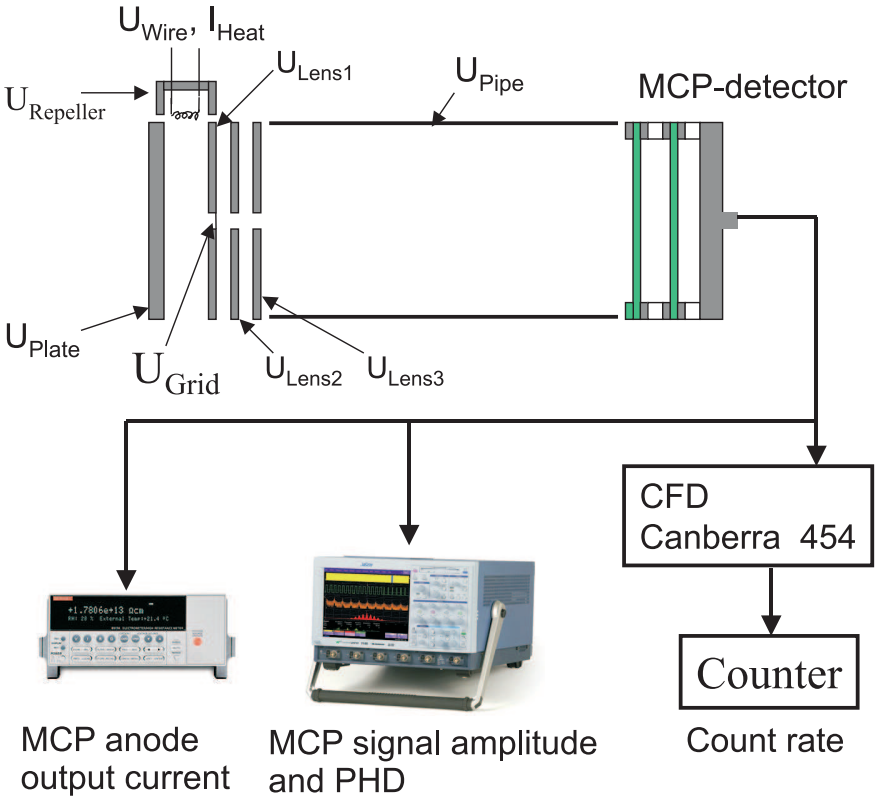

Figure 4.11: Setup for measuring characteristic properties of a MCP in defence of a constant dc particle flux. The electrons are created applying a current to the tantalum wire that creates electrons. By applying reasonable voltages to the other electrodes and lenses an electron beam can be lead through the grid and the pipe onto the MCP. The pipe is set to the same voltage of the first MCPs surface to prevent significant beam widening because of the close vacuum chamber surface. To increase the beam intensity a higher heating current is applied. Different parameters as the count rate of the electrons coming from the source, the MCP output current and the pulse height distribution for different electron fluxes are measured.

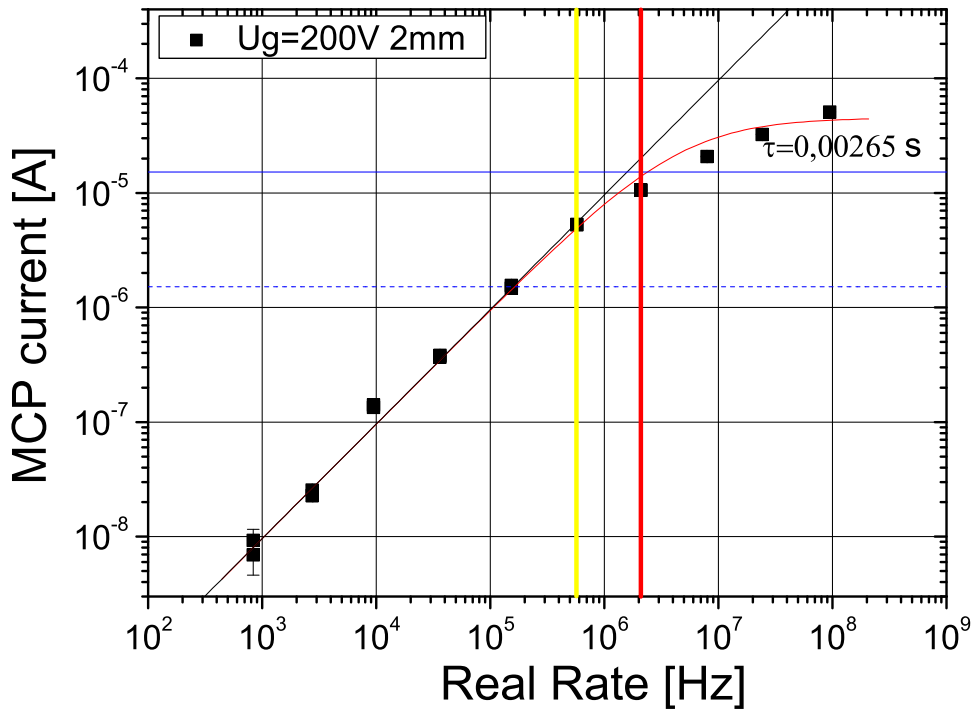

Figure 4.12: Electron rate dependency of the output current of the MCP for a gap voltage of 200 V and 2 mm distance like the MCP detector is used in the current TOF-detector. The output current linearity shows a linear relationship up to a point where less gain is supported from the MCP. This effect is caused by the finite recharge time of the channels. The yellow line indicates the rate at which a shift of the pulse height distribution occurs while the red line indicates the rate at which the pulse height distribution is not peaked anymore. From the spatial spread model, using eq. 3.60 it is calculated that N channels are excited in the second MCP. This value was used in conjunction with eq. 3.67 to make a least mean square fit for the recharge time of a micro channel (red curve).

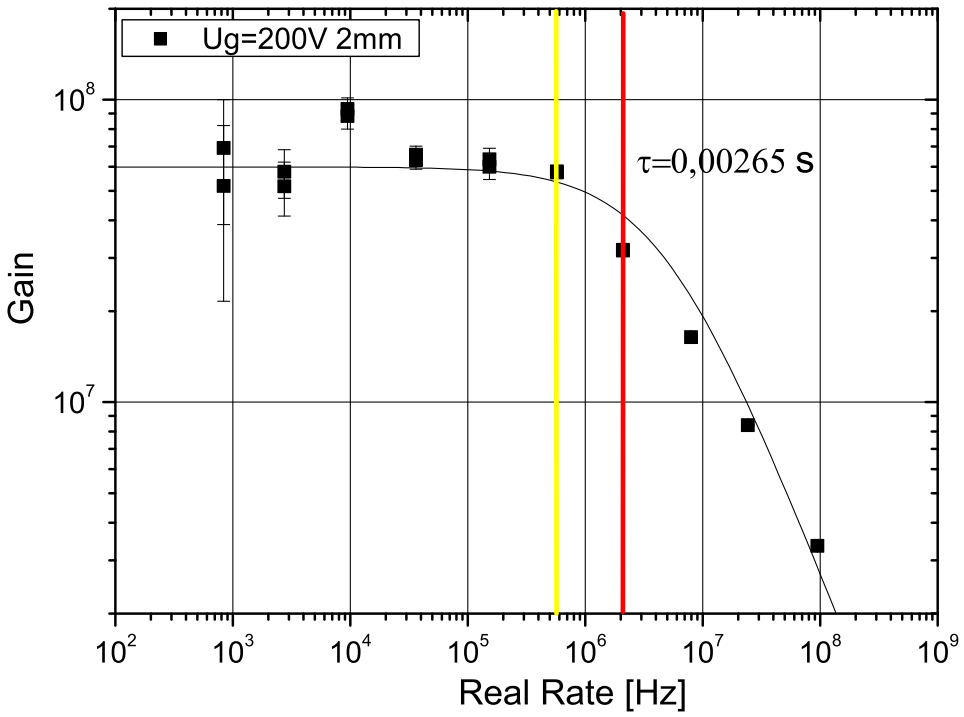

Figure 4.13: Electron rate dependency of the gain of the MCP for a gap voltage of 200 V and 2 mm distance like the MCP detector is used in the current TOF-detector. The detectors gain is calculated by the ratio of the output current and the input current gathered from the count rate measurement. The gain stays constant up to a specific rate. Then the gain starts to drop because of the finite recharge time of the micro channels. The gain is fitted using eq. 3.66 (black curve). While the position of the yellow line indicates the rate at which a change of the pulse-height distribution starts, the red line indicates the rate at which the pulse-height distribution changes to an exponential.

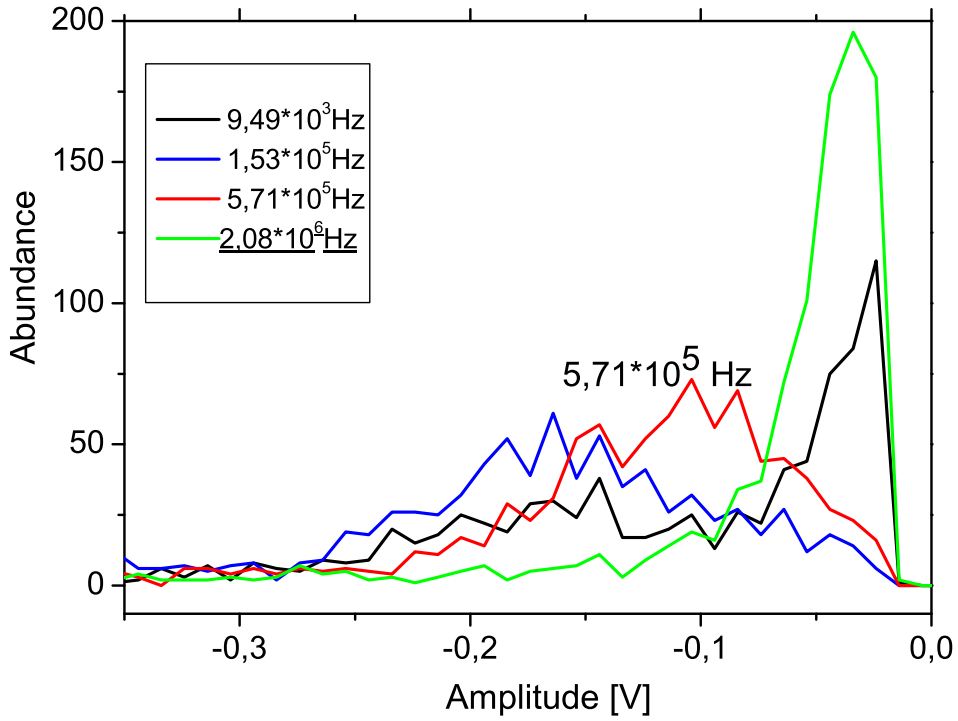

Figure 4.14: Development of the pulse height distribution for different electron input rates and a gap distance of 2 mm and voltage of about 200 V. The histogram clearly shows the influence of the decrease in gain onto the phd. While for low rate the pulse height distribution stays at the same position and is peaked for higher input rates the phd shifts to lower amplitudes and at the end lose their peaked structure. This effect is caused by the nonlinear relation of the gain at higher rates which causes the amplitudes to drop and the loss of the charge saturation process which causes the peaked structure of the phd.

plate. Typical recharge times for one channel, extracted from the measurements, are in the same order of ms like expected from the RC recharge model [Wiz-79].

4.4.2 Source in Pulsed Mode

To experimentally simulate the impact of a short electron bunch onto the MCP the electron source is used in a pulsed mode (fig. [4.15]). Therefore the repeller of the source is used.

The pulser is supported by a TTL-signal with pulse length of 500μs and a repetition frequency of 1 s. The repetition is chosen to be 1 s to make sure that the MCP is recharged before the next pulse of electrons arrives. The pulser is supported by two different voltages. The pulser switches in dependence of the TTL signal to one or the other channel. So it is possible to "close" and "open" the source. The MCP signals are saved by a 1 GHz scope of the company LeCroy while the trigger on the scope is set to the TTL-signal. The spectra for every shot are saved and analyzed later on. Changing the heating current the incoming electron number is changed like for the DC-mode. For low rates the amplitude-time spectra show no time dependency while for higher rates dead time effects cause the amplitude to drop with increasing time to an quasi static lower value (fig. [4.16]). The real incoming rate is determined by counting the number of peaks within the 500 μs for low rates. Taking care that only 60% are detected the real incoming rate can be determined. For higher rates the current deviates again from the exponential law like in the DC mode and the real incident rate needs to be extrapolated again. Another problem of specifying the exact electron rate is the time dependency of the efficiency. Because of the drop over time the real electron rate could be underestimated.

The gain and amplitude is expected to drop exponentially in first order equation 3.71. So to get a more detailed description of the detectors behavior the amplitude decay over time is fitted with an exponential curve of the form:

$$A(t) = y_0 + Be^{-\frac{x}{\tau}} \tag{4.4}$$

Measurements show that the slope of the decay increases (fig. [4.19]) with higher rates while the quasi static amplitude decreases (fig. [4.20]) as expected from eq. 3.71. To examine the development over time of the detection efficiency the area of the pulse height distribution is used. The abundance of the pulse height distribution is normalized to 1 at the location of the maximum. For non-peaked distributions the normalization could not be very accurate because the maximum is not present anymore or vanished in the noise so the area could be overestimated for this curves. The area under the curve for 0 to 10 μs is fixed to the detection efficiency of about 60%. The detection efficiency shows in first order the same decay constant τ for the specific rates (fig.

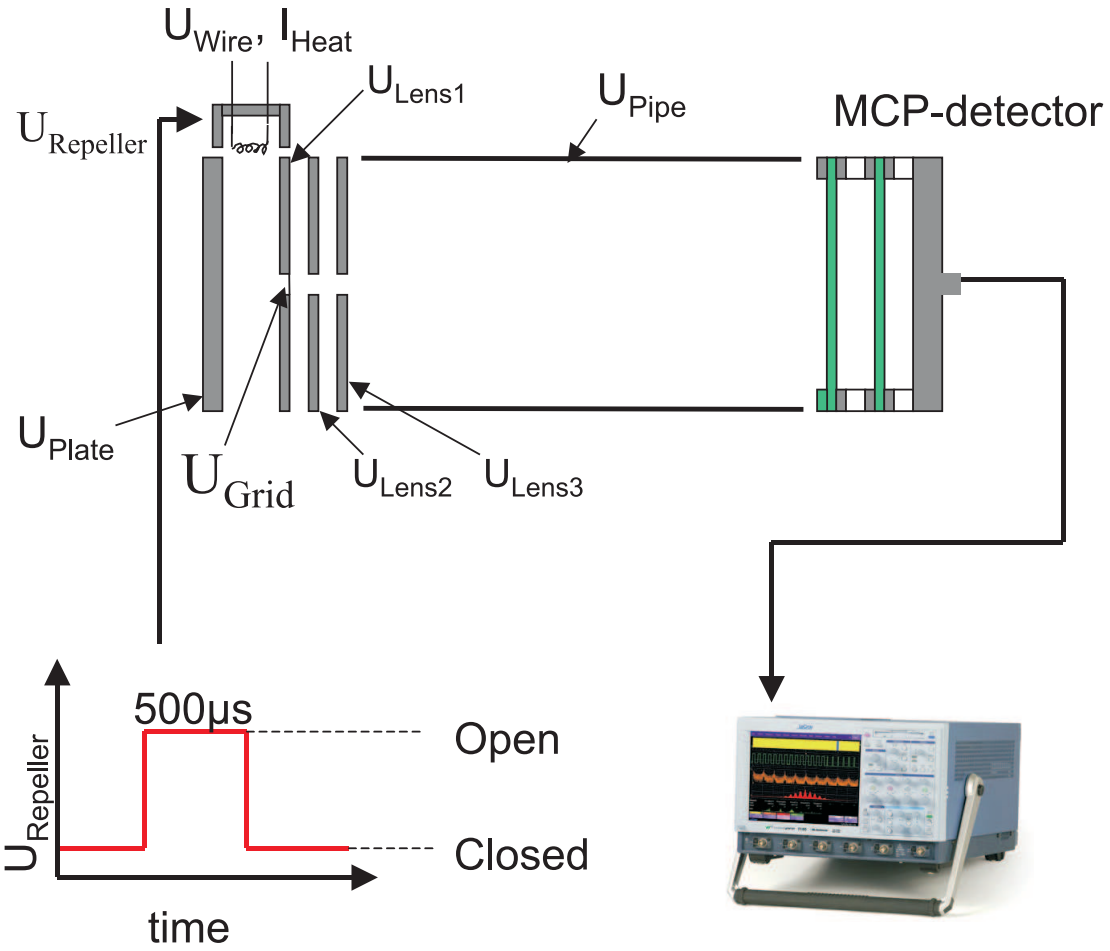

Figure 4.15: Setup for measuring characteristic properties of a MCP in presence of a short electron bunch. Therefore the same voltages of each electrodes as in the DC mode are used. The only difference is that the voltage repeller is operated by a pulser. The pulser switches the voltages of the repeller depending on the applied TTL-signal. The two voltages are chosen in that way that one voltage does not allow electrons to hit the MCP while the other voltage is at the right voltage so that the electron can hit the MCP-detector. A typical time length of the pulse is 500 μs while the repetition rate is set to 1 s to allow all the channels to be recharged after each electron bunch.

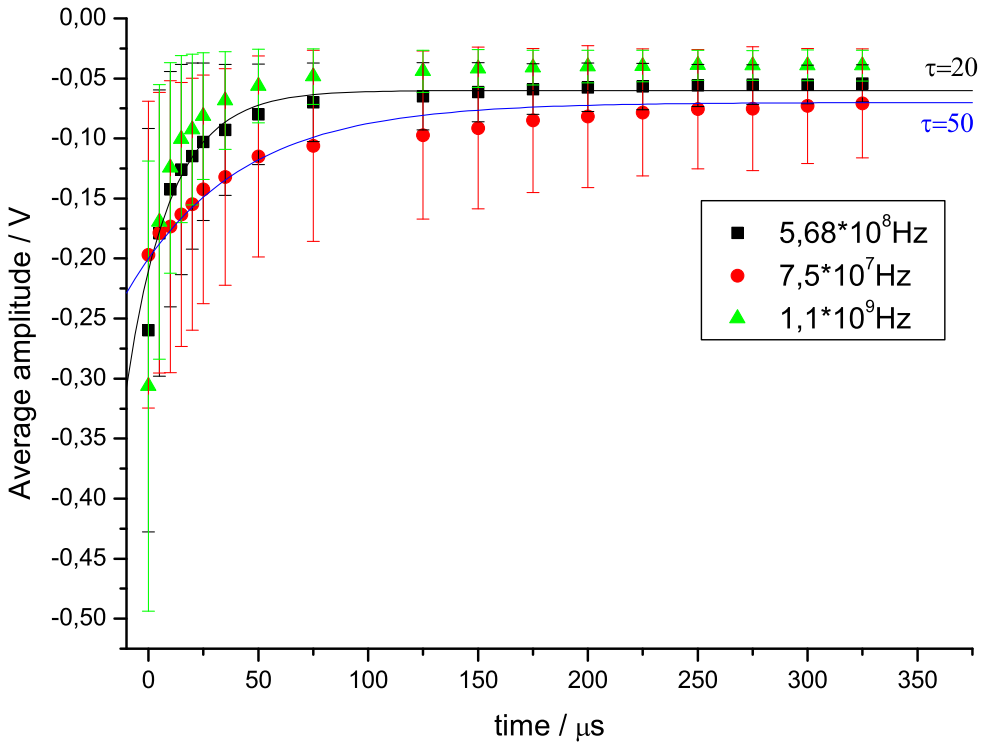

Figure 4.16: Time development of the average signal amplitude during the electron bunch. Therefore the voltage between the MCPs was about 480 V. It shows clearly the expected exponential decay of the amplitude down to a quasi static value. This effect is caused by the exponential decrease of the gain. The error of the average amplitude is simply given by the statistical variation of the amplitude.

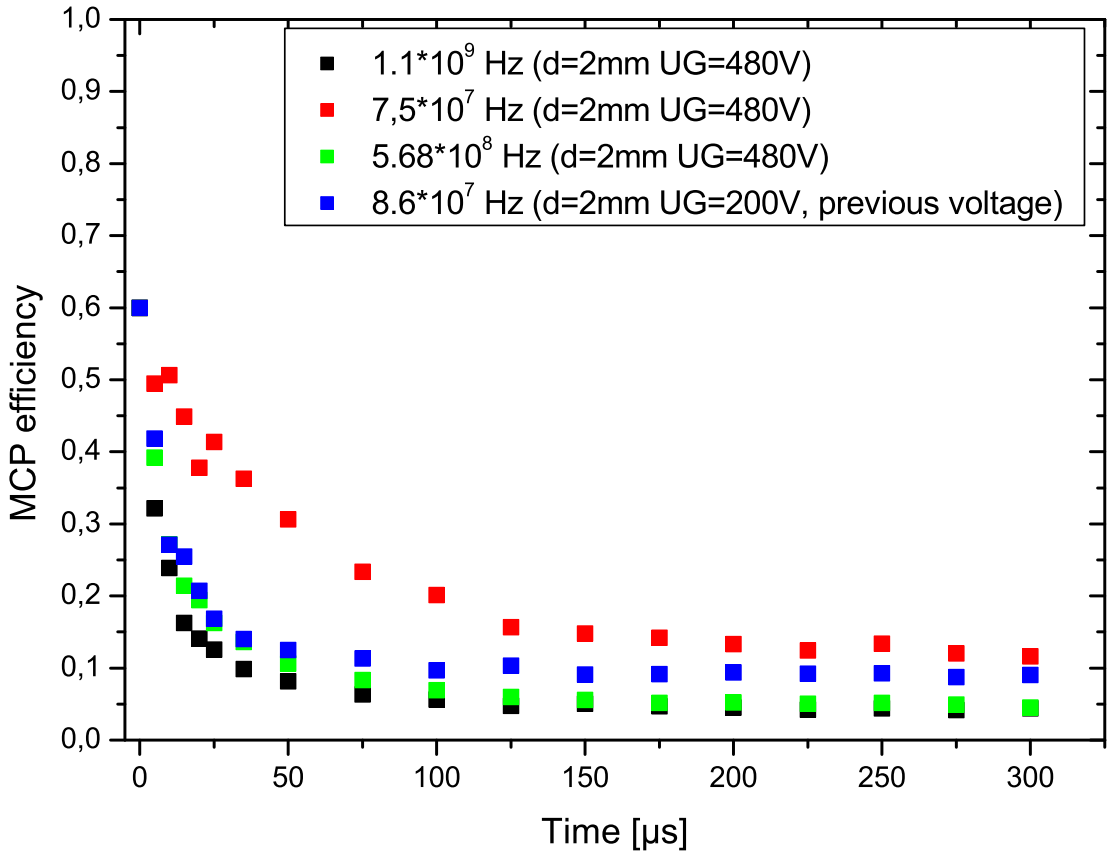

Figure 4.17: Time development of the detection efficiency during the electron bunch. The detection efficiency is calculated by identifying the area under the normalized pulse height distributions. The calculated area for the first time windows is then normalized to be 60%.

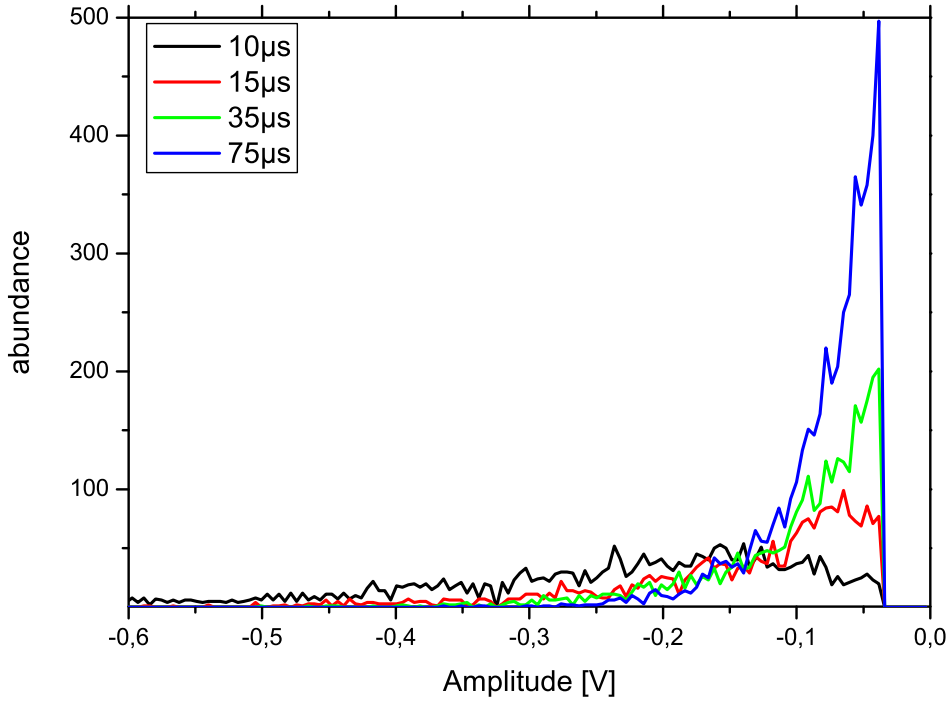

Figure 4.18: Time development of the pulse height distribution during the electron bunch. The development over time shows clearly the shift of the phd to lower amplitudes and the disappearing of the peaked structure. It can be seen that while the gain decreases more and more signal disappears in the noise and that the pulse height distribution changes back to a quasi exponential distribution that leads to a lot of small signals. This effect leads in the end to a decrease of detectable signals and so to a decrease of the detection efficiency which is given by the area under the curves.

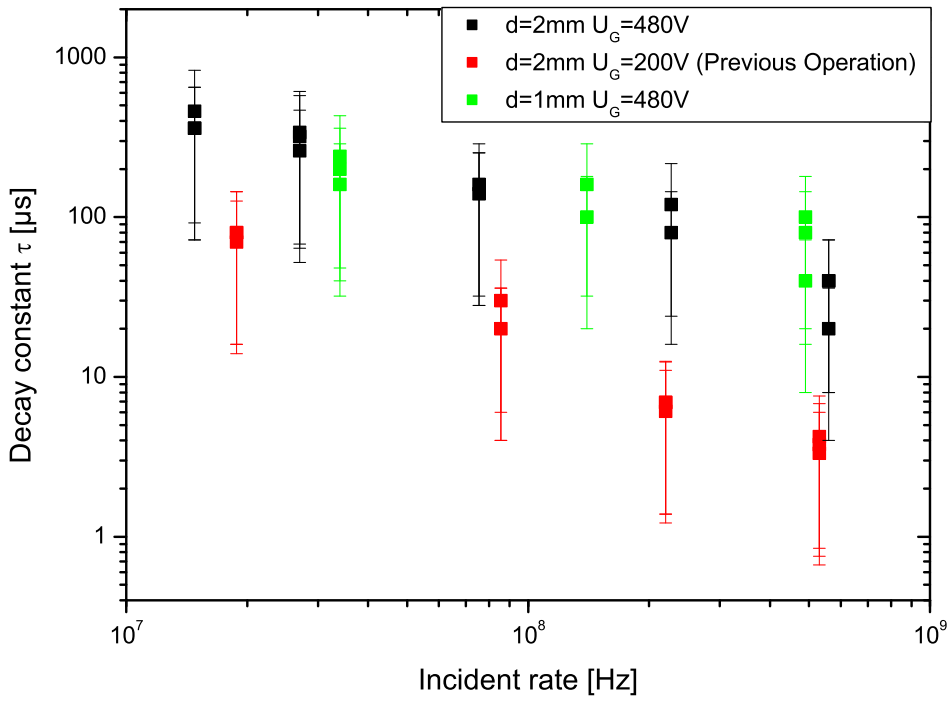

Figure 4.19: Summary of the exponentially fitted decay constants of the temporal development of the amplitudes for different rates, gap distances and gap voltages. The decay constants show all the same trend. The decay constants decrease with increasing input rate which means a faster amplitude, gain and so efficiency decrease for higher rates. While the increase of the gap voltage on the decay constant is clearly seen the influence of the gap distance can not be seen clearly. It seems that a higher voltage focusses the electrons from the first MCP more onto a smaller area on the second MCP what yields less excited channels. This effect causes a higher rate capability of the MCP because more channels per shot are available in the average. The error is estimated by the maximum deviation of a single decay constant compared to the average value.

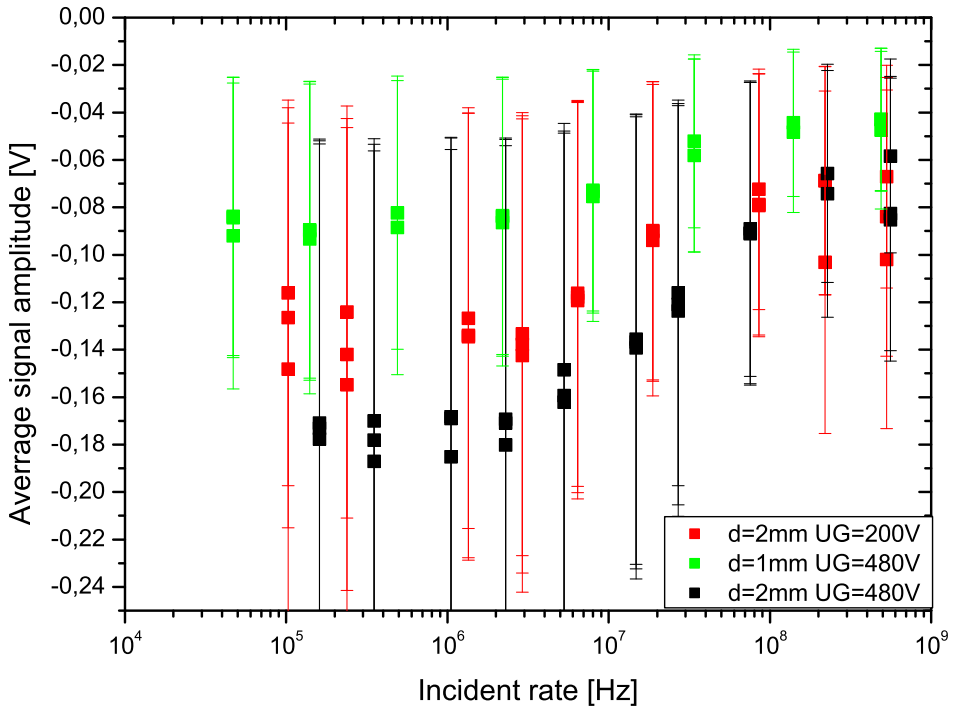

Figure 4.20: Summary of the overall averaged amplitude of a spectra for different rates, gap distances and gap voltages. Because of the decrease in gain for high rates it can be seen that the average amplitude and so the detection efficiency also decreases. The error is estimated by the maximum deviation of a single average amplitude compared to the average value.

[4.17]) compared to the decay of the amplitudes. So the time dependent detection efficiency of the micro channel plate detector and for one electron can be written as

$$\varepsilon_{D,1e^-}(t) = (\varepsilon_0 - \varepsilon_\infty)e^{-\frac{t}{\tau}} + \varepsilon_\infty \tag{4.5}$$

while $\varepsilon_0 = OAR = 0.6$ is the efficiency and equal to the open-area-ratio of the MCP. If recharging and excitation of channels are in equilibrium the quasi-static efficiency is given by ε_∞ and is dependent on the incoming rate.

The gap distance as also the voltage between the MCPs is varied. The influence of the gap voltage U_G onto the rate capability shows a dramatic change in the behavior (fig. [4.19]). The slope of the decay is slower for higher voltages. This could be understood in a geometrical way. For higher voltages less channels are excited because of less spread of the electron cloud eq. 3.60. So in the average the MCP can be more resistant to higher rates. The limitation in the pulsed mode for low charged particle with low projectile number should be mainly limited by the geometrical effect and not by the strip current limitation. During the measurement time of 500 μs no significant current compared to the strip current flows out of the MCP. Let us assume 10 electrons hitting on the MCP detector that is operated with a gain of 10^8 while the bunch length is 400 μs. The output current is equal to 0.4 μA. A typical resistance for an EDR MCP is in the order of 20 MΩ with a typical operation voltage of 1000 V. Then the strip current is about 67 μA. An effect of the output current would be expected at an output current of 6.7 μA which is still a factor of roughly 16 away. So, by decreasing the distance between the MCPs one should win in rate resistance. But this effect could not clearly be observed. A decrease of the channel diameter of the MCPs itself could yield higher rate resistance and therefore a less time dependent efficiency for exotic mass measurement. Therefore the advise is to increase the gap voltage up to 480 V to get a higher gain and so a better peaked pulse height distribution but exciting less channels. The gap distance could be decreased down to 1 mm but further decrease did not show a significant improvement.

5 Online Experiment with a Stable Ni-Isotope Beam

From offline experiments the importance of the secondary electron creation transport, detection efficiency and rate capability is shown. The electron transport and the detection efficiency can be quantitatively understood using simulations and experiments. To verify that no additional important effects occur in online-measurements with the ESR an experiment is performed.

A stable bare Ni-beam is chosen as projectile to have no additional decay branches. A beam of exotic nuclides and the decay of them could otherwise lead to an additional time dependency of the results. Therefore a $^{64}Ni^{26+}$ beam is accelerated up to 11.31 MeV/u in the LINAC and injected into the SIS. The SIS accelerates the beam further up to 497.8 MeV/u and ejects the bunch onto the SEETRAM [Jur-02] that is used to strip the remaining electrons from the nuclides. The bare Ni nuclides are then transferred through the FRS into the ESR with a kinetic energy of 372 MeV/u.

To ensure that the voltages on the electrodes, the foil and the MCP detector and the magnetic field of the detector can be changed without shutting down the beam each time, a remote control based on the LABVIEW software was developed (fig. [5.1]). Using the remote control the voltages on the detector and the magnetic field strength of the TOFs dipole can be changed without entering the ESR-hall. The data is stored by two oscilloscopes simultaneously to make sure that the data is saved even if there occurs a problem with one of them. The trigger of the scopes for starting the measurement cycle is chosen to be the injection trigger of the ESR. So, every time a shot is inserted the scopes saves a spectra with length of about 400μs. The first online tests are tests concerning the transmission probability of the electrons from the foil to the MCP. Therefore two different settings of the electrode voltages are used and the magnetic current on the dipole is changed from 1.6 A to 2.0 A. The both electrode voltage settings are exactly the same that are tested offline and discussed in chapter 4.1. For every detector setting about 10 shots are taken to get a better statistics.

Another test includes the behavior of the spectra by injecting a higher particle number and to see if the expected behavior described in chapter 4.4 can be verified.

And at last a pulser is used to be able to activate the detector at a specific time after the ions already made some turns in the ring. This experiment can support the interpretation of the finite recharge time of the micro channels in the plate.

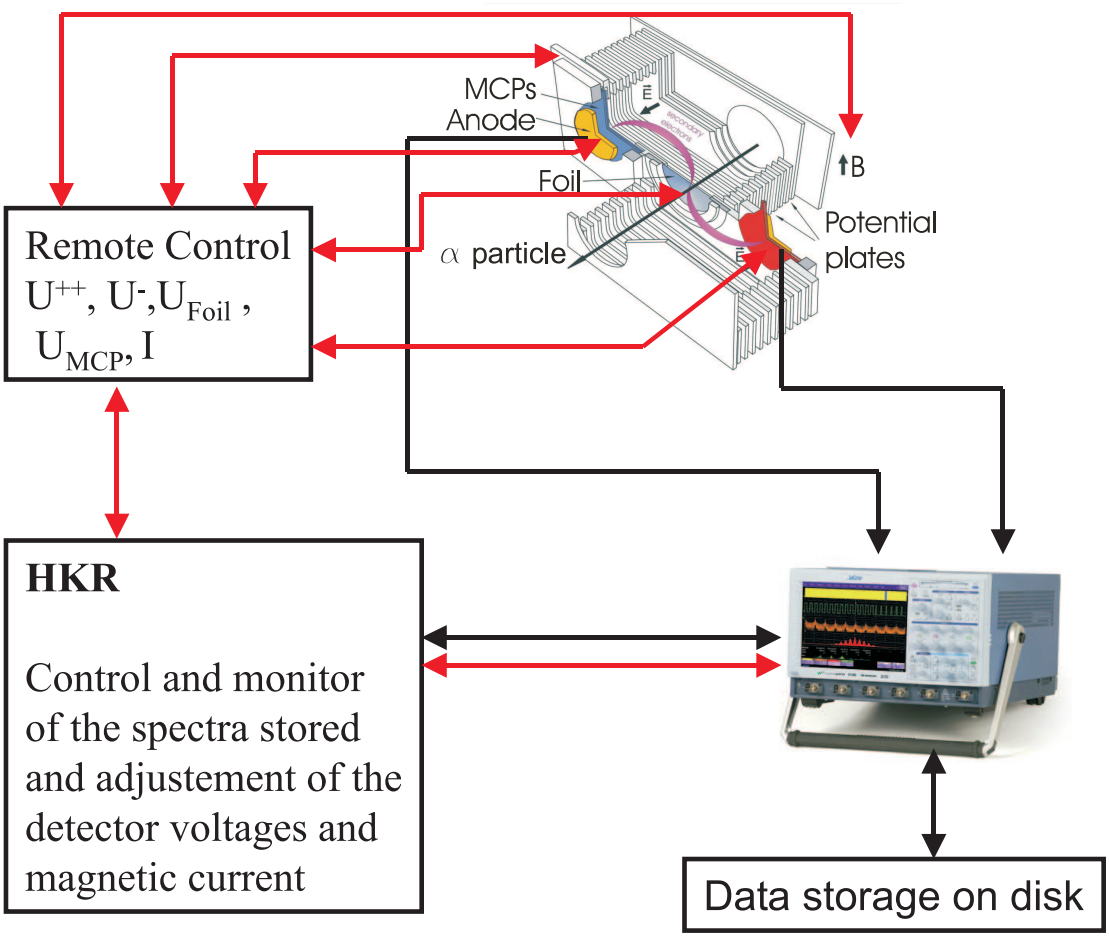

Figure 5.1: Setup used to measure the ions revolution spectra in the isochronous mode of the ESR. The signals of the MCP detectors are transferred to an oscilloscope that samples each spectra and saves it to a hard disk. The scope can be operated from the beam controll room (HKR) and so the data taking can be controlled. For the measurement of spectra using different electrode voltages and magnetic currents a remote control is installed in the ESR-hall to make it possible to change the parameter of the detector directly without entering the ESR.

5.1 Electron Transport Probability

The first test of the detector is done using the standard electrode potentials of the detector while varying the magnetic field. A second test is done using the optimized potentials from the offline test and simulations while also varying the magnetic current. So for every potential and magnetic field setting 10 particle bunches are injected. For every setting 10 spectra are taken.

The data analysis is done offline by using Origin 7.0 [Orig] and home-written C^{++} scripts [Chen-07]. Typically every spectra is loaded into Origin and every peak created by the MCP is analyzed concerning the maximum amplitude and the time location of the peaks maximum. So after analyzing each spectra in dependence of the number of found signals a list of all the found signals including their amplitude and time-positions is created. The so analyzed data is averaged over each setting concerning the number of found peaks for every MCP detector. The error of the found number of peaks per setting is given by the standard deviation of the measurement.

The number of coincident signals in the forward and backward direction is also analyzed by using a script [Chen-07]. The script calculates the time difference between all forward and backward peaks. To get a reasonable time window to define coincident signals the window is varied while observing the number of found coincidences. The number of coincidences grow with increasing time window up to a region where it stays almost constant for longer time windows. The window width starts to get stable at a width of about 1.5 ns. Therefore a difference of 2 ns is chosen as window. This value seems to be reasonable because the typical FWHM of the micro channel plate peaks is about 1.5 ns.

The expected optimum of the magnetic field setting at I=1.8 A shows for each of the electrode settings a maximum of coincidences like expected from the offline analysis (fig. [5.2, 5.3]). The increase of coincidences at the magnetic current of 1.8 compared to the previous magnetic current setting of 1.7 A is a factor of 1.84. The average count number per setting seems to reach a plateau or to drop slightly again after reaching 1.8 A for every MCP detector. This can be explained by assuming that the beam is not adjusted very precisely to the middle. Assuming that the centroid is positioned on one half of the detector foil the simulation shows qualitatively reasonable agreement (fig. [7.5, 7.6]). Within the error bars it can not be seen a systematic improvement by using the new electrode voltage setting but a significant increase can be noticed applying the higher expected magnetic field of 1.8 A to the dipole.

The development over time of the difference of the detected ion number in forward and backward direction shows that using the new setting the standard deviation around the zero line is reduced slightly while the average value of difference in forward and backward direction is four times smaller than for the previous setting (fig. [5.4]). This

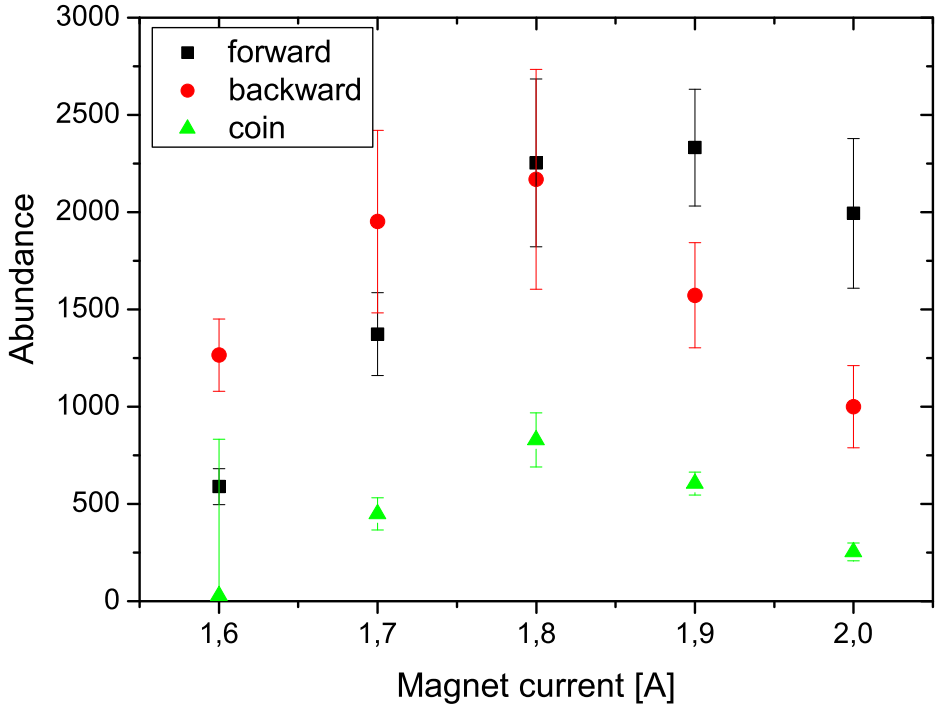

Figure 5.2: Average number of found signals per shot and coincidences in dependence of the magnetic current for the previous electrode voltage setting.

shows already that the transport of the ions in forward and backward direction is better adjusted using the new setting. For the previous setting it also looks like the difference needs a higher order correction to be described. The mean value seems to vary in a special way that could point to a systematical error that is introduced. A systematic error should be observed because of the asymmetric usage of the foil area. Another important parameter that can be extracted from the spectra is the average number of ions that are injected into the ring for each setting. To analyze the spectra for the ion number per shot in the ring the programm m-trace [Sta-02] can be used. The programm is already in use for most of the online analysis concerning the mass measurements. The program determines the equidistant sequences in time for the whole spectra. The program typically starts the analysis at the end of the spectra and analyze back to the beginning of the spectra. Using a least mean square routine the signals are assigned to an individual ion.

The number of sequences found are equal to the number of ions in the ring. The pro-

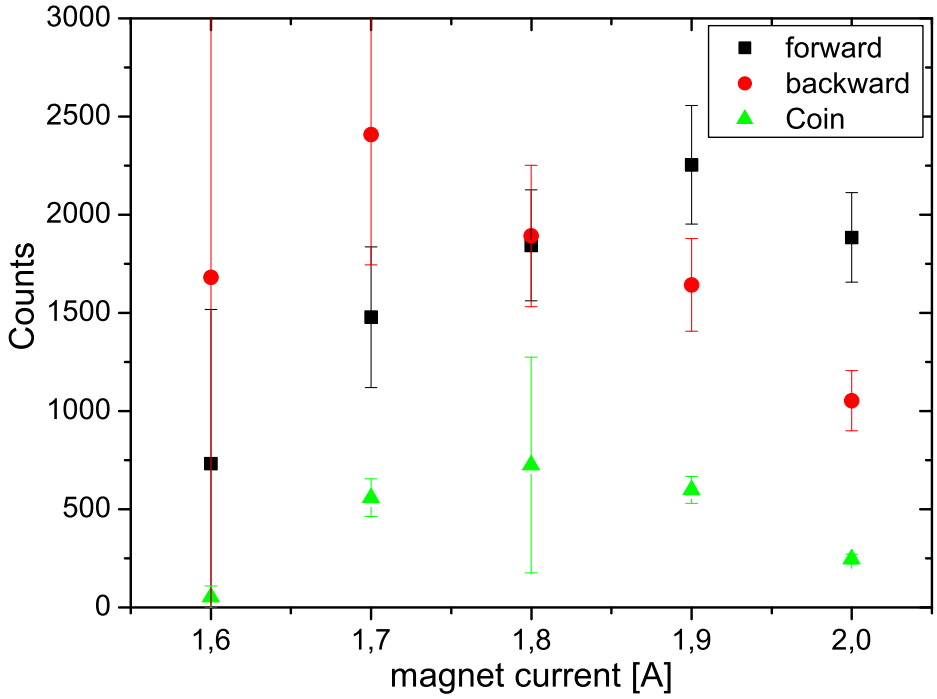

Figure 5.3: Average number of found signals and coincidences per shot in dependence of the magnetic current for the new electrode voltage setting.

gram does not need to have a signal every turn for a specific ions. It is also able to compensate for this effect. So, the number of ions detected with this program is free of the detection and transmission efficiency of the detector and yield the real ion number in the ring. Typical ion number found for the transmission test are about 14 to 20 ions per shot. The analysis of the spectra is typically cut down to 10 turns because of a lot of overlapping signal peaks in the beginning that are extremely hard to analyze. So all ion numbers calculated are the ion numbers that are still in the ring after 10 turns. This overlap of signals is caused by many ions in the beginning that are not all moving isochronously and will drop out of the ESRs acceptance after some turns.

At each spectra the decay of the amplitude over time can also be clearly seen (fig. [5.5]). The order of the decay constant for each spectra is in the order of about 40 turns (table [7.1]). The rate that is effectively seen by the channel plates detector depends on multiple factors. The effective incident rate on the micro channel plate detector can be calculated by

$$f_{Eff} = f_{Ring} N_{Ion} \bar{n}_{SE} \tag{5.1}$$

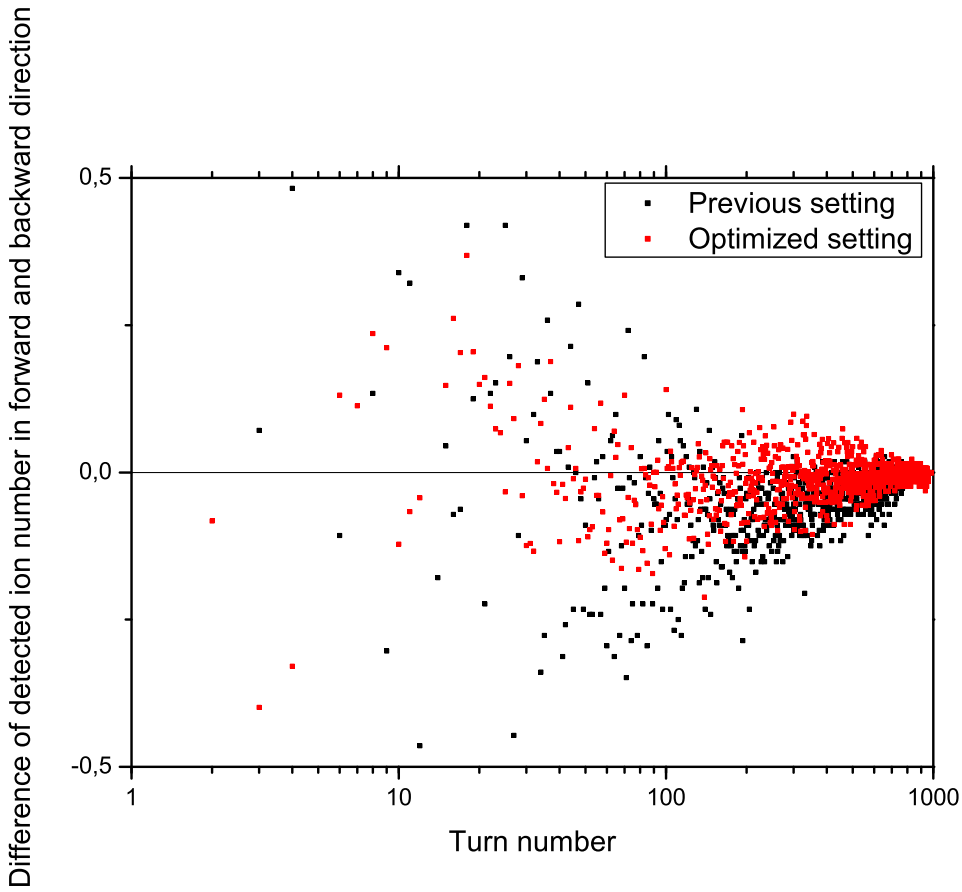

Figure 5.4: Difference of the detected ion number in forward and backward direction. The optimized setting shows a decreased scattering around a mean value of -0.00437 ± 0.0468 while the previous setting has a mean value of -0.01832 ± 0.0939

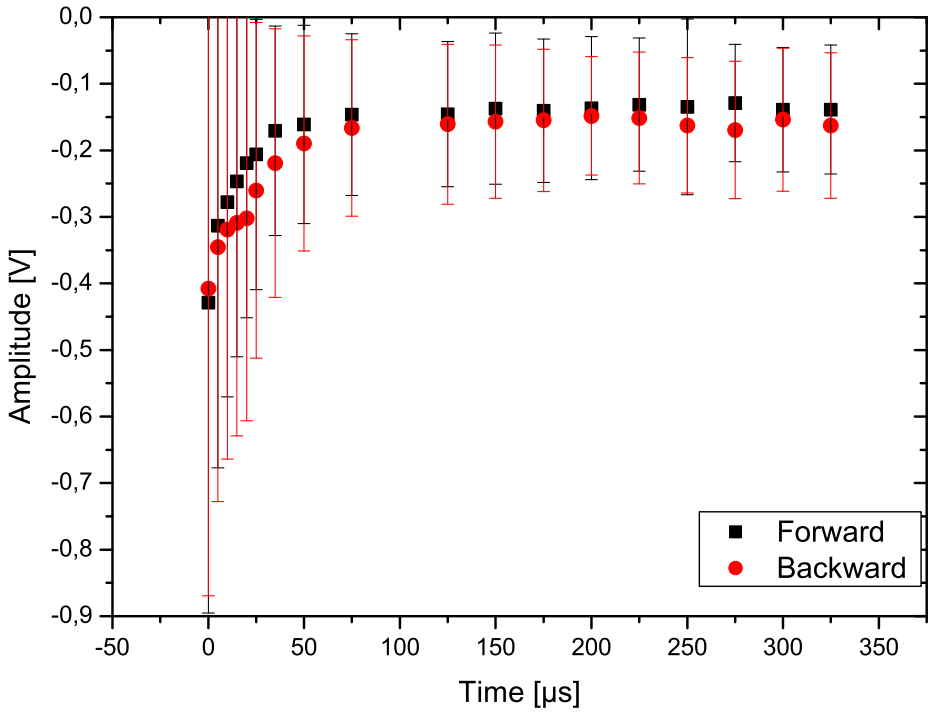

Figure 5.5: Development of the average signal amplitude over the measurement time of one shot. Therefore the amplitude development of the new optimized electrode and magnet setting is used. The same exponential decay of the amplitude can be clearly seen that is expected from the offline tests (chapter 4.4).

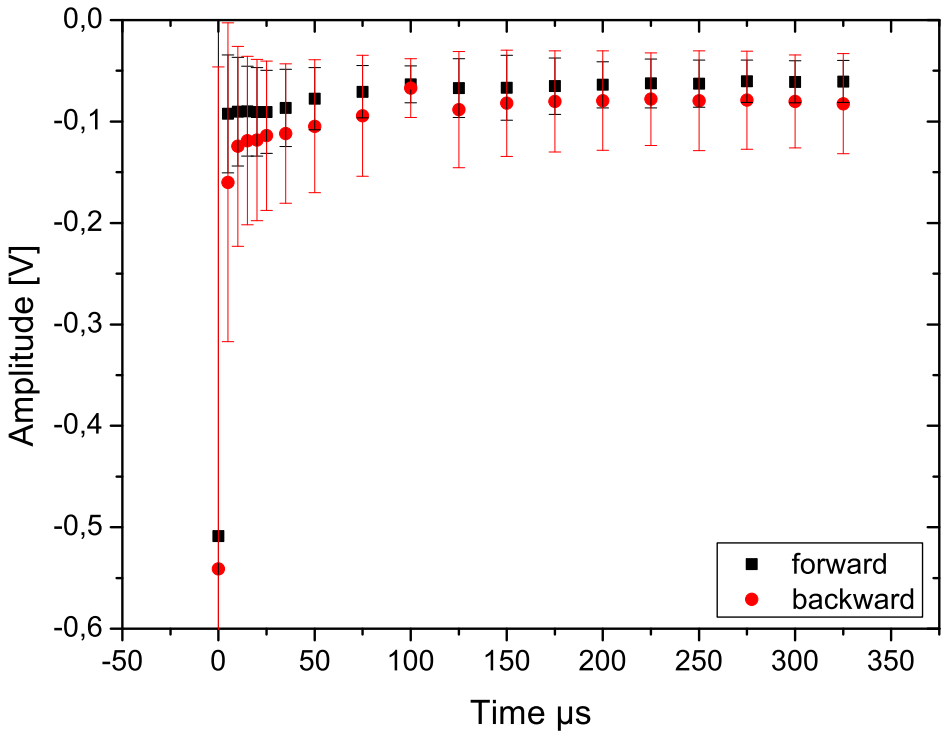

Figure 5.6: Time development of the average amplitude for the previous electrode and magnetic setting but at higher intensity of about 20 ions. It shows the expected faster decay of the amplitude down to an even smaller quasi static amplitude. This effect shows clear evidence of allocating it to a dead time effect of the MCP detector.

while $f_{Ring} = 2$ MHz is the ions revolution frequency, N_{Ion} the ion number per shot in the ring and $\bar{n}_{SE}$ the average created number of secondary electrons per ion. For a typical number of 14 ions and an average secondary electron number of 3.6 per ion the effective frequency is about 100 MHz. Increasing the ion number per injection the decay slope of the amplitude increases like expected from the offline experiments (fig. [5.6]). Not only the amplitudes decay faster but also the amplitudes saturation values decrease further so that in the end the amplitudes are even closer to the noise level.

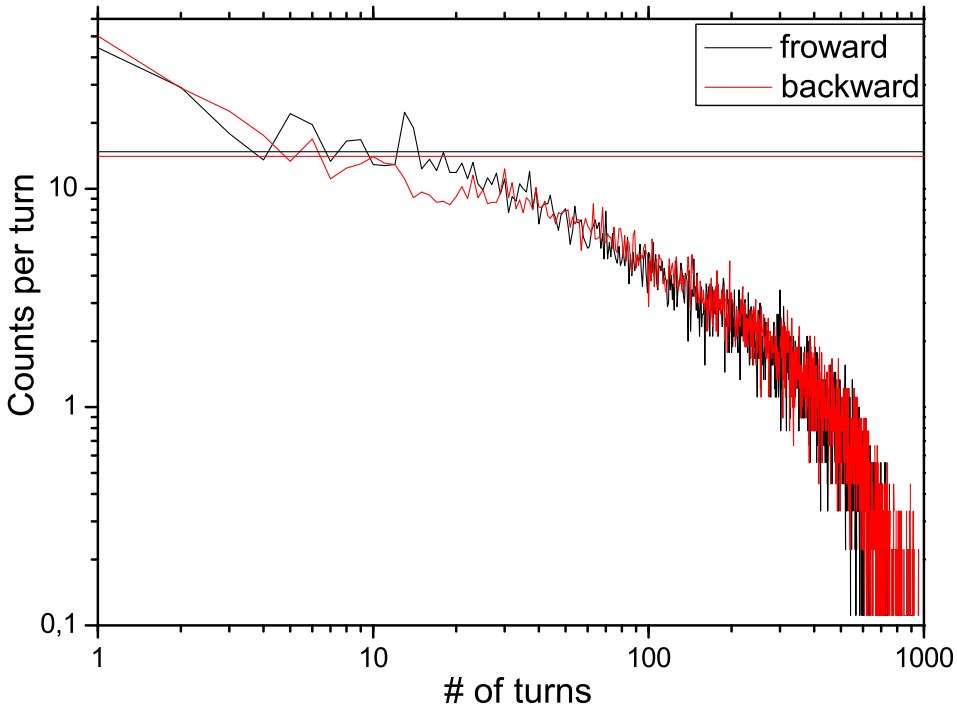

Figure 5.7: Development of the average number of signals found at each turn over the total measurement time and the new voltage and magnet setting of $I = 1.8$ A. The black curve represents the forward branch of the TOF-detector while the red curve represents the backward branch. A simultaneous drop of both detector branches is seen which yields a symmetric usage of the detector foil.

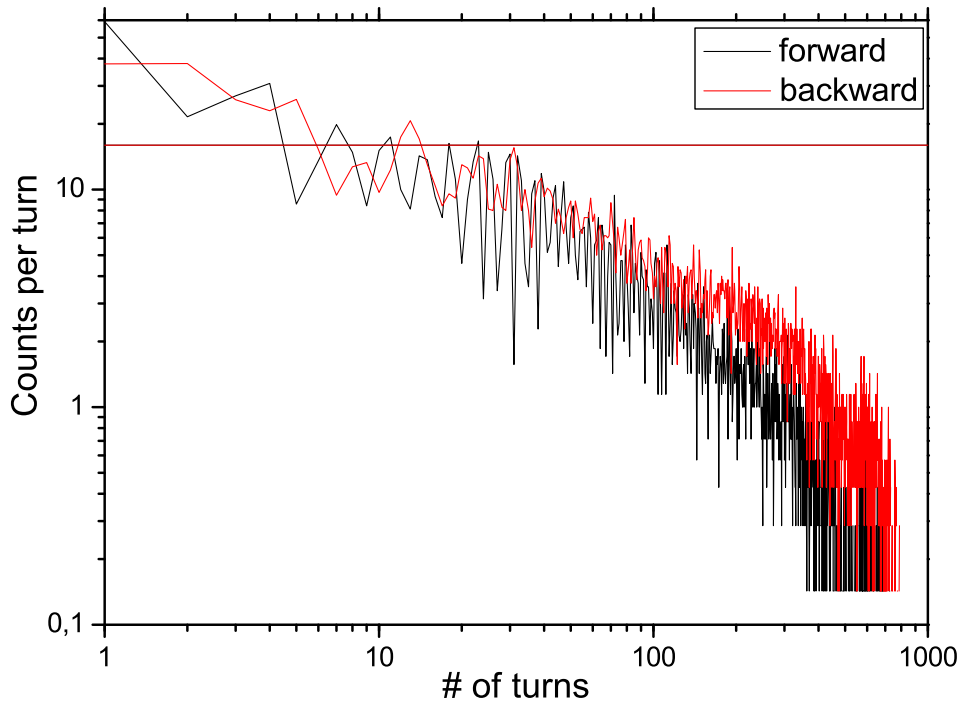

Figure 5.8: Development of the average number of signals found at each turn over the total measurement time and the previous voltage and magnet setting $I = 1.7$ A. The black curve represents the forward branch of the TOF-detector while the red curve represents the backward branch. It can be clearly noticed that in the average the black detector branch stop to register signal earlier than the red one. This effect is caused by a asymmetric usage of the foil.

5.2 Foil Pulsing

Before the problem of efficiency decay over time caused by the finite recharge time of the MCP was known the effect of amplitude dropping was attributed to too many ions injected in the beginning of the measurement. Typically the non-isochronous ions in the beginning just revolve 1 to 8 turns and are lost. So the idea to prevent the high amplitudes and so the decay in the beginning was to switch of the MCP detector and switch it on after the unstable ions are already dropped out. This procedure could save necessary channels for ions that are moving isochronously.

So to further verify the decay of the amplitude caused by the finite recharge time this concept is tested. Therefore not the MCP detector is switched on or off but rather the foil voltage. Decreasing the foils voltage to a value smaller than the MCPs first surface voltage almost no electron can fly to the MCP detector. Only electrons with high kinetic energies are able to be bent onto the MCP but this number should be minor. The foils voltage is raised to the normal operation value by the same pulser that is used for the pulsing of the electrons source of the MCP test setup. Therefore the pulser lowers the voltage on the foil by getting the ESR injection trigger and raises the voltage to the normal value after 125 μs.

The spectra taken with the pulser shows the same behavior of the amplitude decay like the non pulsed (fig. [5.9]). This experiment again verifies the assumption of dead time effects of the MCP. Increasing the number of injected ions into the ring a more pronounced decay of the amplitudes can be observed (fig. [7.8]). This effect shows the expected behavior of the micro channel plate at higher rates too (eq. 3.71). A higher particle flux yields a more pronounced dead time effect. So the problem of decreasing gain, amplitude and detection efficiency can be definitely addressed to the finite recharge time of the MCP and not to the more or less non-isochronous particles in the first turns. So the idea of using a pulser can be rejected because if there is no interest in the first few turns they can be simply taken out of the analysis afterwards what has ben already done.

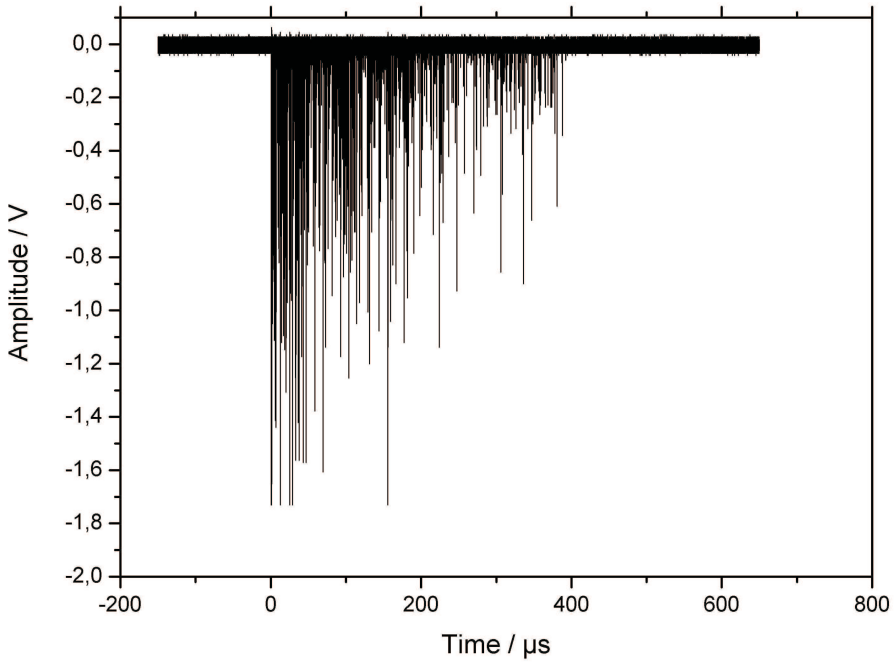

Figure 5.9: Original spectra taken by using the pulsed mode of the foil. The spectra shows again the decay of amplitudes over time even after already losing most of the ions moving on non-isochronous trajectories. So the amplitude decay can only be addressed to the dead time effect of the MCPs.

5.3 Survival Probability of Ni-Ions in the ESR

To compare the combination of the effects of the detection efficiency and the ion movement in the ring to the experimental data the development over time of the number of detected ions is used. It is discussed using the experimental data of the new optimized detector setting because this setting should yield the best description because almost the total foil aperture is used. The development over time of the number of detected ions in dependence of the different electrode potentials and the magnetic field can be found in fig. [7.7]. Using a setting that does not use most of the foils area or will be even asymmetric for both branches will not yield reasonable results. The number of found peaks are sorted time resolved. So it is possible to create a curve that shows the average number of peaks found per turn. In chapter 3.2.5.1 a Monte Carlo code is used to calculate the ion survival probability for a specific number of ions in the ring. This calculated curve is normalized to the real ion number that is calculated by the programm m-trace. So the theoretical curve N_{MC} is normalized to 14.3 ions at turn number

10. Turn number of 10 is chosen because m-trace calculated just down to 10 turns. Comparing both curves it can be seen that the experimental curve starts to drop much earlier than the expected curve. This effect can be explained by the exponential drop of the detection efficiency. So the expected number of detected ions $N_{Detected}$ including a finite time dependent detection efficiency caused by the MCPs can be written as

$$N_{Detected}(t) = N_{MonteCarlo}(t)\varepsilon_{Detection}(t) = N_{MonteCarlo}(t)(1 - e^{\varepsilon_{MCP}(t)\bar{n}_{SE}})\varepsilon_{Tr} \quad (5.2)$$

The average number of secondary electrons $\bar{n}_{SE}$ does not change over the turn number but the detection efficiency $\varepsilon_{MCP}(t)$of the MCP changes from 60% to about 10% as it can be seen from offline experiments for a rate of about 100 MHz (fig. [4.17]). From the offline data the detection efficiency of the micro channel plate detector at this rate is given by

$$\varepsilon_{MCP}(t) = 0.5e^{-\frac{t}{\tau}} + 0.1 \quad (5.3)$$

while τ is taken from the offline experiments and is about 44.2 turns for this rate tab. [4.19]. The transmission probability is assumed to be 100%. The influence of the transmission probability starts to play a role for higher turn number where ions pass through positions of the foil that are more sensitive to initial conditions. This effect starts to play a significant role at about 1000 turns what corresponding to about 15 mm of beam shifting caused by the energy loss [Wei-07].

It can be noticed that by including all these factors a reasonable agreement with the experimental data can be found (fig. [5.11, 5.10]). To compare the time evolution of the coincidence signals one needs to take into consideration that the transmission probability of the electrons is just about $\varepsilon_{CoinTr} = 70\%$. This value is also found by using the Monte Carlo simulation. Therefore only electrons that originated from one point of the foil and can be transported in forward and backward direction onto the MCP detectors are counted as valid. Assuming that each branch is independent from each other the coincidences can be written as

$$N_{Coin,Detected}(t) = N_{MonteCarlo}(1 - e^{\varepsilon_{MCP}(t)\bar{n}_{SE}})^2\varepsilon_{CoinTr} \quad (5.4)$$

The description of the coincidence seems not to be as good as the description of each single detector over the total time (fig. [5.12]). But it needs to be taken into account that the particle trajectories have also a systematic average movement that is not included in the time dependency. The coincidences are more sensitive to local variations on the foil and could cause a more significant effect even for higher turn numbers. It should also be noted that in principle the incident rate on the MCP-detector is not constant over time because of the ion losses over time and so the influence of this effect is not considered.

The errors of the calculation are estimated in dependence of the uncertainty of ε_0, the error of ε_∞, the error of τ and the uncertainty of the average created secondary electron

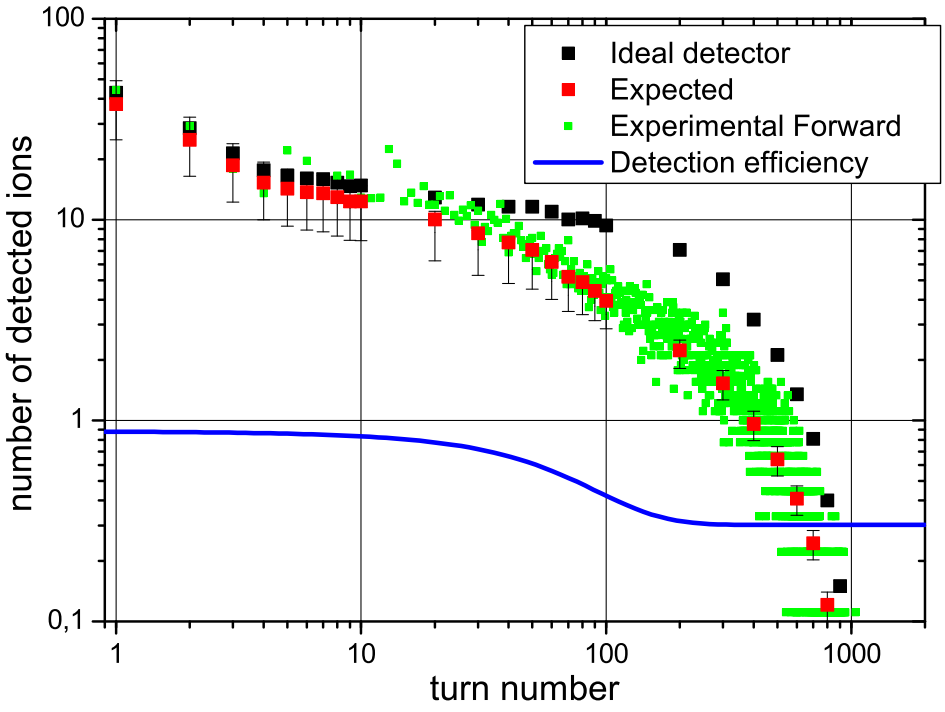

Figure 5.10: Temporal development of the average ion number over one shot for the new optimized detector setting of forward released electrons. The calculated survival probability at 10 turns is scaled to the calculated ion number ($N = 14$) using the m-trace programm. The black curve represents the expected ion survival probability just for including ion optical effects and the energy loss in the foil. The red circles represent the expected performance including the dead time effects of the MCP (eq. 5.2). The green points are the average signals found per turn and therefore represent the measured number of detected ions. The blue line shows the time development of the detection efficiency of the MCP (eq. 5.3).

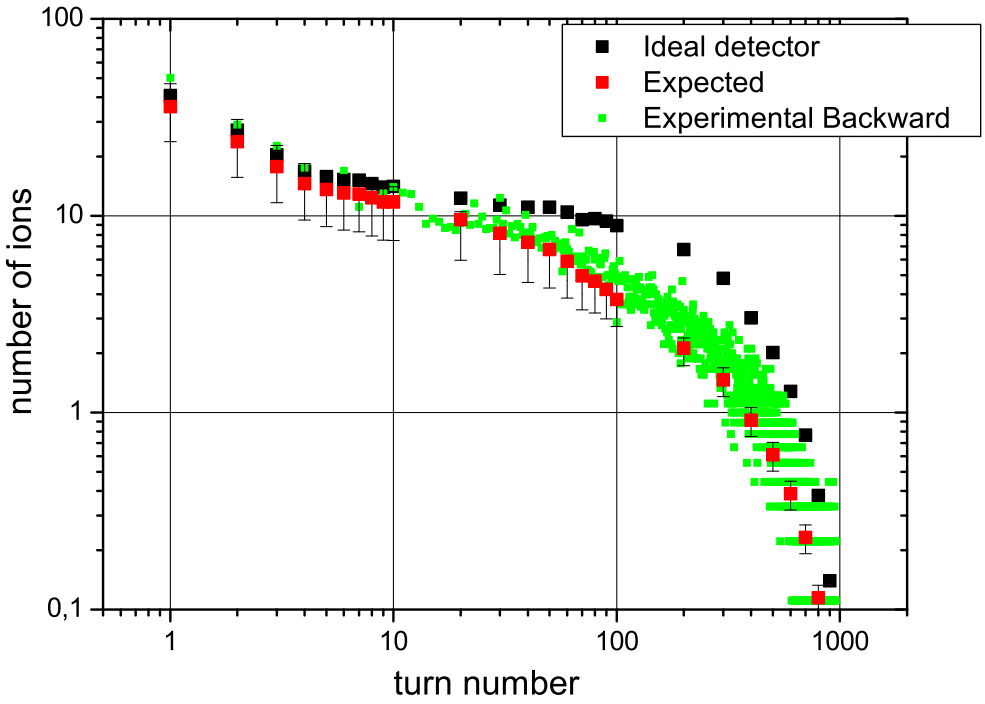

Figure 5.11: Temporal development of the average ion number over one shot for the new optimized detector setting of backward released electrons. The calculated survival probability at 10 turns is scaled to the calculated ion number ($N = 14$) using the m-trace programm. The black curve represents the expected ion survival probability just for including ion optical effects and the energy loss in the foil. The red circles represent the expected performance including the dead time effects of the MCP (eq. 5.2). The green points are the average signals found per turn and therefore represent the measured number of detected ions.

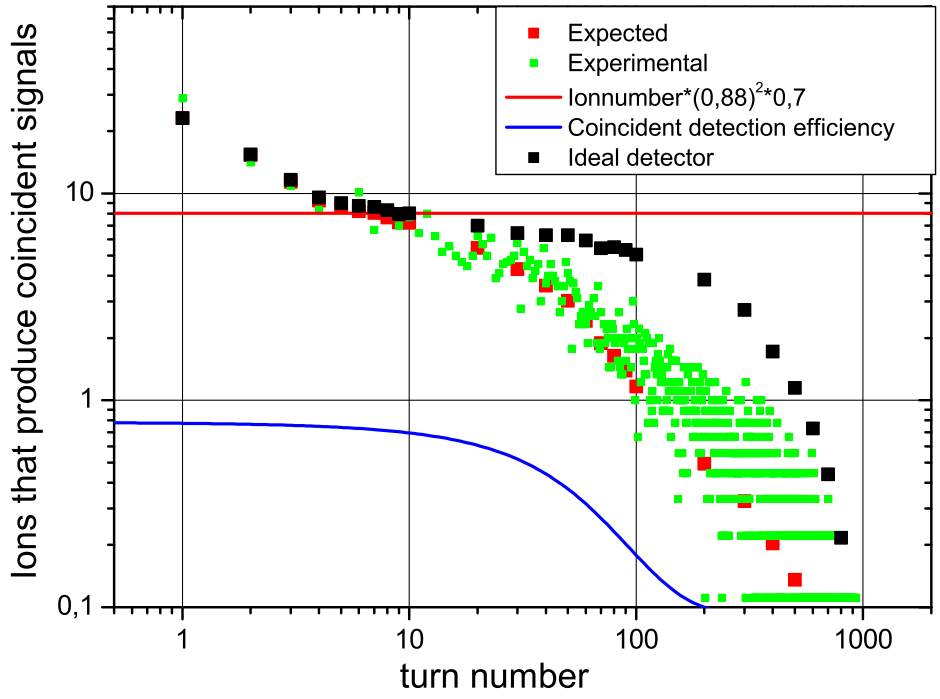

Figure 5.12: Temporal development of the average ion number detected in coincidence over one shot for the new optimized detector setting. The calculated survival probability at 10 turns is scaled to the calculated ion number $(N = 14)$ using the m-trace programm and the effective area of 70% that can be just used to create coincidences. The black curve represents the assumption of having a detector without dead time effects while the red circles represents the expected performance including the dead time effects of both MCPs. The green points are the coincidences found per turn and therefore represent the measured detected ion number in coincidence. The blue line shows the time development of the coincidence detection efficiency of both MCPs which is given by the square of the single detection efficiencies of the MCPS (eq. 5.3).

number n_{SE}. So the error is generally calculated by using

$$N_{Detected}(t) = N_{MonteCarlo}(t)(1 - e^{[(\varepsilon_0 - \varepsilon_\infty)e^{-\frac{t}{\tau}} + \varepsilon_\infty]\bar{n}_{SE}}) \tag{5.5}$$

and so

$$\begin{aligned}(\Delta N_{Detected}(t))^2 = &\left(\frac{\partial N_{Detected}(t)}{\partial \varepsilon_0}\Delta\varepsilon_0\right)^2 + \left(\frac{\partial N_{Detected}(t)}{\partial \varepsilon_\infty}\Delta\varepsilon_\infty\right)^2 \\ &+ \left(\frac{\partial N_{Detected}(t)}{\partial \tau}\Delta\tau\right)^2 + \left(\frac{\partial N_{Detected}(t)}{\partial n_{SE}}\Delta n_{SE}\right)^2\end{aligned} \tag{5.6}$$

It is assumed that the Monte Carlo calculation of the ion survival probability has a neglible error. For the error calculation the following errors for the dependent parameters are chosen: $\Delta\varepsilon_0 = 5\%$, $\Delta\varepsilon_\infty = 5\%$, $\Delta\tau = 10$ s and $\Delta n_{SE} = 1.8$.

6 Outlook

The precision of isochronous mass measurements depends on the timing performance of the detector. Significant improvements of the detector could include the timing optimization while keeping the transmission efficiency as high as possible. The primary goal is to be able to detect the ion time it passes the foil.

Simulations already show that the influence of the initial conditions of the secondary electrons are critical for the timing but not for the transmission efficiency. Therefore, the measurement of the secondary electron spectra of the used foils and incorporation into the simulation could yield more precise timing information.

To be able to store the ions for a longer time in the ring the usage of carbon foils with thickness down to 10 $\mu g/cm^2$ is preferred. The secondary electron yield is saturated for a thickness of about 10 $\mu g/cm^2$. An increase of survival probability for a larger number of turns in the ring (fig. [6.1]) can be achieved. The position where the ion survival probability drops is proportional to the total energy loss of the ions in the foil within an accuracy of 10%. For the carbon foil of 20 $\mu g/cm^2$ coated with the same thickness of CsI on both sides the energy loss is 75 keV per passage while for pure carbon with thickness 20 $\mu g/cm^2$ the energy loss is only 45 keV. The energy loss for this two cases differs by a factor of 1.7 which enables so a larger number of revolutions. The decrease of the foil thickness by a factor of two also allows to increase the number of revolutions by a factor of about 2.

Another critical point that should be investigated further are the dead time effects of the micro channel plate detectors. Keeping track on the development of ultra fast micro channel plates with less dead time effects should be done. At the moment it is not possible to overcome the dead time effect in the channel plates. Micro channel plates with smaller pore sizes increase the number of useable channels and therefore also increase the rate capability. Another option is to develop an ultra-fast detector with timing and detection efficiency properties like a MCP but higher rate capability. For the FAIR project (fig. [6.2]) a new dual detector system will be developed based on the results of this work. Two time-of-flight detectors on a straight section can be also used to measure the velocity of the ions passing through both detector foils. This knowledge could be used to correct for non-isochronous movement in the new Collector Ring (CR). Presently, this information is obtained by $B\rho$-tagging at the dispersive mid focal plane of the fragment separator.

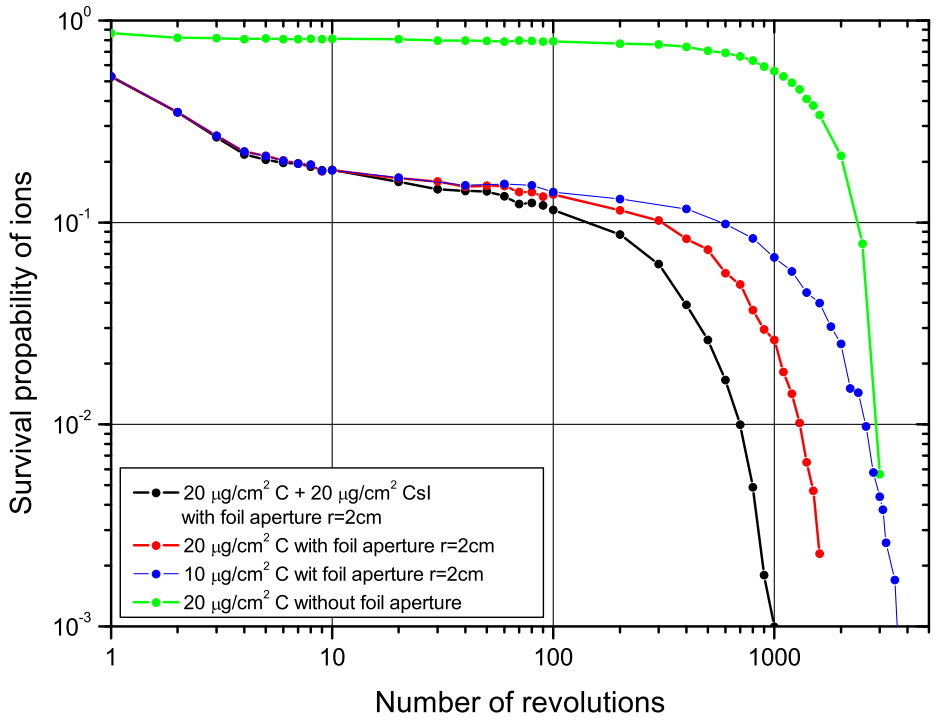

Figure 6.1: Calculated survival probpability of $^{64}Ni^{28+}$ ions in dependence of different foil thickness, coating and aperture size at the position of the detector foil. An decrease of the foil thickness yields an increase in the number of revolutions with similar survival probpabpilities of the ions. The shape of the survival probpability curve is mainly influenced by the aperture of the detector foil while the drop of the curve is mainly influenced by the foil thickness and coating [Wei-07].

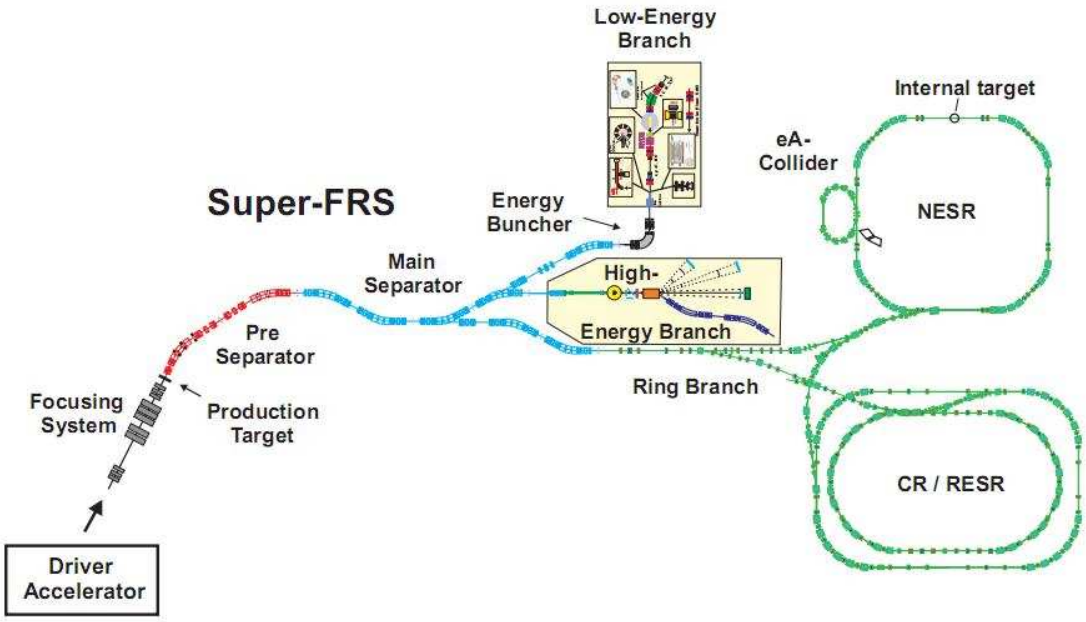

Figure 6.2: Schematic view of the new FAIR-facility. A primary beam imping on the production target produces secondary particles. The necessary ion species can be efficiently selected using the new fragment separator (SUPER-FRS). The so selected beam can be led to three main experimental areas; the low-energy branch, the high energy branch and the ring branch. All areas allow studies of properties of stable and exotic ions via spectroscopic methods.

7 Appendix

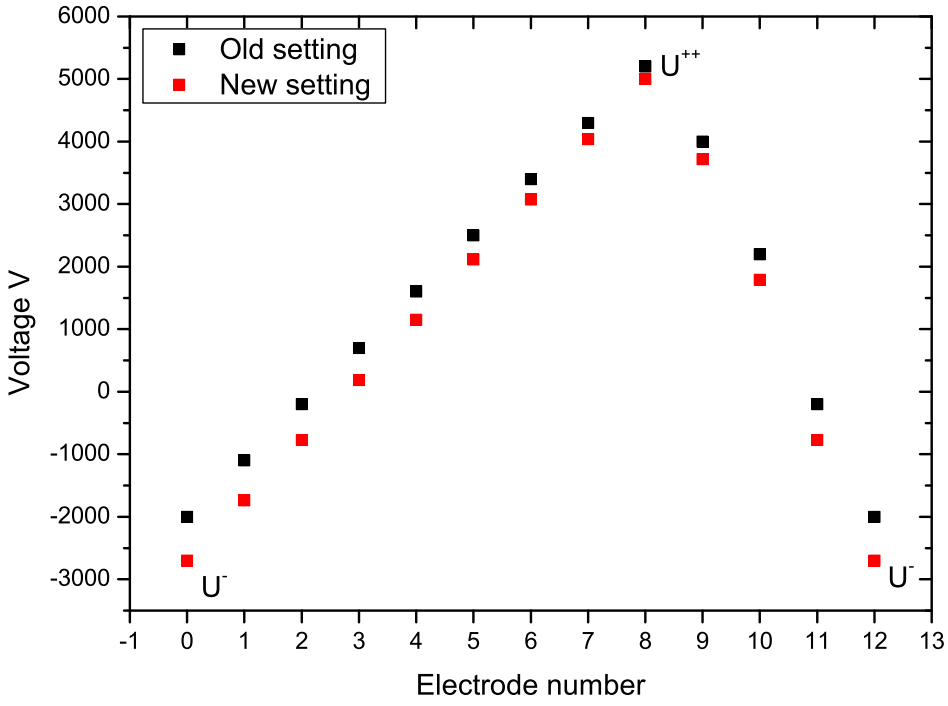

Figure 7.1: Voltage development of the potential plates of the TOF-detector. The black dotes represents the voltage development of the previous detector setting while the red squares represent the voltage development of the new optimized setting. The voltage drop is originally chosen to drop linearly to create a approximately homogeneous electric field in the region of the electron trajectories.

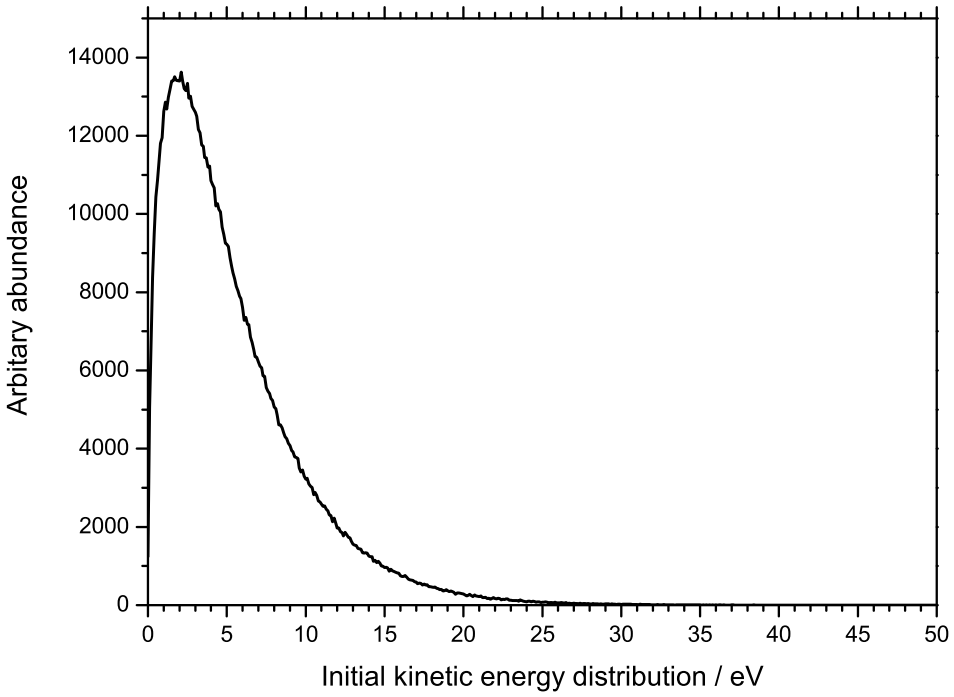

Figure 7.2: Initial kinetic energy distribution of the simulated electrons

Magnetic current	$\tau[\mu s]$ (Forward)	$\tau[\mu s]$ (Backward)
	Previous electrode potential	
1.6	19	31
1.7	47	22
1.8	28	18
1.9	39	16
2.0	34	19
	New electrode potential	
1.6	10	19
1.7	9	15
1.8	15	28
1.9	18	18
2.0	26	25

Table 7.1: Fitted decay constant of the amplitudes of the online experiment for each channel, both electrode potentials settings and variation of the magnetic current.

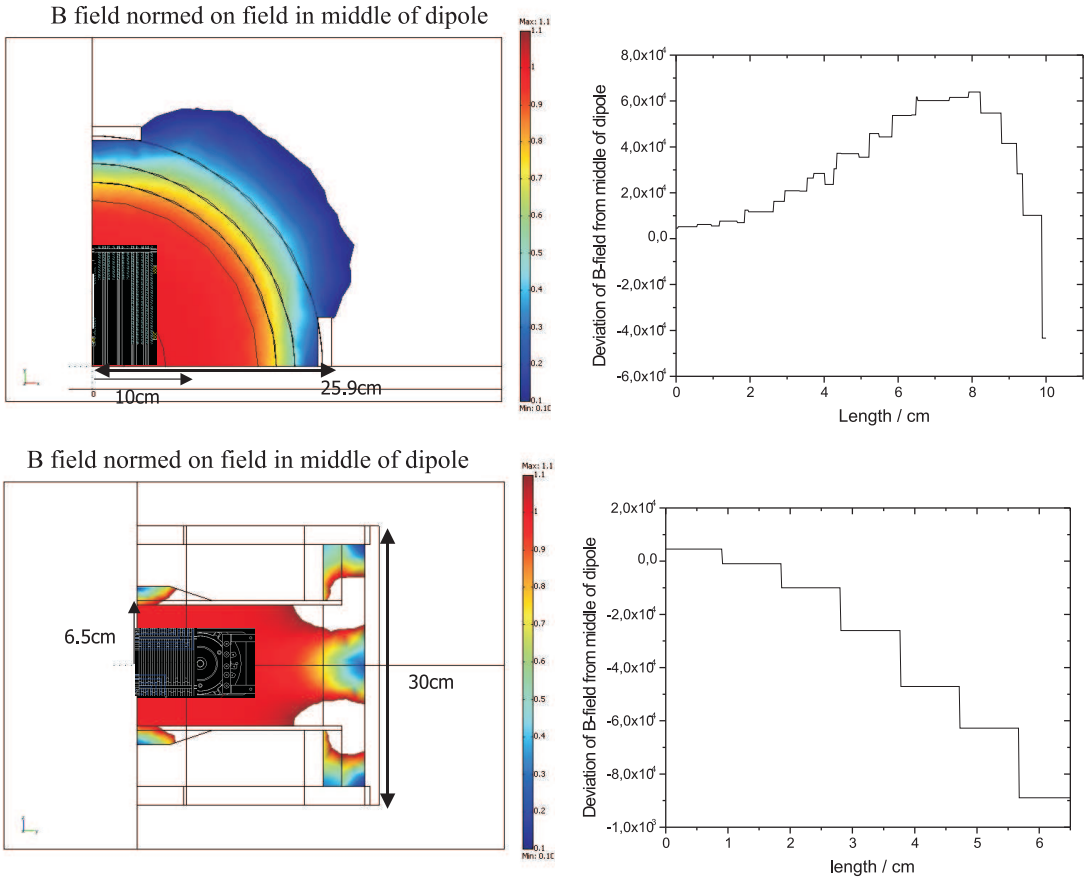

Figure 7.3: Simulation of the magnetic field homogeneity of the magnetic dipole. In radial and axial direction the relative field deviation is smaller than 10^{-4} for the region where the TOF-detector is installed.

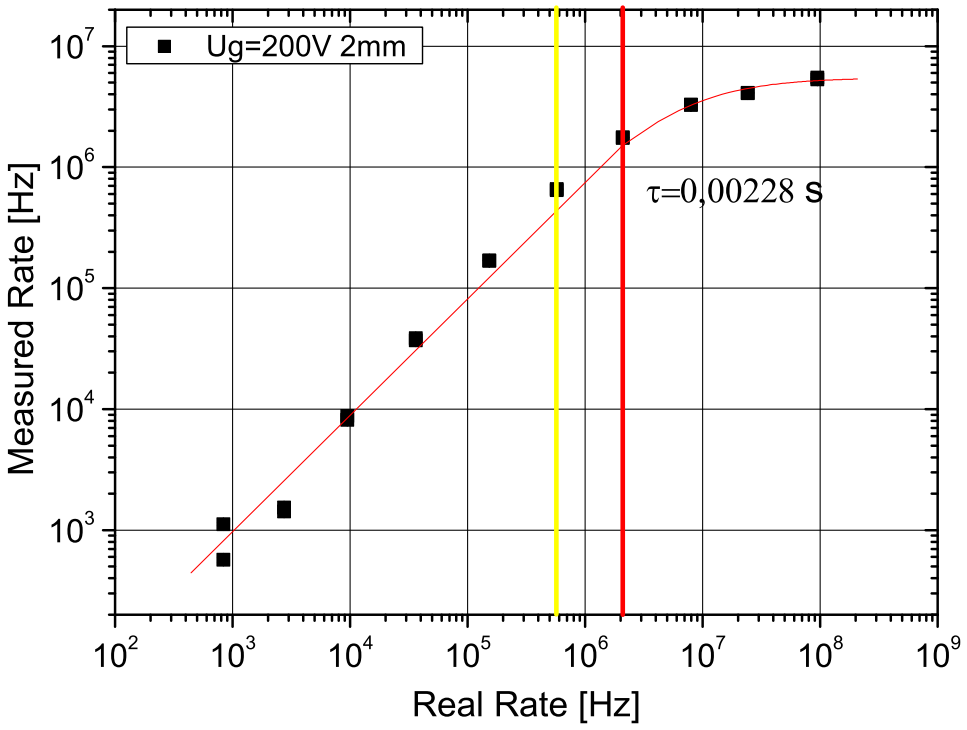

Figure 7.4: Electron rate dependency of the count rate of the MCP for a gap voltage of 200V and 2mm distance like the MCP detector is used in the current TOF-detector. The count rate is measured using a counter and by taking care that the detection efficiency is limited to the open area ratio OAR of about 60%. The count rate increases linearly with the time untill dead time effects start.

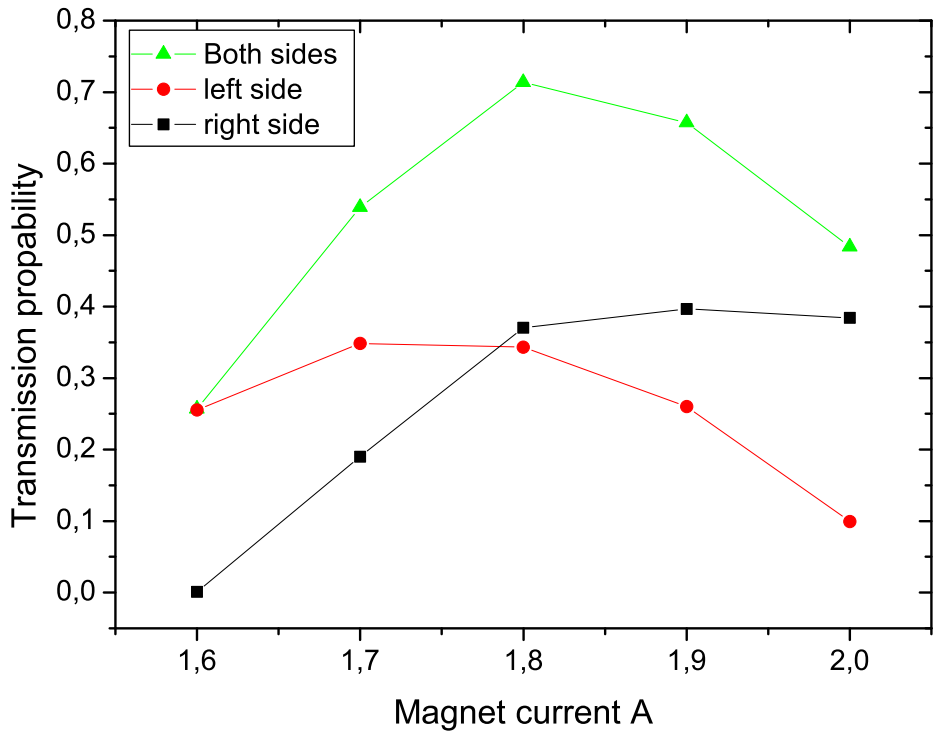

Figure 7.5: Transmission efficiency simulation for the previous electrode voltage setting for each half of the foil area. The red squares are the calculated efficiency contributing from the left half of the foil while the black squares are the contribution of the right half. The green squares are the sum of both contributions.

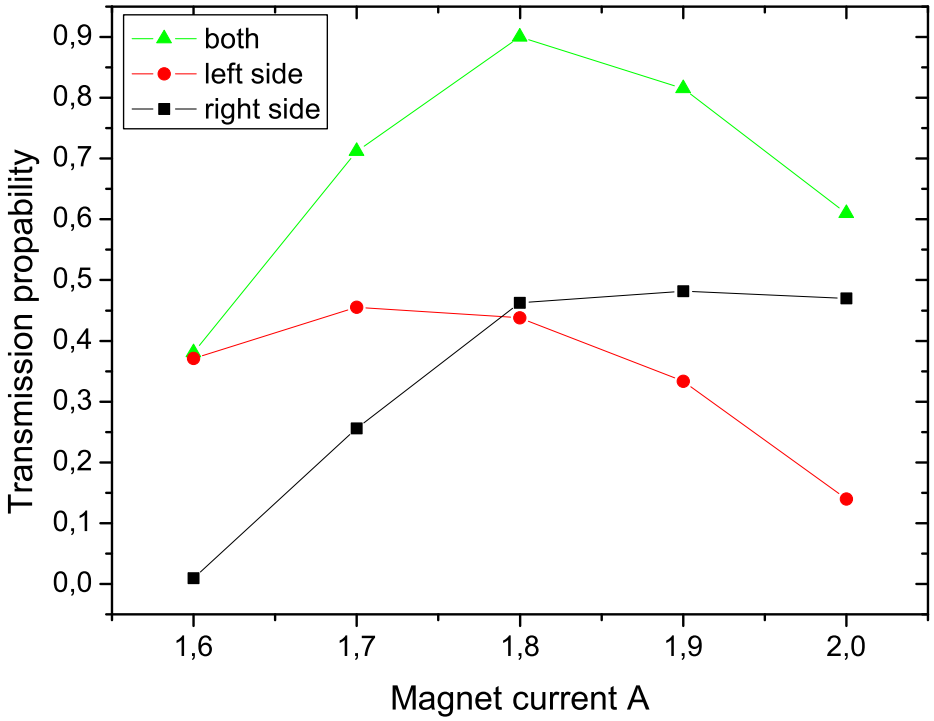

Figure 7.6: Transmission efficiency simulation for the new electrode voltage setting for each half of the foil area. The red squares are the calculated efficiency contributing from the left half of the foil while the black squares are the contribution of the right half. The green squared are the sum of both contributions.

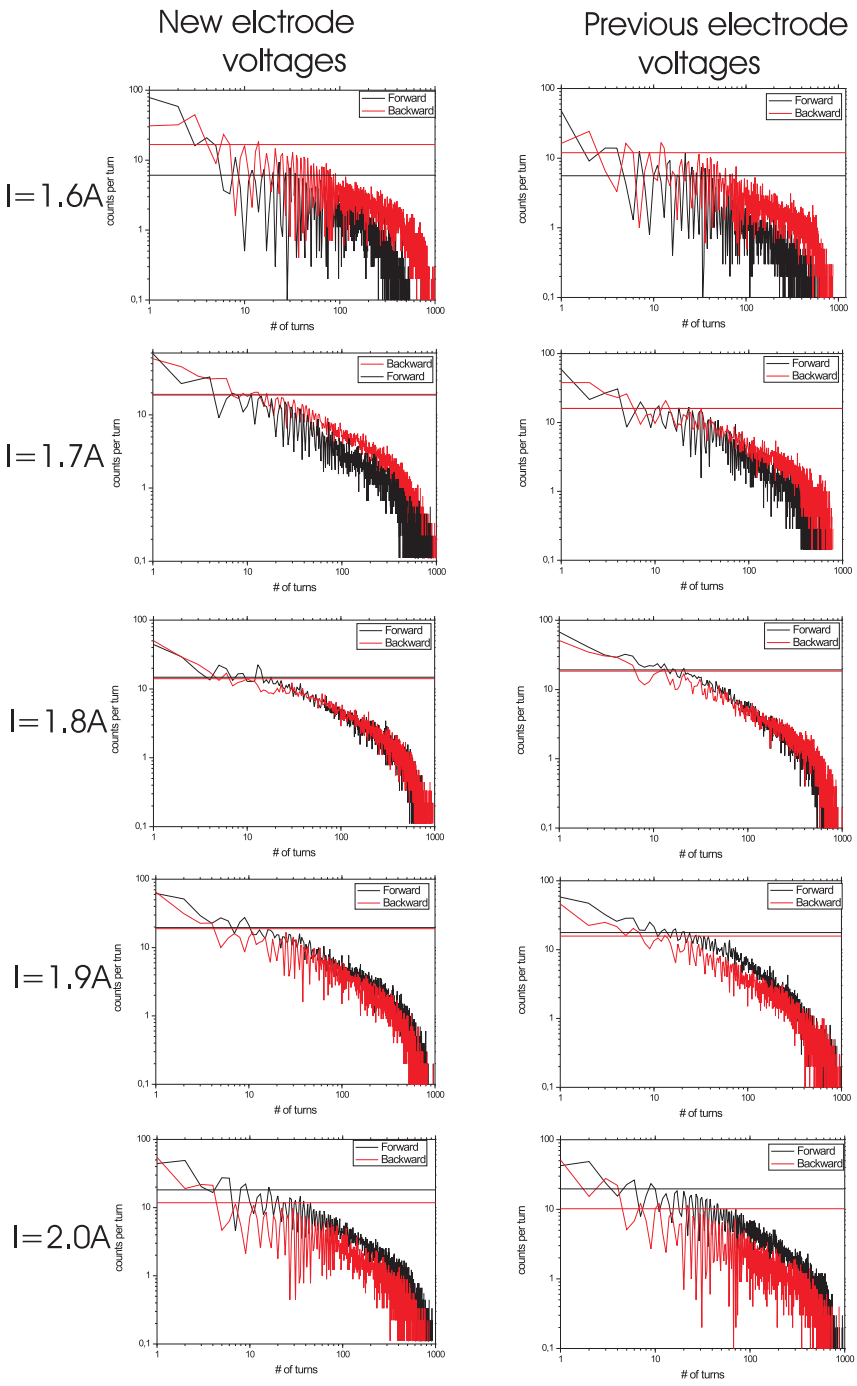

Figure 7.7: Time development of the average number of peaks for variation of the electrode voltages and the magnetic field. While a direct impact of the electrode voltage can not be clearly seen the impact of the magnetic field can be easily seen. For an optimum magnet current of 1.8 A the curves overlap and so the detection duration is the same on both branches. Furthermore the scattering in the number of detected peaks gets also smaller.

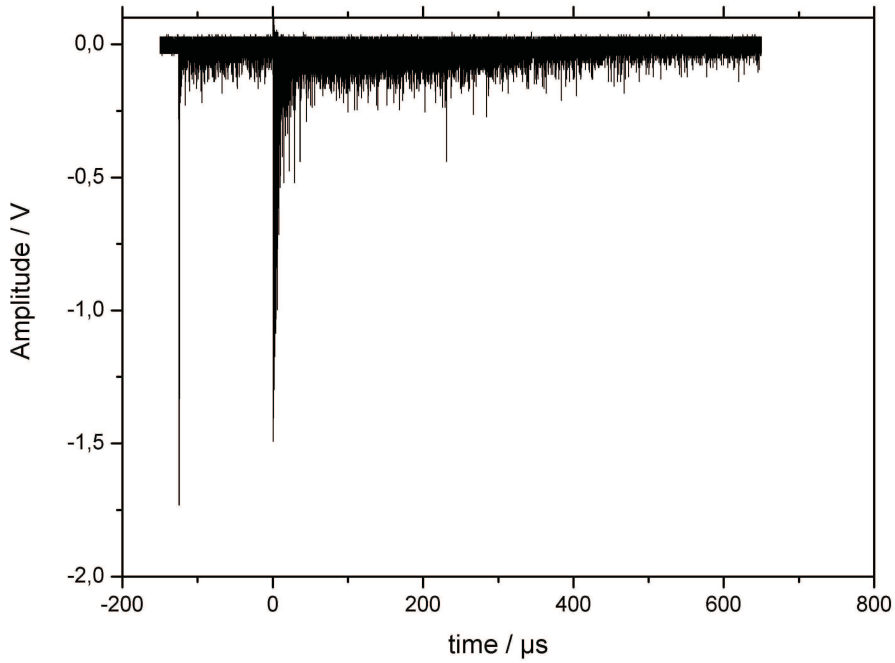

Figure 7.8: Amplitude time spectra by using a pulser on the foil for an initial ion number of about 20 ions. Therefore the beam intensity is increased while the time difference between the injection trigger and the pulsing of the foil voltage is about 125 μs. The spectra shows a faster decay of the amplitudes to an even smaller amplitude than for lower ion numbers.

Electrode	Voltage [kV]
U_{Wire}	-3.4
U_{Lens1}	-2.7
U_{Lens3}	-2.7
U_{Pipe}	-2.7
U_{Lens2}	-2.7
$U_{Repeller}$	-3.45
U_{Grid}	-3.35
U_{MCP}	-2.7

Table 7.2: Overview of the typically applied voltages in the MCP-test setup. The position and function of each electrode is given in 4.11. The difference of U_{Wire} and U_{MCP} yields the average kinetic energy of the electrons imping on the MCP-detector.

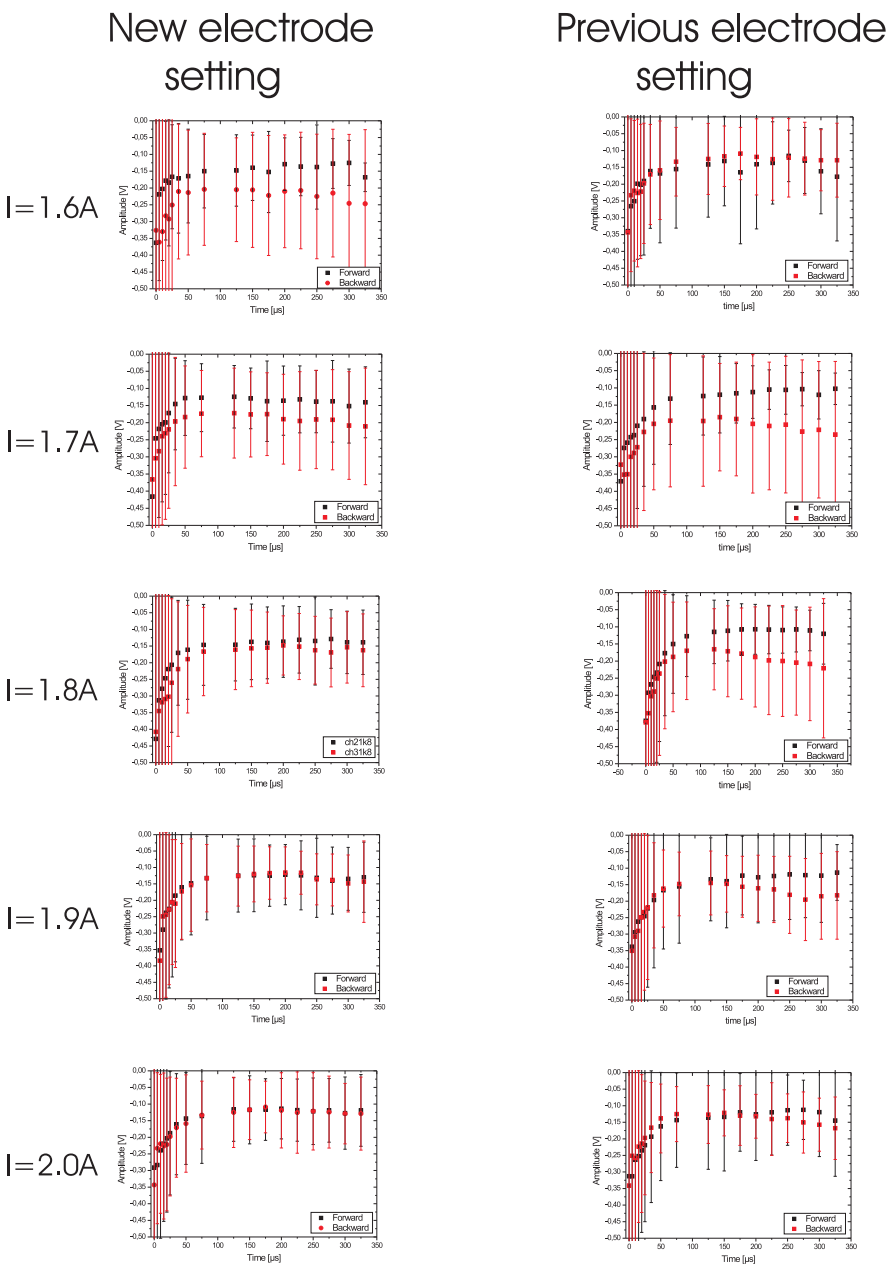

Figure 7.9: Time development of the average amplitudes of the signals at the online test for variations of the electrode potentials and the magnetic field. The amplitude decays over increasing time to a saturation value. The large error bars are mainly caused by the broad distribution of the amplitudes. Typically the scattering of the amplitudes of a micro channel plate detector is in the order of the average value.

List of Figures

List of Tables

Bibliography

[All-05] K. Allweins; Dissertation: *Echzeitfähiges Prüfverfahren zur Schweißnahtkontrolle an Aluminium-Bauteilen mittels magnetoresisitiver Sensoren* (2005)

[Agr-70] V. M. Agranovich et al.; *Study of the energy spectrum of secondary electrons arising from passage of α particles and fission fragmenst trough thin foils*. Soviet. Phys. JETP, **30** 2 p. 220 (1970)

[At] *Atomic Interaction with Matter*. www.linux.gsi.de weick/atima

[Bbfh-57] E. M. Burbidge, G. R. Burbidge, W. A. Fowler and F. Hoyle; *Synthesis of the elements in stars*. Rev. of Modern Physics, **29** 4 p. 547 (1957)

[Bbfp-85] K. Blsache, D. Böhne, B. Franzke and H. Prange; *The SIS heavy ion synchrotron project*. IEEE Trans. on Nucl. Sci. Ns-**32** 5 p. 2657 (1985)

[Bdc-99] J. R. J. Bennett, P. V. Drumm, R. Catherall, O. C. Johnsson and Isolde colaboration; *Measurements of intense beams of ^{11}Li from tantalum foil targe*t. Nucl. Instr. and Meth. **B155** p.515 (1999)

[Bec-90] K. Beckert et al.. The ESR Schottky-diagnosis system; In P. Martin and P. Mandrillon editors, *Proceedings of the 2nd European Particle accelerator Conference, Nice,* page 777, Gif-sur-Yvette, Cedex, (1990). Edition Frontiers.

[Bet-30] H. Bethe. *Zur Theorie des Durchgangs schneller Korpuskularstrahlen durch Materie*; Ann. Phys **5**, p. 324-400 (1930)

[Bh-78] J. D. Bowman and R. H. Heffner; *A novel zero time detector for heavy ion spectroscopy*. Nucl. Instr. and Meth. **148** p.503-509 (1978)

[Bin-92] K. J. Binns, P.J. Lawrenson, C. W. Trowbridge; *The anaylictal and numerical solution of electric and magnetic fields*. J. Willey ans Sons (1992)

[Bor-74] J. Borer et al.; *Nondestructive diagnosis of coastings beams with Schottky noise*. In Proc. IXth conference on high energy accelerators, Stanford U. S. Departement of commerce p. 53 (1974)

[Bou-79] C. Bouchard and J. D. Carette; *Secondary emission and ion feedback in*

a straight semiconducting channel. J. Appl. Phys. **50** 11 p. 7168-7176 (1979)

[Brun-97] A. Brunelle, P. Chaurand, S. D. Negra. Y. L. Beyec and E. Parilis; *Secondary electron emission yields from a CsI surface under impacts of large molecules at low velocities*. Rappid Communicat. in Mass Spectrometry **11** 353-362 (1997)

[Bry-93] P. J. Bryant anf K. Johnsen; *The principle of circular accelerators and storage rings*. Cambridge University Press (1993)

[But-87] J. C. Butcher; *The numerical analysis of ordinary differential equations: Runge-Kutta and general linear methods* Wiley-Interscience New York, NY, USA (1987)

[Chart-08] www.chartofthenuclides.com/

[Chen-07] L. Chen; Elektronische Mitteilung (2007)

[Chen-08] Dissertation in preparation (2008)

[Clou-89] A. Clouvas et al.; *Secondary electron emission from thin foils under fast-ion bombardement*. Phys. Rev. **B39** 10 p. 6316 (1989)

[Coe-06] S. Coeck, M. Beck, V.V. Golovko; *Micro channel plate response to high intensity ion bunches*. Nucl. Instr. and Meth. **A557** p. 516-522 (2006)

[Com] Comsol Multiphysics, www.comsol.de

[Det-74] K. Dettman, K. G. Harrison and M. W. Lucas; *Charge exchange to the continuum for light ions in solids*. J. Phys. B. Atom and Molecular Physics **7** 2 p.269 (1974)

[Dol-96] A. Dolinskiy et al.; *Operation of the ESR (GSI, Darmstadt) at the transition energy*. In S. Myers, A. Pacheco, R. Pascual, Ch. Petit-Jean-Genaz, and J. Poole, editors, Proceedings of the 5th European Particle accelerator conference, Institute of physics publishing p. 596-598, Bristol, (1996)

[Dre-96] C. G. Drexler and R. D. DuBois; *Energy- and angel-differential yields of electron emission from thin carbon foils after fast proton impact*. Phys. Rev. **A53** 3 p.1630 (1996)

[Eb-79] E. H. Eberhardt; Appl. Opt. **18** p. 1418 (1979)

[Eb-81] E. H. Eberhardt; IEEE Trans. Nucl. Sci. **NS – 28** p. 712 (1981)

[Eich-07] J. Eichler and T. Stöhlker; *Radiative electron capture in relativistic ion-atom collisions and the photoelectric effect in hydrogen-like high Z-systems*. Physics Report **439** p.1-99 (2007)

[Fra-87] B. Franzke; *The heavy ion storage and cooler ring project ESR at GSI*. Nucl. Instr. and Meth. **B24** 25 p. 18 (1987)

[Fras-91] G. W. Fraser, M. T. Pain, J. E. Lees and J. F. Pearson; *Micro channel plate at high count rates*. Nucl. Instr. and Meth. **A306** p. 247-260 (1991)

[Fras-92] G. W. Fraser, M. T. Pain and J. E. Lees; *Micro channel plate at high count rates: further studies*. Nucl. Instr. and Meth. **A327** 328-336 (1993)

[Gab-92] H. Geissel, P. Armbruster, K.H. Behr et al.; *The GSI projectile fragment separator (FRS): a versatile magnetic system for relativistic heavy ions*. Nucl. Instr. and Meth. **B70** 286 (1992)

[Gaus] http://mathworld.wolfram.com/Gauss-SeidelMethod.html

[Gei-92] H. Geissel et al.; *First storage and cooling of secondary heavy ion beams at relativistic energies*. Phys. Rev. Lett. **68** 23 p. 3412-3415 (1992)

[Gic-87] M. Berz, H. C. Hoffmann and. H. Wollnik; *COSY* 5.0 - *The fifth order code for corpuscular optical systems* Nucl. Instr. and Meth. bfA258 402 (1987)

[Giu-93] L. Giudicotti, M. Bassan, R. Pasqualotto and R. Sardella; *Simple analytical model of gain saturation in micro channel plate devices*. Rev. Sci. Instr. **65** 1 (1994)

[Gol-74] A. S. Holdhaber; *Statistical models of fragmentation processes*. Phys. Lett. **53**B p. 306-308 (1974)

[Hag-54] Hagstrum H. D.; Phys. Rev. **96** 1 p. 336 (1954)

[Hag-78] Hagstrum H. D.; *Electron and ion spectoscopy of solids*. Plenum Press, New York, **sect**.**1**, **2** p. 273 (1978)

[Has-98] D. Hasselkamp, K. O. Groeneveld, J. Kemmler; *Partcile induced electron emission II*. Springer Verlag GmbH (1998)

[Hen-81] B. Henke et al.; J. Appl. Phys. **52** p. 1509 (1981)

[Hhj-92] E. Hagebo, P. Hoff, O. C. Jonsson, E. Kugler, J.P. Omtvedrt, H. L. Ravn and K. Steffenson; *New production systems at isolde*. Nucl. Instr. and Meth. **B70** 162 (1992)

[ICRU-99] *Secondary electron spectra from charged particle interactions*. ICRU Report **550** (1999)

[Jab-88] A. Jablonski and H. Ebel; *Comparison of electron attenuation lengths and escape depths with inelastic mean free paths*. Surface and Interface Analysis **11** p. 627-632 (1988)

[Joy-04] D. C. Joy, M. S. Prasad and H. M. Meyer; *Experimental secondary electron spectra under SEM conditions*. Journal of microscopy, **215** 1 p. 77-85 (2004)

[Jung-96] M. Jung, H. Rothard, B. Gervais; *Transport of electrons induced by highly charged Ni (74 MeV/u) and Cu (9.6 MeV/u) ions in carbon. A study of target-thickness dependent electron yields*. Phys. Rev. **A54** 5 (1996)

[Jur-02] B. Jurado, K.-H. Schmidt, K.-H. Behr; *Application of a secondary-electron transmission monitor for high-precision intensity measurements of relativistic heavy-ion beams*. Nucl. Instr. and Meth. **A483** 3 p. 603-610 (2002)

[Knoe-08] R. Knoebel; Dissertation in preparation (2008)

[Kos-74] T. Koshikawa and R. Shimizu; *A Monte Carlo calculation of low energy secondary electron emission from metals*. J.Phys. D. Appl. Phys. **7** p. 1303 (1974)

[Kos-89] P. Koschar, K. Kroneberger, A. Clouvas, M. Burkard; *Secondary electron yield as a probe of preequilibrium stopping power of heavy ions colliding with solids*. Phys. Rev. **A40** 7 (1989)

[Lind-61] J. Lindhard and M. Scharff.; *Energy dissipation by ions in the kev region*. Phys. Rev. **124** 1 p. 128-130 (1961)

[LitS-08] S. Litvinov; Elektronische Mitteilung (2008)

[LitY-01] Y. Litvinov et al.; *Schottky mass measurements of cooled exotic nuclei*. In proceedings of the 2nd Euroconference on atomic physics at acceleratots. APAC2000, volume **132** of hyperfine interactions, pages 281-287 (2001)

[LitY-03] Y. Litvinov; Dissertation, Justus-Liebig Universität Gießen (2003)

[Low-04] D. P. Lowney et al.; *Characterization of CsI photocathods at grazing incidence for use in a unit quantum efficiency x-ray streak camera*. Rev. of Sci. Instr. **75** 10 p. 3131 (1994)

[Luc-72] M. W. Lucas, K. G. Harrison; *Beam foil auger spectroscopy*. J. Phys. B. At. Mol. Phys. **5** L20-L22 (1972)

[Lun-98] D. Lunney; *Nuclei in the cosmos* (1998)

[Mar-80] C. Martin and P. Jelinsky; *The size and distribution of electron cloud from a MCP detector*. Phys. Rev. A. Internal SSL Report (1980)

[Mat-04] M. Matos; *Dissertation: New mass measurements of short-lived neutron rich ^{238}U projectile fission fragments at the FRS-ESR-facilities*. (2004)

[Mor-89] D. J. Morrissey; *Systematics of momentum distributions from reactions with relativistic ions*. Phys. Rev. C, **39** 2 p. 460 - 470 (1989)

[Muenz-79] G. Muenzenberg et. al.; *The velocity filter SHIP, a separator of snslowed heavy ion fusion products*. Nucl. Instr. and Meth. **161** p. 65-82 (1979)

[Ohy-04] K. Ohya, T. Ishitani; *Monte Carlo study of secondary electron emission from SiO_2 induced by focused gallium ion beams*. Applied Surface Science **237** p. 606-610 (2004)

[Orig] Origin 7.0. http://www.originlab.com/

[Pen-76] D. R. Penn; *Electron mean free paths for free-electron-like materials*. Phys. Rev. **B13** 12 p. 5248 (1976)

[Pla-01] W. R. Plaß; Dissertation: *The dependence of rf ion trap mass spectrometry performance on electrode geometry and collisional processes*. Justus-Liebig Universität Gießen (2001)

[Pres-92] W. H. Press et al.; *Numerical recipes in C: the art of scientific computing*. Cambridge University Press, Cambridge, GB, second. Edition (1992)

[Pstar] Program: *PSTAR fo the calculation of proton stopping power*. http://www.exphys.uni-linz.ac.at/stopping/

[Rad-94] T. Radon; Diplomarbeit: *Aufbau und Test eines schnellen Zeitdetektors*(1994)

[Rog-82] D. Rogers and R. F. Malina; *Optimization of the performance of a tandem microchannel plate detector as a function of interplate spacing and voltage*. Rev. Sci. Instr. **53** 6 p. 1438 (1982)

[Ros-92] D. Rosenauer; Diplomarbeit: *Herstellung und Untersuchung von Detektorfolien mit unterschiedlichen Beschichtungen für Ionen-Flugzeitmessungen*. (1992)

[Roth-90] Rothardt et. al.; *Secondary electron yields from thin foils: A possible probe for the electronic stopping power of heavy ions*. Phys. Rev. **A41** 5 (1990)

[Roth-92] H. Rothard, J. Schou, K. O. Groeneveld; *Projectile- and charge-state dependent electron yields from ion penetration of solids as a probe of prequilibrium stopping power*. Phys. Rev. **A45** 3 (1992)

[Sch-80] J. Schou; Phys. Rev. **B22** 5 p. 2141 (1980)

[Schei-94] C. Scheidenberger et al.; *Direct observation od systematic deviations from the Bethe stopping theory for relativistic heavy ions*. Phys. Rev. Lett. **73**, p. 50-53 (1994)

[Schei-96] C. Scheidenberger et al.; *Energy loss straggeling experiments with relativistic heavy ions in solids*. Phys. Rev. Lett. **77** 19 p. 3987-3990, (1996)

[ScheiD-96] C. Scheidenberger; *Dissertation: Untersuchung der Abbremsung relativistischer Schwerionen in Materie im Energiebereich (100-1000) MeV/u*. II. Physikalische Institut Gießen (1996)

[Schei-98] C. Scheidenberger et al.; *Charge states of relativisic heavy ions ion matter*. Nucl. Instr. and Meth. **B142** p. 441-462 (1998)

[Schnei-75] D. Schneider, W. Hodge, B. M. Johnson, L.E. Smith and C. Freed Moore; *Auger electron emission spectra from foil and gas excited carbon beams*. Phys. Lett. **54A** 2 p. 174 (1975)

[Schu-00] C. Schulz; *Dissertation: Entwicklung eines neuartigen Niederdruck-Detektors mit hoher Orts- und Flugzeitauflösung zum Nachweis thermischer Neutronen*. Freie Universität Berlin (2000)

[Schw-88] Th. Schwab et al.; *In U. Grundinger, editor, GSI scientifc Report*, GSI-88-1, p. 284, D-64291 Darmstadt (1987)

[Sea-79] M. P. Seah and W. A. Dench; Surf. Interface Anal. **1**, **2** Sects 4.1.2, 4.2 (1979)

[Sei-67] H. Seiler; Z. Angew. Phys. **22** 4.1.2 p. 249 (1967)

[Sg-98] C. Scheidenberger and H. Geissel; *Penetration of relativistic heavy ions through matter*. Nucl. Instr. and Meth. **B135** p. 25 - 34 (1998)

[Sha-89] A. Sharma and J. G. Walker; *Effect of local deadtime in imaging detectors*. Quantum Opt.**1** p. 11-16 (1989)

[She-02] E. Shefer, A. Breskin, T. Boutboul; *Photoelectron transport in CsI and CsBr coating flims of alkali antimonide and CsI cathodes*. Journal of Applied Physics **92** 8 (2002)

[Shi-99] P. M. Shikhaliev; *Saturation model for secondary electron multiplier detectors*. Nucl. Instr. and Meth **A420** p. 202-210 (1999)

[Shih-97] A. Shih et al.; Applied Surface Science, **111** p. 251 (1997)

[Sta-02] J. Stadlmann; *Dissertation: Erste isochrone Massenmessung kurzlebiger Nuklide am Experimentierspeichering der GSI* (2002)

[Ste-96] M. Steck; *Anomalous temparature reduction of electron-cooled heavy ion beams in the storage ring ESR*. Phys. Rev. Lett. **77** 18 p. 3803 (196)

[Ster-57] E. J. Sternglass; *Theory of secondary electron emission by high speed ions*. The Phys. Rev., Second series **108** 1,2 (1957)

[Torn-90] R. Tornov; *A new method to measure and increase the detection efficiency of a microchannel plate for 100 keV electrons*. Meas. Sci. Technol. **1** p. 576-580 (1990)

[Troe-92] J. Troetscher et. al.; *Mass measurments of exotic nuclei at the ESR*. Nucl. instr. and meth. **B70** p. 455-458 (1992)

[Troe-93] J. Troetscher; *Dissertation: Der Experimentspeichering der GSI als Flugzeitmassenspektrometer für exotische Nuklide* (1993)

[Ver-73] R. L. Verma; *Secondary electron emission of caesium iodide*. J. Phys. D. Appl. Phys. **6** p. 2137 (1973)

[Vos-88] M. Vos et. al.; *Inelastic mean free paths for electrons at disordered interfaces*. Phys. Rev. **B39** p. 3274-3278 (1988)

[Wei-07] Helmut Weick; Elektronische Mitteilung (2007)

[Wiz-79] J. L. Wiza; *Micro channel plate detectors*. Nucl. Instr. and Meth. **162** p. 587-601 (1979)

[Wol-87] H. Wollnik; *Mass separators*. Nucl. Instr. and Meth. **A258** p. 289-296 (1987)

[Wu-06] G. Wu et. al.;*Ion trajectory simulation for electrode configurations with arbitrary geometries*. J. Am. Soc. Spectrom. **17** p. 1216 (2006)

8 Danksagung

Mein Dank gebührt all denen, die mich bei der Anfertigung dieser Arbeit unterstützt und beraten haben.

Zunächst danke ich Herrn Prof. Dr. Hans Geissel für die interessante Themenstellung und die zahlreichen Anregungen, die zum Gelingen dieser Arbeit beitrugen.

Herrn Dr. W. R. Plaß, Prof. Dr. Christoph Scheidenberger, Dipl. Phys. Timo Dickel, Dipl. Phys. Martin Petrick, Dr. Helmut Weick, Dipl. Phys. Natalia Kuzminchuck, Dr. Yuri Litvinov, Dipl. Phys. Ronja Knöbel, Dr. Serguei Litvinov sowie Dipl. Phys. Bachoua Sun, Dr. Kozhuharov danke ich für die Unterstützung während der Vorbereitung der Experimente am ESR.

Auch bei allen weiteren Mitgliedern der IONAS-Gruppe und Kernstrukturphysik II an der GSI, die zum Gelingen dieser Arbeit beigetragen habe, bedanke ich mich.

Weiterer Dank gilt:

- der mechanischen Werkstatt des II. Physikalischen Instituts.
- Mitarbeitern des Instituts für angewandte Physiks der Justus-Liebig-Universität, speziell Herrn Dr. K. Allweins sowie Dr. Kreutzbruck für die Bereistellung von FEM-Software und Rechnerkapazität.
- Herrn Dr. Hasselkamp für die zahlreichen Diskussionsrunden über Sekundärelektronenerzeugung.
- Herrn Dr. H. Braeuning für sein stets offenes Ohr für physikalische Problemstellungen und hilfreiche Tips.
- Herrn H. J. Schäfer, C. Karagiannis für die ingenieurstechnische Unterstützung.
- Herrn Dr. J. Jagutzki aus der Atomphysik der Universität Frankfurt für die hilfreichen Diskussionen über Microchannel-Detektoren.

Vor allem möchte ich aber meiner Frau, meinen Freunden und der Familie für die moralische Unterstüzung sowie deren Verständnis für meine Eingebundenheit während der Doktorrandenzeit danken.